LEAD ARTICLE

Acta Cryst. (1997). A53, 108–143

Multiple-Beam X-ray Diffraction for Physical Determination of Reflection Phases and its Applications

EDGAR WECKERT AND KURT HÜMMER

Institut für Kristallographie, Universität Karlsruhe (TH), Postfach 6980, D-76128 Karlsruhe, Germany. E-mail: edgar.weckert@physik.uni-karlsruhe.de

(Received 28 May 1996; accepted 9 September 1996)

Abstract

Theoretical and experimental advances in determination of three-phase invariants by multiple-beam X-ray diffraction are reviewed. The fundamental physics and mathematical analyses are explained. Plane-wave dynamical theory for the interpretation of multiple-beam interference is summarized. New results of its applications to the solution of the enantiomorphism problem of light-atom structures and to the solution of the structure of macromolecules by means of measured phases in conjunction with statistical methods are reported. Practical aspects of applying the three-beam diffraction technique to proteins are emphasized.

After obtaining his first degree in material sciences, Edgar Weckert received his doctorate in 1988 from the Faculty of Mathematics and Physics at the University of Erlangen, Germany. His thesis on three-beam X-ray diffraction using synchrotron radiation was the first application to the solution of the enantiomorphism problem of non-centrosymmetric low-Z structures. Since then, while a postdoctoral assistant at the University of Karlsruhe, he has been developing this technique both theoretically and experimentally and applying it to aperiodic structures and macromolecular crystals. His work on phasing macromolecular structures by means of physically estimated reflection phases in conjunction with maximum-entropy methods very recently won him the first Max von Laue prize of the Deutsche Gesellschaft für Kristallographie awarded to young scientists.

Kurt Hümmer received his doctorate in 1971 and his habilitation in 1978 from the Faculty of Mathematics and Physics of the University of Erlangen, Germany, where he investigated exciton polaritons in II–VI compounds under the supervision of Professor Erich Mollwo. Since then, he has been working on multiple-beam X-ray diffraction and applying this technique to the experimental determination of reflection phases. For the last four years, he has been at the University of Karlsruhe, Germany, as a full professor for crystallography.

1. Introduction

Both theoretical and experimental advances in various techniques have led to several powerful methods of surmounting the phase problem. Nowadays, the solution of even complex crystal structures like proteins is possible. In a recently published book (Woolfson & Fan, 1995), the authors brought together all the methods that have been and are being used. Some of the most effective ways are those that use experimental or physical data in conjunction with Patterson and statistical, *i.e.* direct and maximum-entropy, methods. Obviously, the most direct physical data for structure solution are the phases of reflections.

It has long been recognized that the only way to acquire phase information is by means of an interference experiment. The resultant amplitude and thus the intensity when waves are coherently superimposed depends on the phase difference of the individual waves. This is the principle of holography. Basic ideas how this can be achieved for X-rays were first published by Ott (1938), Bijvoet & MacGillavry (1939) and Lipscomb (1949). Bijvoet & MacGillavry stated that the intensity variation across a Kossel line due to the interference between the directly emitted and the diffracted waves of internal X-ray sources, which are atoms excited for fluorescence, contains phase information. Ott (1938) calculated the fine structure across a Kossel line and found that the interference contrast – he called it *Helldunkeleffekt* – depends uniquely on the phase of the structure factor. The intensity profiles are very similar to the Ψ-scan profiles discussed in this paper.

Lipscomb (1949) proposed to exploit the intensity change of a Bragg reflection when an additional reflection is simultaneously excited so that three beams, the transmitted and two diffracted ones, propagate in the crystal. Such a situation is described as three-beam diffraction. In 1937, Renninger had already shown that in such a situation the intensities of extinguished or weak reflections are drastically enhanced if a second strong reflection is simultaneously excited; so-called *Umweganregung* peaks occurred. If both Bragg reflections are comparably strong, then the coherent dynamical interaction of the excited wavefields leads to intensity

changes of each Bragg reflection, which are mainly due to interference effects. That interference contrast contains information on the phase difference of the interfering waves. Simple considerations by Lipscomb revealed that this information is a so-called triplet phase relationship or three-phase invariant, which is independent of the choice of the origin and is therefore a physically measurable quantity.

The development of the multiple-beam X-ray diffraction technique for experimental phase determination has been reviewed by Chang (1984, 1987) and Colella (1995). Surprisingly, no experimental results on this subject were published after Lipscomb's short communication until the middle of the 70s when the discussion of the X-ray case was kindled again by papers of Colella (1974) and Post (1975, 1977, 1979). Earlier theoretical and experimental work was concerned with the investigation of the anomalous transmission of X-rays, that is the Borrmann effect, which is enhanced in the case of simultaneously excited reflections (Ewald & Heno, 1968). For this it is sufficient to know the wave vectors, *i.e.* the eigenvalues, of the fundamental dynamical equations. However, the eigenvectors, amplitudes and phases, of the waves are also needed for the calculation of multiple-beam interference effects.

This article has different aims. In §2, a general solution of the plane-wave dynamical theory of N-beam X-ray diffraction is formally outlined. It is the basis of the computational analysis of N-beam diffraction intensities. It may be also of interest to those working in that field or in a related field when N-beam effects occur. In §3, the use of three-beam diffraction for the physical determination of phase relationships between Bragg reflections, so-called three-phase structure invariants or triplet phases, is discussed. §§3.1 and 3.2, in particular, should also give the non-expert an idea of the basic physics underlying the experiments for phase determination; it is pointed out that it is the three-beam interference effect that contains the phase information. For this readership, it is not necessary to read §2.2. The rest of §3 deals with new results concerning the influence of the diffraction geometry – Laue transmission and Bragg reflection – and *Pendellösung* effects for the interpretation of three-beam Ψ-scan profiles with respect to the phase determination. The last sections, §§5 to 7, should give the crystallographic community an idea of what can be done with this comparatively new technique with the emphasis on the application to macromolecular structures.

2. The basis of multiple-beam diffraction theory

2.1. *Fundamental dynamical equations and their interpretation*

The solution of the propagation equation of X-rays in crystals deduced from Maxwell's equations leads to the so-called fundamental equations of dynamical theory:

$$\mathbf{D}(\mathbf{h}_m) = \{\mathbf{K}(\mathbf{h}_m)^2/[\mathbf{K}(\mathbf{h}_m)^2 - \mathbf{k}_0^2]\} \times \sum_n \chi(\mathbf{h}_m - \mathbf{h}_n)\mathbf{D}(\mathbf{h}_n)_{[m]}. \quad (1)$$

It can be rewritten in the form of an eigenvalue equation

$$\{[\mathbf{k}_0^2 - \mathbf{K}(\mathbf{h}_m)^2]/\mathbf{K}(\mathbf{h}_m)^2\}\mathbf{D}(\mathbf{h}_m) + \sum_n \chi(\mathbf{h}_m - \mathbf{h}_n)\mathbf{D}(\mathbf{h}_n)_{[m]} = 0. \quad (2)$$

These equations describe the elementary concepts of crystal optics for X-rays such as specular reflection, refraction, diffraction and absorption.

In deriving (1), von Laue's optical model for X-rays is adopted, namely, the polarizability is translationally periodic since electromagnetic waves with wavelengths in the range of interatomic distances will resolve the three-dimensional periodicity of the electron density. Hence, the dielectric susceptibility $\chi(\mathbf{r})$ can be expanded in a Fourier series

$$\chi(\mathbf{r}) = \sum_n \chi(\mathbf{h}_n) \exp(-2\pi i \mathbf{h}_n \cdot \mathbf{r}), \quad (3)$$

where n runs over all reciprocal-lattice vectors (r.l.v.) $\mathbf{h}_n$. The usual structure factors are related to its Fourier components by

$$\chi(\mathbf{h}_n) = -\Gamma F(\mathbf{h}_n), \quad (4)$$

where

$$\Gamma = (r_e\lambda^2/\pi V_c); \quad \Gamma \simeq 10^{-6} - 10^{-7}. \quad (5)$$

$r_e = 2.8 \times 10^{-15}$ m is the classical electron radius and V_c is the volume of the unit cell. Consequently, the amplitudes of the proper wavefields must have the same periodicity as the crystal lattice and they are given by an Ewald–Bloch wave *Ansatz*:

$$\mathbf{D}(\mathbf{r}) = \sum_n \mathbf{D}(\mathbf{h}_n) \exp[-2\pi i \mathbf{K}(\mathbf{h}_n) \cdot \mathbf{r}], \quad (6)$$

where

$$\mathbf{K}(\mathbf{h}_n) = \mathbf{K}(\mathbf{0}) + \mathbf{h}_n \quad (7)$$

is satisfied.

Equations (1) to (7) express the self-consistent dynamical balance of the individual component waves (Bragg waves) that differ by r.l.v.'s. Kato (1992) pointed out that 'Self-consistency is an important concept in physics. P. P. Ewald was one of the few pioneers who recognized its importance and knew how to handle the problem'.

Equation (1) shows that each component wave is formed by the superposition (interference) of all the other Bragg waves, taking into account that only the

component of $\mathbf{D}(\mathbf{h}_n)$ parallel to $\mathbf{D}(\mathbf{h}_m)$, denoted by suffix $[m]$, is relevant for the resulting amplitude. Their electromagnetic coupling due to the interaction with the electrons is given by the Fourier component of the dielectric susceptibility of the difference r.l.v. $\mathbf{h}_m - \mathbf{h}_n$. The resonance term

$$\mathbf{K}(\mathbf{h}_m)^2/[\mathbf{K}(\mathbf{h}_m)^2 - \mathbf{k}_0^2] \qquad (8)$$

shows that only those waves have large amplitudes whose wave-vector magnitudes $K(\mathbf{h}_m)$ are very close to the vacuum value k_0, which means that $K(\mathbf{h}_m)$ terminates very close to the Ewald sphere. On the other hand, (8) allows the reduction of the infinite systems of equations (1) or (2) taking into account only those waves that have strong amplitudes (N-beam case). This term also shows that diffraction is nothing but a spatial resonance phenomenon. This should be kept in mind in order to understand the three-beam diffraction profiles, which will be discussed in §3.2.2.

The solutions of the eigenvalue equation (2) give the allowed wave vectors $\mathbf{K}(\mathbf{h}_m)$ (eigenvalues) and the relative amplitudes $\mathbf{D}(\mathbf{h}_m)$ (eigenvectors). The locus of the starting points of all the allowed wave vectors is called the 'dispersion surface'.

Before the outline of the quantitative calculation of N-beam diffraction profiles, let us first discuss the number of waves when N nodes of the reciprocal lattice including the origin are simultaneously very close to or lie on the Ewald sphere. It is worth interpreting the main properties in terms of ray optics for the two-beam case as the simplest example. Each ray is formed out of wave packets, which is a bundle of plane waves. The ray directions, the directions of the energy flow (Poynting) vectors, are normal to the dispersion surface as has been shown by Kato (1958) and Ewald (1958). This is the golden rule of rays and it is true also for the wave packet of the Ewald–Bloch wave field, which consists of all the component waves $\mathbf{D}(\mathbf{h}_m)$ whose wave vectors $\mathbf{K}(\mathbf{h}_m)$ differ by r.l.v.'s according to (7) (Kato, 1992).

The dispersion surface in a two-beam case is, roughly speaking, given by two dispersion spheres around two nodes of the reciprocal lattice, one being the origin (Fig. 1). It is the equi-energy surface for the wave vectors of the possible waves with fixed frequency that start at the surface and terminate at the nodes of the reciprocal lattice. At the intersection circle, where the eigenvalues of the problem would be degenerate, this degeneracy, however, is lifted owing to the interaction of the two waves $\mathbf{K}(\mathbf{0})$ and $\mathbf{K}(\mathbf{h}_m)$. In fact, each node of the reciprocal lattice can be treated equivalently. According to (7), the waves $\mathbf{K}(\mathbf{0})$ are coupled to the waves $\mathbf{K}(\mathbf{h}_m)$ *via* $\mathbf{h}_m$ and, *vice versa*, the waves $\mathbf{K}(\mathbf{h}_m)$ are coupled to the waves $\mathbf{K}(\mathbf{0})$ *via* $-\mathbf{h}_m$. In the sense of Bragg reflection at the lattice planes denoted by $\mathbf{h}_m$ and $-\mathbf{h}_m$, respectively, the term 'coupled' means diffracted. This again makes the main concept of dynamical diffraction evident, namely self-consistency. Near the interaction region at the Brillouin-zone boundary, the dispersion surface is split into a hyperboloid (non-crossing rule). This splitting is not drawn in Fig. 1, since the diameter of the hyperboloid is of the order of 10^{-5} compared with the radius of the dispersion spheres. The difference between the magnitudes of the wave vectors in vacuum, k_0, and in the crystal, $K(\mathbf{h}_m)$, which is of the same order, is also neglected, as well as the splitting of the dispersion spheres for different polarization states. Therefore, only one dispersion sphere is drawn for each node.

The relevant wave vectors for a given diffraction geometry are sorted out by the normals of the entrance and exit surface of the crystal since the tangential components of the wave vectors must be equal (boundary condition) because of the phase matching of the waves across the boundary. Thus, the wave vectors differ only in their normal components. In the two-beam case, for each polarization state there are four intersection points of the surface normal with the dispersion surface (Fig. 1) assuming a parallel-sided crystal slab. The directions of the Poynting vectors of the possible rays are the normals of the dispersion surface at the intersection points A, B, C, D (tie points according to Ewald). They point radially to the corresponding nodes 0 and H_n. Thus, eight rays, four for each polarization, are excited inside the crystal and two in vacuum at each side of a thin crystal slab (Fig. 1). They can be identified as the incident ray $\mathbf{S}_0$, the forward-transmitted rays $\mathbf{S}_t(\mathbf{0})$ and $\mathbf{T}(\mathbf{0})$, the specular reflected rays $\mathbf{S}_r(\mathbf{0})$ and $\mathbf{R}(\mathbf{0})$, the diffracted transmitted rays $\mathbf{S}_t(\mathbf{h}_n)$ and $\mathbf{T}(\mathbf{h}_n)$, and finally the diffracted reflected rays $\mathbf{S}_r(\mathbf{h}_n)$ and $\mathbf{R}(\mathbf{h}_n)$, where the S rays are inside and the R and T rays are outside the crystal. It should be noticed again that each ray $\mathbf{S}(\mathbf{h}_n)$ consists of a bundle of plane waves.

The wave vectors of the vacuum plane waves, identical with the vacuum rays $\underrightarrow{\mathbf{k}_t(\mathbf{0})} = \overrightarrow{B0}$, $\underrightarrow{\mathbf{k}_r(\mathbf{0})} = \overrightarrow{D0}$, on one hand, and $\mathbf{k}_t(\mathbf{h}_n) = \overrightarrow{AH_n}$, $\mathbf{k}_r(\mathbf{h}_n) = \overrightarrow{CH_n}$, on the other hand, have the same tangential component with respect to the crystal surface and they differ by a normal component of equal magnitude but opposite direction, *i.e.* their normal components have opposite sign. The wave vector of the incident ray is $\mathbf{k}_0$.

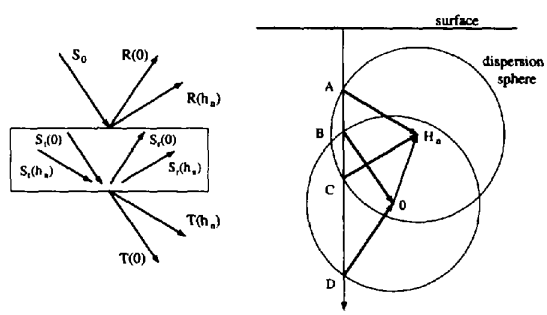

Fig. 1. Possible rays in crystal and reciprocal space for a two-beam case.

At this stage of the discussion, it is not necessary to distinguish between the Laue transmission and the Bragg reflection diffraction geometries. In both cases, all four rays are excited. It depends on the diffraction geometry which rays carry strong intensity and which are weak.

The two-beam properties discussed above can immediately be transferred to an N-beam case. Generally, for an N-beam case there are N reflected and N transmitted rays for each polarization state [*cf.* (11)].

2.2. *Solution of the fundamental equations*

2.2.1. *Eigenvalue problem.* In traditional treatments of solving the dynamical equations, the 'linearization of the eigenvalue equation' is usually applied. Since the differences in the magnitudes of the wave vectors in the vacuum and in the crystal are of the order of 10^{-5}, it can be assumed to a sufficient approximation that (Pinsker, 1978)

$$[\mathbf{k}_0^2 - \mathbf{K}(\mathbf{h}_m)^2]/\mathbf{K}(\mathbf{h}_m)^2 + \chi(\mathbf{0}) \simeq 2[K_0 - K(\mathbf{h}_m)]/k_0, \tag{9}$$

where

$$K_0 = k_0[1 + \tfrac{1}{2}\chi(0)], \tag{10}$$

$\mathbf{K}_0$ is the wave vector in the crystal for the one-beam case.

The linear expression (9) was called excitation error (*Resonanzfehler*) by Ewald. With the application of (9), half of the solutions are thrown out of the problem. Those rays are concerned that carry negligibly weak intensity in ordinary diffraction experiments. The strong rays remain, those are the forward-transmitted 0 rays, the diffracted transmitted rays of the Laue cases and the diffracted reflected rays of the Bragg cases. The complete set of solutions have to be taken into account in the case of extreme diffraction geometries, such as grazing incidence of the incoming ray, grazing exit where one or more pairs of reflected and transmitted rays are excited parallel to the crystal surface and extreme backward diffraction where $2\theta \simeq 180°$. A general solution of the plane-wave dynamical theory of N-beam X-ray diffraction was developed by Colella (1974). A short review of Colella's solution will be given here as we also use this general approach for the computational analysis of N-beam diffraction profiles.

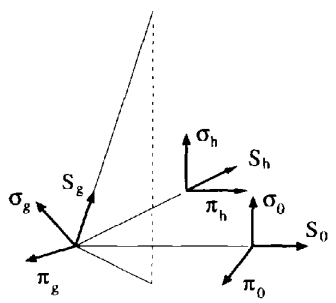

Fig. 2. Definition of the polarization vectors in a three-beam case.

The set of vector equations (2) can be decomposed into a set of $2N$ scalar equations since the displacement vectors $\mathbf{D}(\mathbf{h}_n)$ are normal to their wave vectors $\mathbf{K}(\mathbf{h}_n)$. Therefore, two orthogonal unit vectors $\boldsymbol{\pi}_n$ and $\boldsymbol{\sigma}_n$ are defined (Fig. 2) both normal to the wave propagation direction $\mathbf{s}_n = \mathbf{K}(\mathbf{h}_n)/|\mathbf{K}(\mathbf{h}_n)|$.

Then, $\mathbf{D}(\mathbf{h}_n)$ is expressed as

$$\mathbf{D}(\mathbf{h}_n) = D_\pi(\mathbf{h}_n)\boldsymbol{\pi}_n + D_\sigma(\mathbf{h}_n)\boldsymbol{\sigma}_n. \tag{11}$$

Insertion of (11) and multiplication by $\boldsymbol{\pi}_n$ and $\boldsymbol{\sigma}_n$ gives the following system of scalar equations of rank $2N$:

$$\{k_0^2/\mathbf{K}(\mathbf{h}_m)^2 - [1 - \chi(\mathbf{0})]\}D_\pi(\mathbf{h}_m) + \sum_{\mathbf{n}\neq\mathbf{m}} \chi(\mathbf{h}_m - \mathbf{h}_n)[D_\pi(\mathbf{h}_n)\boldsymbol{\pi}_n\boldsymbol{\pi}_m + D_\sigma(\mathbf{h}_n)\boldsymbol{\sigma}_n\boldsymbol{\pi}_m] = 0 \tag{12}$$

$$\{k_0^2/\mathbf{K}(\mathbf{h}_m)^2 - [1 - \chi(\mathbf{0})]\}D_\sigma(\mathbf{h}_m) + \sum_{\mathbf{n}\neq\mathbf{m}} \chi(\mathbf{h}_m - \mathbf{h}_n)[D_\pi(\mathbf{h}_n)\boldsymbol{\pi}_n\boldsymbol{\sigma}_m + D_\sigma(\mathbf{h}_n)\boldsymbol{\sigma}_n\boldsymbol{\sigma}_m] = 0. \tag{13}$$

From the system of $2N$ homogeneous linear equations (12) and (13), the eigenvalues, *i.e.* the unknown wave vectors $\mathbf{K}(\mathbf{h}_n)$, and the corresponding eigenvectors, *i.e.* the unknown relative amplitudes D_σ, D_π are calculated.

In a short-hand matrix notation, (12) and (13) can be written as

$$[\mathcal{A} + \mathcal{B}]\mathcal{D} = 0. \tag{14}$$

$\mathcal{D}$ is a column matrix whose elements consist of N pairs $D_\pi(\mathbf{h}_n)$, $D_\sigma(\mathbf{h}_n)$, $n = 1, 2, \ldots, N$. $n = 1$ refers to the origin of the reciprocal lattice $\mathbf{0}$. $\mathcal{B}$ is a diagonal matrix whose $2N$ elements consist of N equal pairs $B_{nn} = \mathbf{k}_0^2/\mathbf{K}(\mathbf{h}_n)^2$, one for each component of $D_p(\mathbf{h}_n)$, with $p = \pi, \sigma$. All the diagonal elements of matrix $\mathcal{A}$ are given by $[\chi(\mathbf{0}) - 1]$. The elements $A_{2n-1,2n}$ and $A_{2n,2n-1}$ are zero. All the other non-diagonal elements consist of the elements of the sums of (12) and (13) in the appropriate order.

This system has non-trivial solutions if

$$\det|\mathcal{A} + \mathcal{B}| = 0. \tag{15}$$

From this equation, which is of rank $2N$ for $\mathbf{K}(\mathbf{h}_n)^2$, $4N$ eigenvalues are found that give the $4N$ tie points due to the π and σ polarization components σ_n and π_n of each wave. As $\mathcal{B}$ is a diagonal matrix, (15) can be written as

$$\det|\mathcal{A}^{-1} + \mathcal{B}^{-1}| = 0. \tag{16}$$

The diagonal elements of $\mathcal{B}^{-1}$ now have the form $\mathbf{K}(\mathbf{h}_n)^2/k_0^2$.

Owing to the continuity of the tangential component of the wave vectors across the boundary, they differ by components normal to the crystal surface. Therefore, it is suitable to choose a Cartesian coordinate system with **y** and **z** parallel and **x** normal to the surface. Thus, each wave vector can be written as (Schwegle, 1993)

$$\begin{aligned}\mathbf{K}(\mathbf{h}_n)^2 &= (\mathbf{k}_0 + \mathbf{h}_n + \mathbf{v})^2 \\ &= v_x^2 + (2k_{0x} + 2h_{nx})v_x + (\mathbf{k}_0^2 + \mathbf{h}_n^2 + 2\mathbf{k}_0 \cdot \mathbf{h}_n),\end{aligned} \tag{17}$$

where $\mathbf{v} = (v_x, 0, 0)$. k_{0x} and $\mathbf{k}_0 \cdot \mathbf{h}_n$ depend on the angle of the incident beam with respect to the crystal surface and the lattice planes $\mathbf{h}_n$, respectively. Thus, the diffraction geometry at the entrance surface is fixed by these two parameters, the v_x's are the unknown eigenvalues.

According to (17), $\mathcal{B}^{-1}$ can be written as a sum of three diagonal matrices.

$$\mathcal{B}^{-1} = (1/\mathbf{k}_0^2)\left(v_x^2\mathcal{I} + v_x\mathcal{C}_1 + \mathcal{C}_0\right), \tag{18}$$

where $\mathcal{I}$ is the identity matrix.

Then the determinantal equation (16) can be written as a second-order matrix polynomial:

$$\det\left|v_x^2\mathcal{I} + v_x\mathcal{C}_1 + (\mathcal{C}_0 + \mathcal{A}^{-1})\right| = 0. \tag{19}$$

It can be shown that the solutions of (19) are the eigenvalues of a linear determinantal equation (22) (Colella, 1974) defining for each eigenvector a second one by

$$\mathcal{D}_2 v_x = \mathcal{D}_1, \tag{20}$$

which leads to

$$\begin{pmatrix} -\mathcal{C}_1 & -\mathcal{E} \\ \mathcal{I} & \mathcal{O} \end{pmatrix}\begin{pmatrix} \mathcal{D}_1 \\ \mathcal{D}_2 \end{pmatrix} = v_x\begin{pmatrix} \mathcal{D}_1 \\ \mathcal{D}_2 \end{pmatrix}, \tag{21}$$

where $\mathcal{E} = \mathcal{C}_0 + \mathcal{A}^{-1}$.

Then the linear determinantal equation is given by

$$\det\left|\mathcal{Q} - v_x\mathcal{I}\right| = 0, \tag{22}$$

where $\mathcal{Q}$ is a $4N \times 4N$ matrix given by

$$\mathcal{Q} = \begin{pmatrix} -\mathcal{C}_1 & -\mathcal{E} \\ \mathcal{I} & \mathcal{O} \end{pmatrix} \tag{23}$$

and $\mathcal{O}$ is the null matrix.

The eigenvalues of (19) and (22) are the same (Colella, 1974). For each eigenvalue, an eigenvector with $4N$ components is obtained. As can be seen from (20) and (21), the first $2N$ components $\mathcal{D}_1$ are linearly dependent on the second $2N$ components $\mathcal{D}_2$. Each eigenvalue (tie point) $j = 1, 2, \ldots, 4N$ corresponds to a set of plane waves $\mathbf{D}_j(\mathbf{h}_n)$, $n = 1, 2, \ldots, N$, with amplitudes $D_p(\mathbf{h}_n)$, $p = \pi, \sigma$, which form the ray of the jth tie point. It should be noticed that in a non-coplanar N-beam case the π and σ polarization components are no longer decoupled as in a two-beam case. Thus, according to (11), for each tie point there are D_π and D_σ components excited simultaneously. The $4N$ eigenvalues and eigenvectors can now be calculated by standard methods for which computer programs are available.

The various components of the ray are determined only on a relative basis. The total displacement vector in the crystal is written as

$$\mathbf{D}_{\text{tot}}(\mathbf{r}) = \sum_j^{4N} q_j \sum_n^N \mathbf{D}_j(\mathbf{h}_n)\exp[-2\pi i\mathbf{K}_j(\mathbf{h}_n)\cdot\mathbf{r}], \tag{24}$$

where the q_j's are $4N$ unknown coefficients to be determined by means of the boundary conditions.

2.2.2. *Boundary conditions.* The boundary conditions for an electromagnetic wave propagating through the crystal surface require continuity of the tangential components of the electric and magnetic fields **E** and **H** and for the normal components of the dielectric displacement and magnetic induction **D** and **B**. The latter conditions, however, are not independent of the former, so a total of four scalar equations for the two tangential components of **E** and **H** have to be satisfied. Within the crystal, for each set of plane waves whose wave vectors terminate at the node H_n of the reciprocal lattice, there are $4N$ distinct propagation directions given by $\mathbf{K}_j(\mathbf{h}_n)$ of (17) with the eigenvalues of (22) where n is fixed and j runs over all the $4N$ tie points. For the waves inside the crystal, only the components of the displacement vectors $\mathbf{D}_j(\mathbf{h}_n)$ will be involved in the final equations since the components of the electric and magnetic fields will be eliminated through the relations

$$\mathbf{E}_j(\mathbf{h}_n) = \varepsilon_{jn}^{-1}\mathbf{D}_j(\mathbf{h}_n) \tag{25}$$

$$\mathbf{H}_j(\mathbf{h}_n) = \varepsilon_{jn}^{-1}[\mathbf{K}_j(\mathbf{h}_n) \times \mathbf{D}_j(\mathbf{h}_n)]. \tag{26}$$

The ratio

$$\varepsilon_{jn} = \mathbf{K}_j(\mathbf{h}_n)^2/\mathbf{k}_0^2 \tag{27}$$

is the individual permittivity for each plane wave $\mathbf{D}_j(\mathbf{h}_n)$.

The boundary condition at the entrance and exit surfaces of a crystal slab of thickness d can now be written as (Schwegle, 1993)

$$\begin{aligned}\left[\mathbf{E}_0\delta_n^1\delta_x^0 + \mathbf{E}(\mathbf{h}_n)\right]_t &= \left[\sum_j^{4N} q_j\varepsilon_{jn}^{-1}C_{jn}\mathbf{D}_j(\mathbf{h}_n)\right]_t \\ \left[\mathbf{H}_0\delta_n^1\delta_x^0 + \mathbf{H}(\mathbf{h}_n)\right]_t &= \left[\sum_j^{4N} q_j C_{jn}\mathbf{H}_j(\mathbf{h}_n)\right]_t.\end{aligned} \tag{28}$$

On the left-hand side are the field vectors of the waves in vacuum, on the right those of the crystal waves.

Suffix t ($t = y, z$) stands for their tangential components. $\mathbf{E}_0$ and $\mathbf{H}_0$ are the given field vectors of the incident beam, which have to be taken into account only at the entrance surface (δ_x^0) and only for the **0** waves with $\mathbf{h}_n = \mathbf{0}$ for $n = 1$ (δ_n^1). $\mathbf{E}(\mathbf{h}_n)$ and $\mathbf{H}(\mathbf{h}_n)$ are those of the reflected diffracted waves at the entrance surface and those of the transmitted diffracted waves at the exit surface. $\mathbf{E}(\mathbf{0})$ and $\mathbf{H}(\mathbf{0})$ are those of the specular reflected and forward-transmitted waves (see Fig. 1).

The absolute phases and amplitudes of the waves at both surfaces are matched by the factor

$$C_{jn} = \exp[-2\pi i \mathbf{K}_j(\mathbf{h}_n) \cdot \mathbf{x}], \quad |x| = d, \tag{29}$$

which is equal to one at the entrance surface where $x = 0$.

Since there are two independent scalar equations for each of the two tangential components of $\mathbf{E}$ and $\mathbf{H}$ for each r.l.v. $\mathbf{h}_n$ on both surfaces, we have a total of $8N$ equations with $8N$ unknowns: the $4N$ coefficients q_j of the waves in the crystal and the $4N$ transverse components of the electric field $\mathbf{E}(\mathbf{h}_n)$ of all the vacuum waves. It is, however, possible to eliminate the components of the vacuum waves at each surface by using the continuity of the normal component of the $\mathbf{D}_j(\mathbf{h}_n)$ and substituting (26) into (28). Thus, we are left with a system of $4N$ linear complex equations for the unknown q_j's that determine the crystal waves.

With the q_j's known, it is possible to calculate the (x, y, z) components of the amplitudes of the vacuum waves using again the continuity conditions of $\mathbf{E}$ and $\mathbf{D}$.

$$[\mathbf{E}(\mathbf{h}_n)]_t = \left[\sum_j^{4N} q_j C_{jn} \varepsilon_{jn}^{-1} \mathbf{D}_j(\mathbf{h}_n) - \mathbf{E}_0 \delta_n^1 \delta_x^0\right]_t, \quad t = y, z, \tag{30}$$

$$[\mathbf{E}(\mathbf{h}_n)]_x = \left[\sum_j^{4N} q_j C_{jn} \mathbf{D}_j(\mathbf{h}_n) - \mathbf{E}_0 \delta_n^1 \delta_x^0\right]_x. \tag{31}$$

In the above sections, we discussed the solutions for the complete set of reflected and transmitted waves in the case of the plane-wave approximation. In ordinary diffraction experiments when only the strong Bragg reflected and Laue transmitted rays have to be considered, linearization of the eigenvalue equation is allowed. It should be noted, however, that both types of wave may exist simultaneously – in total $N - 1$ such rays, where the forward-transmitted ray is not included. Within this approximation, only $2N$ tie points (eigenvalues) result, *i.e.* half of the waves are neglected. Consequently, only half of the boundary-condition equations are relevant. These are the conditions at the exit surface for the waves of the Bragg reflected rays and at the entrance surface for the waves of the Laue transmitted rays since the Bragg and Laue rays in vacuum are formed of the rays $\mathbf{S}_r(\mathbf{h}_n)$ and $\mathbf{S}_t(\mathbf{h}_n)$, respectively (see Fig. 1) (Hümmer & Billy, 1982; Weckert & Hümmer, 1990).

2.2.3. *Calculation of reflectivity and transmissivity.* By means of the known amplitudes of the vacuum waves at the entrance and exit surface, it is possible to calculate the reflected and transmitted intensities. In the case of asymmetric diffraction geometry, where the lattice planes are not parallel or normal to the crystal surface, the cross section of the reflected and transmitted beams will be changed. In order to satisfy the condition of conservation of energy, as the intensity is defined as the energy flow density, asymmetry factors $\gamma(\mathbf{h})_n$ have to be introduced that take this change into account (von Laue, 1960). Accordingly, the reflected or transmitted intensity is calculated as

$$I_{\mathbf{h}_n} = [|\gamma(\mathbf{h}_n)|/\gamma_0]\left\{\sum_{u=x,y,z} [\mathbf{E}(\mathbf{h}_n)]_u [\mathbf{E}^*(\mathbf{h}_n)]_u\right\} \Big/ \mathbf{E}_0 \mathbf{E}_0^*, \tag{32}$$

where $\gamma(\mathbf{h}_n)$ are the direction cosines between the vacuum wave vectors $\mathbf{k}(\mathbf{h}_n)$ and the surface normal, γ_0 that of the incident beam. $I_{\mathbf{h}_n}$ represents the intensity of the reflected vacuum beams (reflectivity $R_{\mathbf{h}_n}$) in Bragg geometry taking the amplitudes at the entrance surface. Equivalently, in Laue geometry, $I_{\mathbf{h}_n}$ represents the intensity of the transmitted vacuum beam (transmissivity $T_{\mathbf{h}_n}$) taking the amplitudes at the exit surface where the C_{jn} have to be taken from (29).

3. Phase determination by multiple-beam diffraction

3.1. *Introductory remarks*

The basic idea of how N-beam diffraction can be used for physical determination of phase relations originates from Lipscomb (1949). He proposed exploiting the diffracted intensity when two Bragg reflections are simultaneously excited. This situation is called three-beam diffraction since, besides the forward-transmitted ray, two additional diffracted rays, in total three strong rays, are simultaneously propagated (*cf.* Fig. 3). More

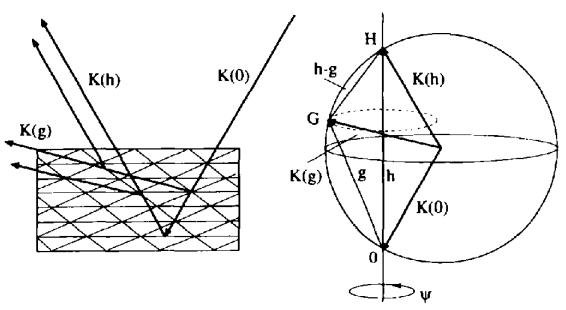

Fig. 3. Three-beam case: schematical representation in crystal and reciprocal space with primary reflection **h** and secondary reflection **g**; for simplicity, all three **K** vectors are drawn coplanar.

generally, N-beam diffraction occurs when, apart from the origin, $N-1$ nodes of the reciprocal lattice lie very close to or on the Ewald sphere.

Experimentally, N-beam diffraction can be achieved systematically by the azimuthal Ψ-scan technique. In this experiment, the crystal is first aligned for a selected reflection, called the primary reflection, to generate an ordinary two-beam case. Then the crystal is rotated about this diffraction vector (r.l.v.), which means rotated about the normal of the corresponding lattice planes, keeping the Bragg angle of the primary reflection constant and monitoring its intensity. As the crystal is rotated, in general, several nodes of the reciprocal lattice simultaneously pass through the Ewald sphere. In favourable cases, exactly one additional secondary reflection is excited, which leads to a distinct three-beam case. Renninger (1937) used the Ψ-scan technique for the investigation of multiple-beam diffraction effects. Later, it was extensively used to study extinction effects (*Aufhellung* and *Umweganregung*) (*e.g.* Moon & Shull, 1964) in multiple-beam cases.

To specify nomenclature, in the following the primary reflection is denoted by its r.l.v. **h**, around which the azimuthal Ψ scan is carried out. The additional secondary reflection is denoted by **g**, the related three-beam case by **0/h/g** and a four-beam case by **0/h/g/g'**, correspondingly.

A rough estimate of the interaction of the excited waves in multiple diffraction shows that the intensities of the diffracted rays are affected by the relative phases of the structure factors involved. We concentrate on the three-beam case (Lipscomb, 1949) shown in Fig. 3. The incident beam simultaneously excites two diffracted waves **h** and **g** denoted by their corresponding r.l.v.'s. With respect to an arbitrarily chosen origin of the unit cell, their phases are given by $\varphi(\mathbf{h})$ and $\varphi(\mathbf{g})$. Since the difference vector $\pm(\mathbf{h}-\mathbf{g})$ has to be also a vector of the reciprocal lattice, the **g** wave is diffracted into the direction of the **h** wave by $\mathbf{h}-\mathbf{g}$ and *vice versa*. In the $\mathbf{K}(\mathbf{h})$ direction, two waves are superimposed, namely the primary diffracted wave **h** and a wave that is diffracted at the lattice planes of **g** and $\mathbf{h}-\mathbf{g}$ called detour excited (*Umweg*) wave, whose phase is consequently given by $\varphi(\mathbf{g})+\varphi(\mathbf{h}-\mathbf{g})$.

The existence of this *Umweg* wave was already proved in 1937 by Renninger. He observed that simultaneously excited reflections drastically enhance the intensity of a weak reflection (*Umweganregung* peaks) by monitoring the 'forbidden' 222 reflection of diamond as the primary reflection in a Ψ-scan experiment.

Interference of the coherent primary diffracted and *Umweg* waves leads to a resultant intensity that depends on their phase difference:

$$\Phi_{3\pm}=\pm[\varphi(\mathbf{g})+\varphi(\mathbf{h}-\mathbf{g})-\varphi(\mathbf{h})],\quad \Phi_{3+}=-\Phi_{3-}. \tag{33}$$

It is well known that the resulting intensity due to the interference of two waves with amplitudes A_1 and A_2 and phases α_1 and α_2 is governed by the cosine of $\pm(\alpha_2-\alpha_1)$:

$$\begin{aligned} I &= |A_1 \exp i\alpha_1 + A_2 \exp i\alpha_2|^2 \\ &= A_1^2 + A_2^2 + 2A_1A_2\cos(\alpha_2-\alpha_1). \end{aligned} \tag{34}$$

It turns out that the phase difference Φ_3, a so-called triplet phase relationship, is independent of an arbitrarily chosen origin. Therefore, it is a structure-invariant quantity. In fact, only structure invariants are measurable quantities. Hence, it should be possible to exploit the three-beam intensities for the experimental determination of triplet phases.

Now, the distinct advantage of the Ψ-scan technique is obvious. As the primary reflection remains in its reflection position, the two-beam intensity serves as a reference level that is modulated when the *Umweg* wave is continuously turned on and off scanning through a three-beam position. Thus, the intensity change due to the interference contrast of the primary reference beam contains information on the triplet phase.

This experimental technique is very similar to the technique used to produce a hologram, where the intensity of a reference beam is modulated by the scattered waves. The interference pattern contains the phase information.

These simple considerations do not explain the experimentally observed three-beam diffraction profiles. In order to understand the actually observed profiles and the underlying diffraction physics, a modified two-beam approximation is applied, the so-called first-order Bethe approximation, commonly used in electron multibeam diffraction. It should be pointed out, however, that it is very difficult to use this approximation for a quantitative analysis of multiple-diffraction effects, in particular, for the quantitative analysis of the various properties like phase-independent *Aufhellung* and *Umweganregung* effects, *Pendellösung* effects and the effects of different polarization states. There are several authors who have done a considerable amount of work elaborating the analytical solution of multiple-beam diffraction using the Bethe approximation (Juretschke, 1982*a*,*b*; Høier & Marthinsen, 1983; Chang, 1984). The present authors prefer computational simulations. However, simple versions of the two-beam approximation are used to obtain an insight into the underlying diffraction physics. The quantitative computer analysis discussed later is based on the plane-wave dynamical theory using boundary conditions for parallel-sided crystal slabs.

Thorkildsen (1987) published the solution of dynamical three-beam diffraction by means of Takagi–Taupin equations for a parallelepiped-shaped crystal. The extension of this work could be a way to solve the problem for arbitrarily shaped crystals.

3.2. *Simplified two-beam approximation*

In order to gain a better understanding of multiple diffraction profiles and the information they give about the multiplet invariant phases involved, it is worth discussing their main properties by means of a first-order Bethe approximation.

3.2.1. *Three-beam case.* To make the discussion as simple as possible without losing general physical arguments, the coupling between the π and σ polarization components is neglected, *i.e.* the $\boldsymbol{\pi}\cdot\boldsymbol{\sigma}$ scalar products in (12) and (13) are set equal to zero, as they are in a coplanar three-beam case. Then (12) and (13) are reduced to equivalent non-coupled equations for only one polarization component (Hümmer & Billy, 1986). The effects that may occur by the use of linearly polarized synchrotron radiation are discussed in §3.3. With the above approximation, using (10),

$$R(\mathbf{h}_m)^{-1} = \{k_0^2/\mathbf{K}(\mathbf{h}_m)^2 - [1-\chi(\mathbf{0})]\} \simeq [\mathbf{K}_0^2 - \mathbf{K}(\mathbf{h}_m)^2]/\mathbf{K}(\mathbf{h}_m)^2, \quad (35)$$

each equation (12) and (13) can be written in matrix notation:

$$\begin{pmatrix} R(\mathbf{0})^{-1} & \alpha_{0h}\chi(-\mathbf{h}) & \alpha_{0g}\chi(-\mathbf{g}) \\ \alpha_{0h}\chi(\mathbf{h}) & R(\mathbf{h})^{-1} & \alpha_{hg}\chi(\mathbf{h}-\mathbf{g}) \\ \alpha_{0g}\chi(\mathbf{g}) & \alpha_{hg}\chi(\mathbf{g}-\mathbf{h}) & R(\mathbf{g})^{-1} \end{pmatrix} \begin{pmatrix} \mathbf{D}(\mathbf{0}) \\ \mathbf{D}(\mathbf{h}) \\ \mathbf{D}(\mathbf{g}) \end{pmatrix} = 0. \quad (36)$$

The α_{nm} represent geometrical coupling factors that result from the scalar products $\boldsymbol{\pi}_n\cdot\boldsymbol{\pi}_m$ or $\boldsymbol{\sigma}_n\cdot\boldsymbol{\sigma}_m$.

To solve these equations for the ratio $\mathbf{D}(\mathbf{h})/\mathbf{D}(\mathbf{0})$, a perturbational approach, called the Bethe potential method (Bethe, 1928) is adopted. The amplitude of $\mathbf{D}(\mathbf{g})$ may be expressed in terms of $\mathbf{D}(\mathbf{0})$ and $\mathbf{D}(\mathbf{h})$ using the third equation of (36). Upon insertion of this expression in the second equation of (36), for instance, and solving for $\mathbf{D}(\mathbf{h})/\mathbf{D}(\mathbf{0})$ using (4), we get

$$\begin{aligned}\mathbf{D}(\mathbf{h})/\mathbf{D}(\mathbf{0}) &= N^{-1}R(\mathbf{h})[\alpha_{0h}\Gamma F(\mathbf{h}) \\ &\quad + R(\mathbf{g})\alpha_{0g}\alpha_{hg}\Gamma^2 F(\mathbf{g})F(\mathbf{h}-\mathbf{g})] \\ &= N^{-1}R(\mathbf{h})F_{\text{eff}}, \end{aligned} \quad (37)$$

where $N = 1 - \alpha_{hg}^2[\Gamma F(\mathbf{h}-\mathbf{g})]^2 R(\mathbf{g})R(\mathbf{h})$. This result should be interpreted as follows. The amplitude in the two-beam case, given by $\mathbf{D}_2(\mathbf{h})/\mathbf{D}(\mathbf{0}) = N^{-1}R(\mathbf{h})\alpha_{0h}\Gamma F(\mathbf{h})$, the first term of (37) (*i.e.* no secondary reflections are excited) is modified by higher-order terms owing to excitation of other reflections. Obviously, if $R(\mathbf{h})$ is negligibly small, *i.e.* Bragg's law for the $\mathbf{h}$ reflection is not fulfilled, then no intensity can be observed in the direction of $\mathbf{K}(\mathbf{h})$. This is also true even though other wave fields are excited. In this case, Bragg's law for the scattering of the secondary $\mathbf{g}$ reflection into the $\mathbf{h}$ reflection is not fulfilled since the point of the coupling vector $\mathbf{h}-\mathbf{g}$ does not lie on the Ewald sphere. Thus, the basic requirement in order to observe the modification of the intensity of the $\mathbf{h}$ reflection by additional excitation of other reflections is to keep $\mathbf{h}$ precisely on the Ewald sphere during the Ψ scan.

Equation (37) confirms in part the basic considerations by Lipscomb (1949). The resulting amplitude of the wave $\mathbf{D}(\mathbf{h})$ is given by a superposition of two waves: the directly diffracted wave governed by the structure factor $F(\mathbf{h})$ and the *Umweg* wave governed by the product of structure factors $F(\mathbf{g})F(\mathbf{h}-\mathbf{g})$. However, the resonance term $R(\mathbf{g})$ determines not only the amplitude but also the phase of the *Umweg* wave. It causes a phase shift of 180° by scanning through a three-beam position. This behaviour can be seen by means of the Ewald construction, where the radius of the Ewald sphere is given by $|\mathbf{K}_0|$. We assume that the azimuthal scan is carried out so that the point of $\mathbf{g}$ passes the Ewald sphere from inside to outside, in short 'in–out' scan. At the beginning when $\mathbf{g}$ terminates inside, then $|\mathbf{K}(\mathbf{g})| < |\mathbf{K}_0|$ since $\mathbf{K}(\mathbf{g}) = \mathbf{K}_0 + \mathbf{g}$ (*cf.* Fig. 4) and $R(\mathbf{g})$ is positive. When the point of $\mathbf{g}$ approaches the Ewald sphere, $R(\mathbf{g})$ gets larger as the the denominator of $R(\mathbf{g})$ gets smaller, *i.e.* the amplitude of the *Umweg* wave increases. It has its maximum value when the point of $\mathbf{g}$ exactly lies on the Ewald sphere. When it leaves the Ewald sphere, again the magnitude of $R(\mathbf{g})$ and therefore the amplitude of the *Umweg* wave decreases. However, $R(\mathbf{g})$ has changed its sign, since $|\mathbf{K}(\mathbf{g})| > |\mathbf{K}_0|$ when $\mathbf{g}$ terminates outside (*cf.* Fig. 4). Changing its sign, $R(\mathbf{g})$ causes an additional phase shift $\Delta(\Psi)$ by 180°, which is the resonance phase shift. $R(\mathbf{g})$ is a Lorentzian where it is taken into account that because of absorption the wave vectors are complex quantities. The behaviour of the amplitude and the phase shift of the *Umweg* wave during the Ψ scan is shown schematically in Fig. 5. A kinematical approach for the explanation of this resonance phase shift is given by Woolfson & Fan (1995).

To specify nomenclature, henceforth, all the Ψ-scan profiles refer to an 'in–out' scan: $\Psi = 0$ marks the exact geometrical three-beam position, for $\Psi < 0$ the point of $\mathbf{g}$ is inside, for $\Psi > 0$ it is outside the Ewald sphere.

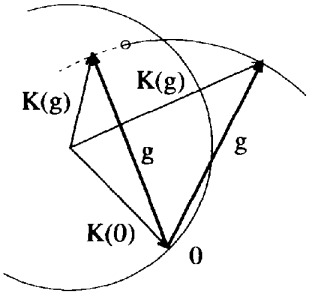

Fig. 4. Schematic drawing illustrating the change of sign of the resonance term $R(\mathbf{g})$.

$\Delta(\Psi)$ varies from 0 to 180° for an 'in–out' Ψ-rotation sense. If the rotation sense is reversed (out–in), the resonance phase shifts from 180 to 0°. Therefore, it is important to know the rotation sense for the exploitation of the triplet phase from the three-beam diffraction profiles (Chang, 1982).

Now, the fundamental features of the integrated intensity of a Ψ-scan profile can easily be calculated by means of (37). In a first-order approximation, except for a range very close to the three-beam position, N may be taken as a constant, $N \simeq 1$. The range of validity for the first-order solution has been discussed in detail by Juretschke (1984), where ξ_L in Juretschke's paper is equivalent to $R(\mathbf{g})^{-1}$. It depends on the magnitudes of the structure factors involved. Then, the integrated three-beam intensity is approximately given by

$$I_h(\Psi) \simeq |F_{\text{eff}}|^2. \tag{38}$$

We introduce the magnitude $|R_g(\Psi)|$ and the phase $\Delta(\Psi)$ of the resonance term,

$$R(\mathbf{g}) = |R_g(\Psi)| \exp[i\Delta(\Psi)], \tag{39}$$

and the magnitude and the phase of the structure factors involved

$$F(\mathbf{h}_n) = |F(\mathbf{h}_n)| \exp[i\varphi(\mathbf{h}_n)], \quad \mathbf{h}_n = \mathbf{h}, \mathbf{g}, \mathbf{h} - \mathbf{g}. \tag{40}$$

From (34) and (37), $I_h(\Psi)$ is given by

$$I_h(\Psi) \simeq A_1^2 + A_2^2 + 2A_1A_2 \times \cos\{[\varphi(\mathbf{g}) + \varphi(\mathbf{h} - \mathbf{g}) + \Delta(\Psi)] - \varphi(\mathbf{h})\}, \tag{41}$$

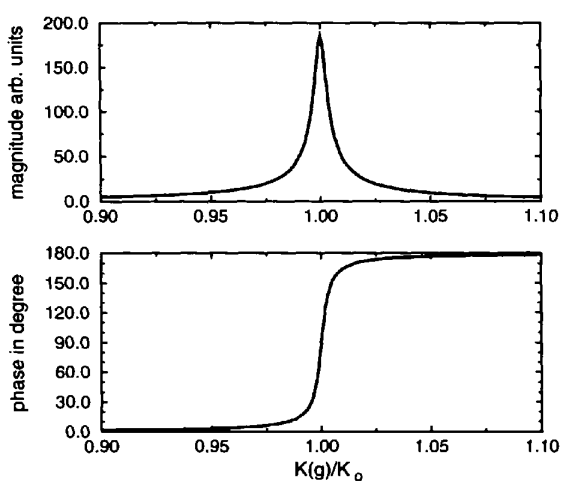

Fig. 5. Schematic drawing of amplitude (magnitude) and phase of the *Umweg* wave close to the three-beam position.

where

$$A_1 = \alpha_{0h}\Gamma|F(\mathbf{h})|$$
$$A_2 = \alpha_{0g}\alpha_{hg}\Gamma^2|R_g(\Psi)||F(\mathbf{g})||F(\mathbf{h} - \mathbf{g})|. \tag{42}$$

Hence, the interference of the primary wave and the *Umweg* wave is governed by the total phase $\Phi_{\text{tot}}(\Psi)$, which according to (33) and (41) is given by

$$\Phi_{\text{tot}}(\Psi) = \pm[\Phi_{3+} + \Delta(\Psi)] = \mp[\Phi_{3-} - \Delta(\Psi)]. \tag{43}$$

It should be noticed that the resonance phase shift was not considered by Lipscomb (1949). It is a result of the self-consistent dynamical interaction. In fact, such a phase shift occurs also in two-beam diffraction rocking the crystal through a two-beam diffraction position. Ewald (1917, 1965) in his work on crystal optics of X-rays has previously pointed out that Bragg diffraction is a spatial resonance phenomenon. The resonance term may be regarded as the efficiency of the crystal to convert a given amplitude of polarization **P** into the field amplitude **D**. If Bragg's diffraction condition is fulfilled, *i.e.* $\mathbf{K}(\mathbf{h})^2 \simeq K_0^2$, this efficiency will be optimum. Thus, the diffraction will be optimum when the spatial periodicity of the incoming wave matches the spatial periodicity of the lattice. At this stage of the discussion, it should be stressed once again that the three-beam intensity depends not only on the cosine of the triplet phase but also on the cosine of the total phase $\Phi_{\text{tot}}(\Psi)$, which contains the resonance phase shift $\Delta(\Psi)$. Owing to this fact, the three-beam intensity depends also on the sign of $|\Phi_3|$ with $0 \leq |\Phi_3| \leq 180°$.

3.2.2. *Three-beam interference profiles.* In the previous section, we have already considered the three-beam interference between the directly diffracted wave and the *Umweg* wave and their phase difference. Let us now find the principal features of three-beam profiles for different triplet phases using the azimuthal Ψ-scan technique.

Suppose the triplet phase of a three-beam case **0/h/g** is zero: $\Phi_{3+} = 0°$. Then, at the beginning of the Ψ scan, $\Delta(\Psi) \simeq 0$ and $\Phi_{\text{tot}}(\Psi) = 0$. The amplitude of the *Umweg* wave is very small and the two-beam intensity $I_h^{(2)}$ is observed. With a scan towards the three-beam position, the amplitude of the *Umweg* wave increases. The primary wave and the *Umweg* wave interfere in a constructive way that leads to an increase in the resultant amplitude of $\mathbf{D}(\mathbf{h})$. Thus, the intensity is increased. Very near to the three-beam position, $\Delta(\Psi)$ shifts very rapidly from 0 to 180°, then $\Phi_{\text{tot}}(\Psi) = 180°$. This means that the interference becomes destructive and the two-beam intensity is decreased. At the end of the Ψ scan when the amplitude of the *Umweg* wave gets smaller, the two-beam intensity is observed again. A calculated profile of this type is shown in Fig. 6(*a*). It reflects the fact that $\cos[\Phi_{\text{tot}}(\Psi)]$ changes its sign as $\Phi_{\text{tot}}(\Psi)$ varies from 0 to 180°. In the case that $\Phi_{3+} = 180°$, the Ψ-scan profile

will be reversed with respect to $\Psi = 0$, as $\Phi_{tot}(\Psi)$ varies from 180 to 360° and thus $\cos[\Phi_{tot}(\Psi)]$ changes from negative to positive values.

For $\Phi_{3+} = +90$ or $-90°$, it is important to notice that different Ψ-scan profiles result. Therefore, it is possible to distinguish the two cases experimentally. For $\Phi_{3+} = +90°$, $\cos[\Phi_{tot}(\Psi)]$ is always negative scanning through a three-beam position; for $\Phi_{3+} = -90°$, it is always positive. This means that the interference term, the third term of (41), is symmetric around the three-beam position $\Psi = 0$. Therefore, a symmetric decrease or increase of the two-beam intensity is expected owing to destructive or constructive interference, respectively.

Of course, if we had taken the negative sign in (43), we would have obtained the same type of profile. This is also true if we had taken the negative sign for the definition of the triplet phase in (33), *i.e.* $-\Phi_{3-}$ instead of Φ_{3+}. Both definitions lead to the same type of profile. Hence, there is no ambiguity with respect to the experimental phase determination from the Ψ-scan profiles, since one gets either Φ_{3+} or $-\Phi_{3-}$.

It remains to discuss the diffraction profiles if Φ_{3+} equals ±45 or ±135°. Their principal features must be something intermediate between 0 and ±90 or ±90 and 180°, as can be seen from Figs. 6(*b*) and (*d*). For instance, if $\Phi_{3+} = +45°$, then at first a smaller region of constructive interference is observed, as long as $\cos[45° + \Delta(\Psi)]$ is positive. Since the amplitude of the *Umweg* waves reaches its maximum for $\Phi_{tot}(\Psi) = 45 + 90 = 135°$, in that case, a larger region of destructive interference is to be expected and the increase of the two-beam intensity is weaker than the decrease.

A summary outline of (integrated) three-beam profiles is given in Fig. 6. Because of its experimental relevance, profiles of triplet phases having opposite sign are compared. In the following, we use Φ_{3+} as a definition for the triplet phase [*cf.* (33)] and use the short-hand notation Φ_3.

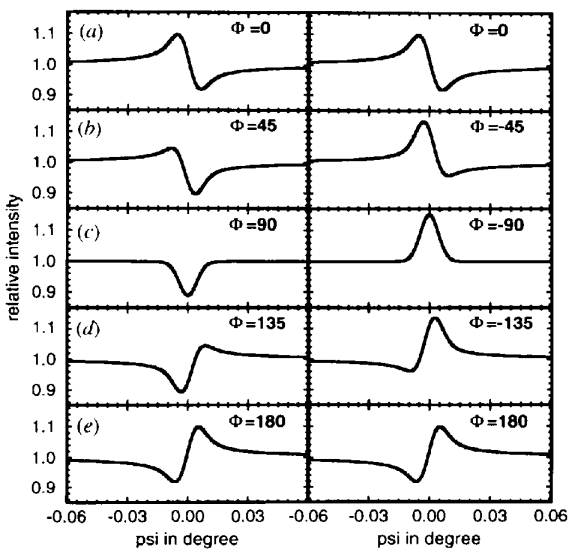

Fig. 6. Interference profiles for different triplet phases.

3.2.3. *Four-beam case.* The feasibility of experimental determination of multiplet phase invariants by means of four-beam Ψ-scan experiments was investigated both theoretically and experimentally (Post, Gong, Kern & Ladell, 1986; Chang *et al.*, 1988; Hümmer, Bondza & Weckert, 1991). There are two types of four-beam case: systematic ones if the Ψ-rotation axis coincides with a symmetry direction of the reciprocal lattice and accidental ones for special wavelengths if two arbitrary three-beam cases occur at the same Ψ position. The modified two-beam solution (44) shows that the Ψ-scan profiles depend on two first-order triplet phase terms and two second-order quartet phase terms and a second-order phase-independent extinction term. Analogous to the three-beam case, the crystal is rotated about **h**. The two additional secondary reflections are denoted by **g** and **g**′. The two-beam approximation calculated analogously to the case of three-beam diffraction gives

$$\begin{aligned} D(\mathbf{h})/D(\mathbf{0}) = N^{-1}R(\mathbf{h})\Gamma[&F(\mathbf{h}) \\ &+ \Gamma R(\mathbf{g})\alpha_{0g}\alpha_{hg}F(\mathbf{g})F(\mathbf{h}-\mathbf{g}) \\ &+ \Gamma R(\mathbf{g}')\alpha_{0g'}\alpha_{hg'}F(\mathbf{g}')F(\mathbf{h}-\mathbf{g}') \\ &+ \Gamma^2 R(\mathbf{g})R(\mathbf{g}')\alpha_{0g}\alpha_{gg'}\alpha_{hg'} \\ &\times F(\mathbf{g})F(\mathbf{g}'-\mathbf{g})F(\mathbf{h}-\mathbf{g}') \\ &+ \Gamma^2 R(\mathbf{g})R(\mathbf{g}')\alpha_{0g'}\alpha_{gg'}\alpha_{hg} \\ &\times F(\mathbf{g}')F(\mathbf{g}-\mathbf{g}')F(\mathbf{h}-\mathbf{g}) \\ &- \Gamma^2 R(\mathbf{g})R(\mathbf{g}')\alpha_{0h}\alpha_{gg'}^2 \\ &\times F(\mathbf{h})F^2(\mathbf{g}-\mathbf{g}')], \end{aligned} \tag{44}$$

where N^{-1} is equal to one plus higher-order phase-independent terms in Γ^n. The magnitude of the terms in (44) is governed by the power n of Γ ($\Gamma \simeq 10^{-7}$).

The first-order triplet terms represent *Umweg* waves generated by twofold reflection at the lattice plane of **g** and **h** − **g** or **g**′ and **h** − **g**′, respectively, which are superimposed on the primary diffracted wave. Consequently, two triplet phase invariants are involved:

$$\begin{aligned} \Phi_3 &= -\varphi(\mathbf{h}) + \varphi(\mathbf{g}) + \varphi(\mathbf{h}-\mathbf{g}) \\ \Phi_3' &= -\varphi(\mathbf{h}) + \varphi(\mathbf{g}') + \varphi(\mathbf{h}-\mathbf{g}'). \end{aligned} \tag{45}$$

The second-order quartet terms represent *Umweg* waves generated by threefold reflection at the lattice planes of **g**, **g**′ − **g**, **h** − **g**′ and **g**′, **g** − **g**′, **h** − **g**, which are superimposed on the primary diffracted wave. Accordingly, in addition two quartet phase invariants are involved:

$$\begin{aligned} \Phi_4 &= -\varphi(\mathbf{h}) + \varphi(\mathbf{g}) + \varphi(\mathbf{g}'-\mathbf{g}) + \varphi(\mathbf{h}-\mathbf{g}') \\ \Phi_4' &= -\varphi(\mathbf{h}) + \varphi(\mathbf{g}') + \varphi(\mathbf{g}-\mathbf{g}') + \varphi(\mathbf{h}-\mathbf{g}). \end{aligned} \tag{46}$$

The fifth term is a phase-independent second-order extinction term, which can be interpreted analogously to the primary extinction in a two-beam case. It leads to a phase-independent modification of the two-beam intensity. It should be noticed that only those structure-factor multiplets that contain $F(\mathbf{h})$ are relevant for the modulation of the primary reflection scanning Ψ about $\mathbf{h}$.

Systematic four-beam cases occur if $\mathbf{h}$ coincides with a symmetry direction of the reciprocal lattice. The symmetry of the reciprocal lattice (holohedry) of each crystal family ensures that each lattice symmetry direction carries symmetry operation $2/m$, except for the [111] direction in the rhombohedral and cubic crystal system. If, simultaneously, $\mathbf{h}$ coincides with a twofold axis of the crystal structure, then special relations exist between the two triplet phases Φ_3 and Φ'_3, and between the two quartet phases Φ_4 and Φ'_4.

As can be seen from Fig. 7, where the reciprocal-lattice vectors involved in Φ_3 and Φ'_3 are drawn with respect to their common origin, $\mathbf{g}$ and $\mathbf{g}'$ are symmetrically related to $\mathbf{h} - \mathbf{g}'$ and $\mathbf{h} - \mathbf{g}$, respectively. If $\mathbf{h}$ coincides with a twofold symmetry axis or a twofold screw axis 2_1 of the structure, then $\varphi(\mathbf{g}) = \varphi(\mathbf{h} - \mathbf{g}')$ and $\varphi(\mathbf{g}') = \varphi(\mathbf{h} - \mathbf{g})$ and, therefore, $\Phi_3 = \Phi'_3$. This condition can only be fulfilled in space groups with rotations, roto-inversions and corresponding screw axis 2, 4, $\bar{4}$, 6. It is not possible in space groups containing only operations $\bar{1}$, m, $\bar{3}$, $\bar{6}$, 3_1, 3_2 and glide planes (Hümmer, Bondza & Weckert, 1991).

If the Ψ scan is carried out about the opposite parallel side of the trapezoid, namely around $(\mathbf{g}' - \mathbf{g})$, taking the $(\mathbf{g}' - \mathbf{g})$ reflection as a primary one (*cf.* Fig. 7), then the relevant triplet phase relationships are given by

$$\begin{aligned} \hat{\Phi}_3 &= -\varphi(\mathbf{g}' - \mathbf{g}) + \varphi(\mathbf{h} - \mathbf{g}) + \varphi(\mathbf{g}' - \mathbf{h}) \\ \hat{\Phi}'_3 &= -\varphi(\mathbf{g}' - \mathbf{g}) + \varphi(-\mathbf{g}) + \varphi(\mathbf{g}'). \end{aligned} \tag{47}$$

By means of two Ψ-scan experiments about the parallel sides of the trapezoid, provided that $\mathbf{h}$, and $\mathbf{g}' - \mathbf{g}$, coincide with a twofold axis 2 or screw axis 2_1 of the structure, the quartet phases can be calculated by the measured triplet phases Φ_3 and $\hat{\Phi}_3$. They are given by $\Phi_4 = \Phi_3 - \hat{\Phi}_3$; $\Phi'_4 = \Phi'_3 + \hat{\Phi}_3$.

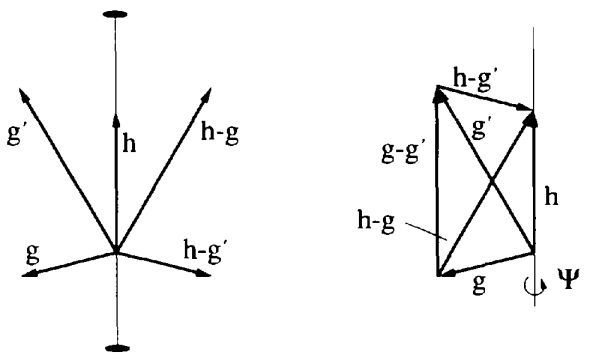

Fig. 7. Reciprocal-lattice vectors for a systematic four-beam case drawn with respect to a common origin (left) and their mutual orientation in a four-beam Ψ-scan diffraction experiment (right).

In the event that the Ψ-rotation axis coincides with the non-parallel sides of the trapezoid or with one of its diagonals, no such relations between the invariant phases can be found. Moreover, with one of the diagonals taken as the Ψ-rotation axis, the two other reciprocal-lattice points pass through the Ewald sphere with different rotation sense, *i.e.* one is at an in–out position the other at an out–in position (Post, Gong, Kern & Ladell, 1986). Such Ψ-scan experiments would give rise to complicated profiles and consequently the extraction of phases would become very difficult.

Detailed computational analysis and experimental investigations (Hümmer, Bondza & Weckert, 1991) have shown that the four-beam diffraction profiles are dominated by the triplet phases as the two-beam modulation due to the quartet phase terms is of the order of Γ weaker than that due to the triplet phase terms [*cf.* (44)]. For accidental four-beam cases, which may happen for selected wavelengths, the two triplet phases involved generally have different values. Then, the Ψ-scan profiles are essentially a superposition of two three-beam profiles of different triplet phases. In that case, it is generally impossible to determine the unknown triplets experimentally. However, it is expected that the interference effects in systematic symmetrical four-beam cases with two equal triplet phases are enhanced. In that way, experimental phase determination may be easier, as shown by Huang, Wang & Chang (1994).

3.3. *Polarization effects*

For simplicity in §3.2, the coupling between the π and σ polarization components were neglected. Now the Bethe approach is applied to (12) and (13) without these restrictions. The polarization vectors $\boldsymbol{\pi}_n$ and $\boldsymbol{\sigma}_n$ can be arbitrarily aligned. It is convenient, however, to regard all $\boldsymbol{\pi}_n$ components lying in the plane of the incident beam and the primary diffracted beam shown in Fig. 2 for a three-beam case.

The polarization state of the incident ray is represented by

$$\mathbf{E}_0 = E_0(\boldsymbol{\pi}_0 + ib\boldsymbol{\sigma}_0), \tag{48}$$

where b is the ellipticity parameter $(-1 \leq b \leq +1)$; $b = \pm 1$ represents right and left circular polarization, $b = 0$ linear polarization. Then, the result can be best represented by means of the flow diagram of Fig. 8 (Schwegle, 1993) for the geometrical arrangement shown in Fig. 2. On the left-hand side, there are the input components of the incident beam, on the right, the output components of the diffracted beam of the reference two-beam case $\mathbf{0}/\mathbf{h}$. In terms of two-beam approximation, the couplings between the input and output are decomposed into the directly diffracted waves D and the various *Umweg* waves U. According to the definitions of the

Table 1. *Overview of possible combinations of signs of the Umweg waves*

Case	$\boldsymbol{\pi}_0\boldsymbol{\pi}_h$	$\boldsymbol{\pi}_0\boldsymbol{\pi}_g\boldsymbol{\pi}_g\boldsymbol{\pi}_h$	$\boldsymbol{\pi}_0\boldsymbol{\sigma}_g\boldsymbol{\sigma}_g\boldsymbol{\pi}_h$	
1	+	+	+	No anomalous asymmetry
2	+	−	+	Anomalous asymmetry possible
3	+	+	−	Anomalous asymmetry possible
4	−	−	−	No anomalous asymmetry
5	−	−	+	Anomalous asymmetry possible
6	−	+	−	Anomalous asymmetry possible

polarization components of Fig. 2, the directly diffracted wave $\mathbf{0}/\mathbf{h}$ allows the coupling *via* the scalar products $\boldsymbol{\pi}_0 \cdot \boldsymbol{\pi}_h$ and $\boldsymbol{\sigma}_0 \cdot \boldsymbol{\sigma}_h$ (where the latter is trivially equal to 1). The components of the *Umweg* wave, which as has been shown depends on the products of the structure factors $F(\mathbf{g})F(\mathbf{h}-\mathbf{g})$, are represented by a twofold scalar product. Each coupling of the polarization components of the $\mathbf{0}$ beam into those of the $\mathbf{h}$ beam *via* the π and σ components of the $\mathbf{g}$ beam with nonzero scalar products have to be taken into account. Thus, there are five coupling channels open. For instance, part of the power of the $\boldsymbol{\pi}_0$ component may be diffracted into the $\boldsymbol{\sigma}_g$ component, which in its turn may be diffracted into the $\boldsymbol{\sigma}_h$ component. It should be noticed that there is no coupling between the $\boldsymbol{\sigma}_0$ and the $\boldsymbol{\pi}_g$ component as they are perpendicular to each other. Therefore, there are three π and two σ channels open for the coupling between the incident beam and the $\mathbf{h}$ reflection *via* the *Umweg* wave.

Dependent on the diffraction geometry, some scalar products may become negative. In terms of three-beam interference, this has to be interpreted as an additional 180° phase shift, which may significantly influence the phase indication of the Ψ-scan profiles as anomalous asymmetry effects occur (Juretschke, 1986; Schwegle, 1989).

Let us discuss this effect under relevant experimental three-beam conditions when linearly polarized synchrotron radiation is used, with its electric field vector either in the plane or perpendicular to the reflection plane $(\mathbf{s}_0, \mathbf{s}_h)$ of the reference two-beam case. In the latter case, the incoming beam is regarded as σ polarized. The input component $D_\pi(\mathbf{0})$ is zero. Nevertheless, there exists a non-zero output $D_\pi(\mathbf{h})$ because of the *Umweg* component $U_{\sigma\pi}$. However, the latter has no relevance for three-beam interference as there exists no D_π component of the primary diffracted wave. Then, there remains the interference between D_σ and $U_{\sigma\sigma}$ where its twofold scalar product $\boldsymbol{\sigma}_0\boldsymbol{\sigma}_g\boldsymbol{\sigma}_g\boldsymbol{\sigma}_h$ is always positive since $\boldsymbol{\sigma}_0$ is parallel to $\boldsymbol{\sigma}_h$. Therefore, in the σ-polarized mode, no anomalous asymmetries occur.

For the in-plane case, the input $D_\sigma(\mathbf{0})$ is null. Then, the interference between D_π and $U^\sigma_{\pi\pi}$ and $U^\pi_{\pi\pi}$ has to be considered. Usually, the Bragg angle θ_h of the primary reflection is smaller than 45°. Then, the scalar product of the primary reflection $\boldsymbol{\pi}_0\boldsymbol{\pi}_h$ is always positive. However, the two $U_{\pi\pi}$ components may become negative. This depends on where the end of $\mathbf{g}$ passes through the Ewald sphere. Such a case is shown in the stereographic projection of Fig. 9. If the end of $\mathbf{g}$ passes through the Ewald sphere in the grey region of the stereographic projection, *i.e.* $\boldsymbol{\pi}_g$ lies between $\boldsymbol{\pi}_0$ and $\boldsymbol{\pi}_h$, then the twofold scalar product $\boldsymbol{\pi}_0\boldsymbol{\pi}_g\boldsymbol{\pi}_g\boldsymbol{\pi}_h$ of the $U^\pi_{\pi\pi}$ component is positive whereas $\boldsymbol{\pi}_0\boldsymbol{\sigma}_g\boldsymbol{\sigma}_g\boldsymbol{\pi}_h$ of $U^\sigma_{\pi\pi}$ is negative. However, the signs of both *Umweg* components are inverted if the end of $\mathbf{g}$ passes through the Ewald sphere in the dark region of Fig. 9.

Generally, for the π-polarized mode, the sign combinations given in Table 1 are possible. If the two *Umweg* components have different signs and if they are

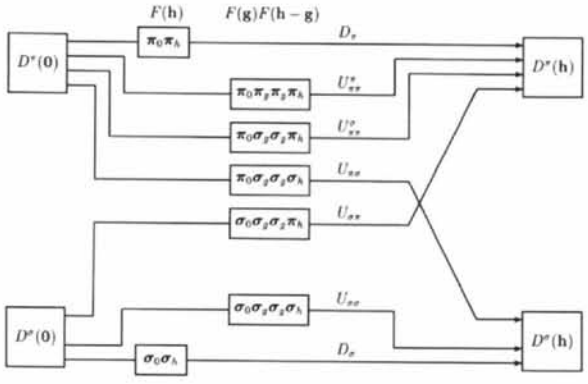

Fig. 8. Schematic flow diagram showing the contributions of different polarization states in the two-beam approximation (Schwegle, 1993).

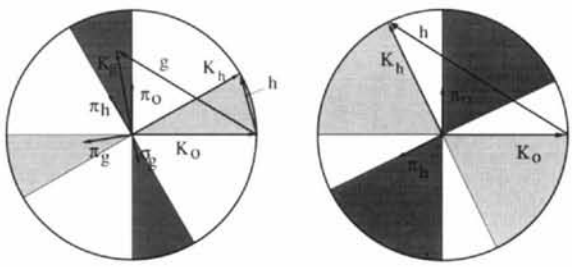

Fig. 9. Stereographic projections of the Ewald sphere onto the primary two-beam diffraction plane. The shadowed regions indicate positions for the end of $\mathbf{g}$ where anomalous asymmetries may occur. Left: $\theta < 45°$, $\boldsymbol{\pi}_0\boldsymbol{\pi}_h > 0$; right: $\theta > 45°$, $\boldsymbol{\pi}_0\boldsymbol{\pi}_h < 0$. The light-grey regions correspond to cases 3 and 5 of Table 1 and the dark-grey regions to cases 2 (as indicated in the left figure) and 6.

comparably strong, then anomalous asymmetries due to the additional geometrically induced phase shift by 180° appear, which may lead to wrong phase indications. Since the diffraction geometry is known, those critical cases can be avoided from the beginning. It should be noticed that in the case of macromolecular structures with large dimensions of the unit cell the Bragg angles are relatively small. Then, the $U^{\sigma}_{\pi\pi}$ component is always weak since $\pi_0\sigma_h$ as well as $\sigma_g\pi_h$ are nearly equal to zero and as a consequence no anomalous asymmetries occur. However, these effects may occur with small-molecule structures. On the other hand, the dependence of the three-beam interference on the polarization can be exploited to detect the polarization state (ellipticity) of the incident beam (Shen & Finkelstein, 1990, 1992; Schwegle, 1993).

4. Computational analysis of three-beam diffraction

4.1. *Dispersion surface*

The dispersion surface is the locus of the tie points where the wave vectors of all the possible waves are attached that may propagate in the crystal with a given frequency. They are calculated from the linear determinantal equation (22), which is a conditional equation for the fundamental equations to provide non-trivial solutions. The tie points that are actually excited are given by the experimental parameters that define the diffraction geometry.

In a three-beam case, the dispersion surface consists of six sheets owing to the π and σ components for each of the **0**, **h** and **g** waves whose wave vectors terminate at the corresponding reciprocal-lattice points 0, H and G. As the three-dimensional dispersion surface for a non-coplanar three-beam case is very difficult to survey, it is appropriate to discuss intersections adapted to the azimuthal Ψ-scan technique where the diffraction condition for the two-beam case **0**/**h**, for instance, is always satisfied. An intersection of the dispersion surface with the plane of incidence for the two-beam case **0**/**h** is shown in Fig. 10(*a*). Near the intersection (Lorentz point Lo_2) of the dispersion spheres around 0 and H, represented by the asymptotes T_0 and T_h, which are the traces of their dispersion spheres, the dispersion surface splits into two hyperbolical branches, one for each π and σ polarization. In the two-beam case, the dispersion surface consists of surfaces of revolution around the diffraction vector **h**. Rocking the crystal about **h** by small angles Ψ makes the actual tie points move approximately perpendicular to the plane of drawing. Therefore, it is convenient to depict the Ψ-scan dispersion surface in an intersection plane perpendicular to the primary diffraction vector **h**. Such an intersection $\overline{AA}$ is shown in Fig. 10(*b*). The three parallel dashed lines are the intersection lines with the diameter points of the two-beam σ hyperbola and the trace of the two-beam Lorentz point Lo_2. The other straight dashed line is the trace T_g of the third dispersion sphere around G. At the three-beam setting ($\Psi = 0$), the three dispersion spheres T_0, T_h and T_g intersect at the three-beam Lorentz point Lo_3. Because of the three-beam interaction, the two-beam dispersion surface splits again at the crossing points with T_g. Hence, T_g is the asymptote of the g-like parts of the dispersion surface away from the three-beam setting where the Poynting vector essentially points to G. The splitting of the dispersion surface owing to the π and σ components is clearly visible.

Fig. 11 shows intersections $\overline{AA}$ of the three-beam dispersion surface for three triplet phases, namely for $\Phi_3 = 0, \pm 90$ and 180°. It can be seen that the dispersion surface near the three-beam Lorentz point Lo_3 is different for different triplet phases. It is asymmetric

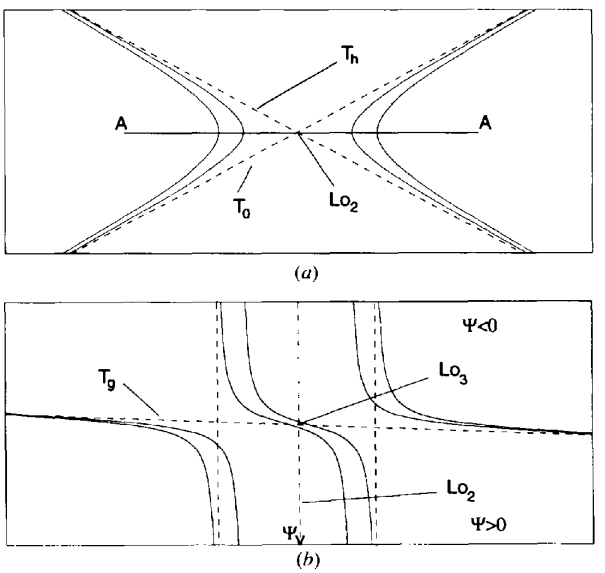

Fig. 10. (*a*) Intersection of the dispersion surface with the diffraction plane in a two-beam case. (*b*) Intersection of the three-beam dispersion surface with the plane A–A of (*a*) for a Ψ scan around **h**.

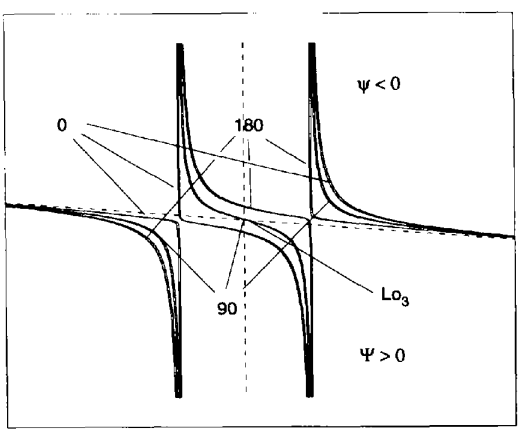

Fig. 11. Same as in Fig. 10(*b*) for different triplet phases of 0, ±90 and 180°.

for Φ_3 equal to 0 and 180° and it is symmetric with respect to Lo_3 for Φ_3 equal to ±90°. This means that the dispersion surface depends on $\cos(\Phi_3)$ since the eigenvalues are identical for Φ_3 equal to +90 and −90°. This behaviour has already been proved by Ewald & Heno (1968). The eigenvectors, however, and thus the three-beam intensity depend also on the sign of Φ_3 where we define its magnitude in the range $0 \leq |\Phi_3| \leq 180°$. This fact has already been discussed by means of the two-beam approximation and it will be discussed later on in more detail.

The asymmetrical dispersion surface leads to asymmetrical Ψ-scan profiles, whereas for $\Phi_3 = \pm 90°$ symmetrical profiles are expected. Thinking in terms of the effective structure factor F_{eff} in the framework of the two-beam approximation, the splitting of the two-beam dispersion surface is supposed to be proportional to F_{eff}. Hence, the intensity is increased if the width of the splitting at the crossing close to Lo_3 is large and *vice versa*. This can be seen in Fig. 11 where for $\Phi_3 = 0°$ the splitting at $\Psi < 0$ is larger than that at $\Psi > 0$. In that case, for an in–out Ψ-scan experiment, the integrated intensity is first increased and then decreased. Consequently, the inverse asymmetry appears for $\Phi_3 = 180°$ and no asymmetry appears for $\Phi_3 = \pm 90°$.

4.2. *Integrated three-beam Ψ-scan profiles*

In the framework of plane-wave dynamical theory, *i.e.* taking ideally monochromatic and ideally non-divergent collimated beams, the N-beam Ψ-scan profiles are calculated from the reflectivity or transmissivity of the primary diffracted ray using (32) as a function of two angular variables Ψ and ω. The ω-rotation axis is perpendicular to the Ψ-rotation axis (*cf.* Figs. 3 and 10). Hence, away from the N-beam setting ($|\Psi| > 0$), an ω scan generates an unperturbed two-beam rocking curve of the primary reflection (*cf.* for instance Fig. 12).

In order to take into account experimental parameters like divergence, spectral bandwidth and mosaicity, the plane-wave dynamical profiles have to be convoluted with a broadening function, for instance with a suitable Gaussian G.

$$I_{\mathbf{h}}^{\text{con}}(\omega, \Psi) = \text{constant} \int_{-\infty}^{+\infty} \mathrm{d}v \int_{-\infty}^{+\infty} \mathrm{d}u \, I_{\mathbf{h}}(\omega - v, \Psi - u) \times G(v, u). \tag{49}$$

It turns out that the divergence together with dispersion effects due to the limited bandwidth usually exceed the ω width of the dynamical profiles. In these cases, the convolution in the ω direction may be replaced by an integration over ω. Then, the integrated Ψ-scan intensity is given by

$$I_{\mathbf{h}}^{\text{int}}(\Psi) = \text{constant} \int_{-\infty}^{+\infty} \mathrm{d}\omega \int_{-\infty}^{+\infty} \mathrm{d}u \, I_{\mathbf{h}}(\omega, \Psi - u) G(u). \tag{50}$$

In the following figures, the integrated intensity $I_{\mathbf{h}}^{\text{int}}(\Psi)$ is normalized with respect to the unperturbed integrated two-beam intensity $I_{\mathbf{h}}^{(2)}$ of the primary reflection.

$$I_{\mathbf{h}}^{\text{rel}}(\Psi) = I_{\mathbf{h}}^{\text{int}}(\Psi)/I_{\mathbf{h}}^{(2)}. \tag{51}$$

Therefore, these diagrams show the relative change of the two-beam intensity owing to simultaneous excitation of other beams.

4.3. *Reflection and transmission geometries*

We are now going to consider different three-beam diffraction geometries. If the crystal is supposed to be a parallel-sided slab, four distinct situations may occur. First of all, the diffraction geometry of the primary reflection has to be considered. It can be a Bragg diffraction case or a Laue transmission case. Since the two-beam intensities in both cases show different behaviour, the question arises whether there are basic differences with respect to the evaluation of triplet phases from three-beam diffraction profiles. In particular

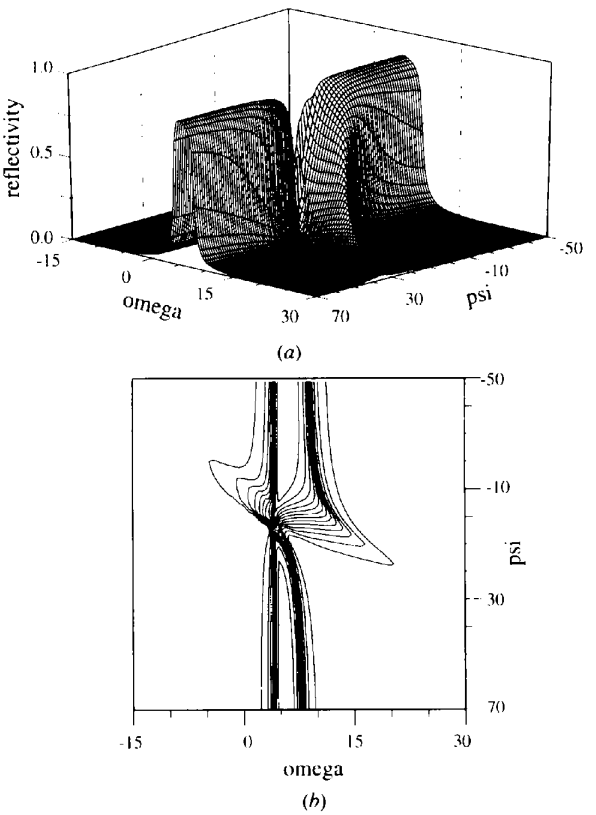

Fig. 12. (*a*) Three-beam reflectivity, $\Phi_3 = 0°$ (axis units in arcseconds), diffraction geometry: Bragg–Bragg; three-beam case: $\mathbf{h} = 311$, $\mathbf{g} = 220$, GaAs; $F(\mathbf{0}) = 242.9$, $|F(\mathbf{h})| = 110.6$, $|F(\mathbf{g})| = 170.2$, $|F(\mathbf{h} - \mathbf{g})| = 143.5$, $\lambda = 1.35$ Å, surface normal: $\mathbf{n} = 311$; plate thickness: 1 mm; incident beam: π polarized. (*b*) Contour plot of (*a*).

in the Laue case, the influence of *Pendellösung* effects has to be considered. In this case, the intensity of the primary reference beam depends critically on the thickness of the crystal and it is expected that additional effects occur.

Moreover, the secondary reflection can be either a Bragg or a Laue case. However, it will turn out that the diffraction geometry of the secondary reflection is not a crucial point. Therefore, the diffraction geometry is denoted by that of the primary reflection, *e.g.* Bragg or Laue case; if necessary, the type of diffraction geometry of the secondary reflection is appended.

An additional parameter in our analysis for different diffraction geometries is the thickness of the crystal. To have a short-hand notation, we speak of a thin or thick crystal if the thickness is smaller or larger than the *Pendellösung* distance, respectively. If necessary, more precise denotations are used.

4.3.1. *Bragg case.* A calculated three-beam diffraction profile $I_{\mathbf{h}}(\omega, \Psi)$ with the primary reflection in Bragg geometry in the case of a thick crystal is shown in Fig. 12(*a*). The triplet phase involved is 0°. Further parameters are given in the caption. Near the three-beam setting, $\Psi \simeq 0$, the two-beam profile is modified owing to the excitation of a secondary reflection. The excitation of **K(h)** waves along the **g**-like part of the dispersion surface can clearly be seen, particularly in the contour plot (Fig. 12*b*). As can further be seen in Fig. 12(*a*), the two-beam profile $I_{\mathbf{h}}(\omega, |\Psi| = \text{constant} > 0)$ far from the three-beam setting shows the typical properties of a Bragg-case rocking curve. The reflectivity is about 90% in the total-reflection domain since absorption is taken into account. Because of refraction at the entry surface, the maximum of the rocking curve is shifted away from the geometrical Bragg angle ($\omega = 0$) calculated from the vacuum wavelength. The relative integrated three-beam reflectivity is shown in Fig. 13. It shows the typical asymmetry of a Ψ-scan profile for $\Phi_3 = 0°$, as already discussed in §3.2. These features are not immediately obvious in Fig. 12 since the increase of the integrated reflectivity is due to a broadening of the two-beam profile near the three-beam setting, where for $\Psi < 0$ the effective structure factor F_{eff} is increased because of the constructive three-beam interference. In the Bragg case for thick crystals, the maximum height of the two-beam rocking curve (*cf.* Fig. 12*a*) is not increased since it is essentially governed by total reflection. The increase of the integrated reflected power due to constructive interference is only possible by broadening the total-reflection range. Contrarily, in the destructive interference range, for $\Psi > 0$, the total reflection width is decreased. These features are immediately obvious in the contour plot of Fig. 12(*b*).

For a thin crystal in Bragg reflection geometry, there exists no total reflection even in the absence of absorption. Fig. 14 shows the three-beam reflectivity of a 180° triplet phase where the thickness of the plate was chosen to achieve a maximum reflectivity of the two-beam case of about 30%. In this case, the reflectivity in the constructive interfering part at $\Psi < 0$ is higher and in the destructive part at $\Psi > 0$ lower compared with the undisturbed two-beam reflectivity. In addition to this change of the maximum reflectivity like in the 'thick'-crystal Bragg case, the width of the reflection profile is increased in the constructive and decreased in the

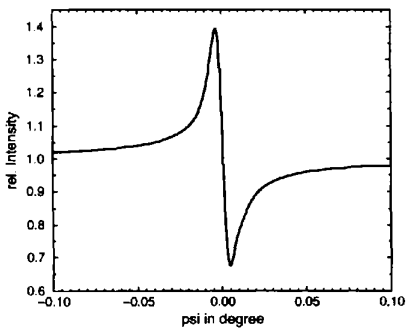

Fig. 13. Integrated three-beam Ψ-scan profile of Fig. 12 convoluted with a Gaussian with $\sigma = 11''$.

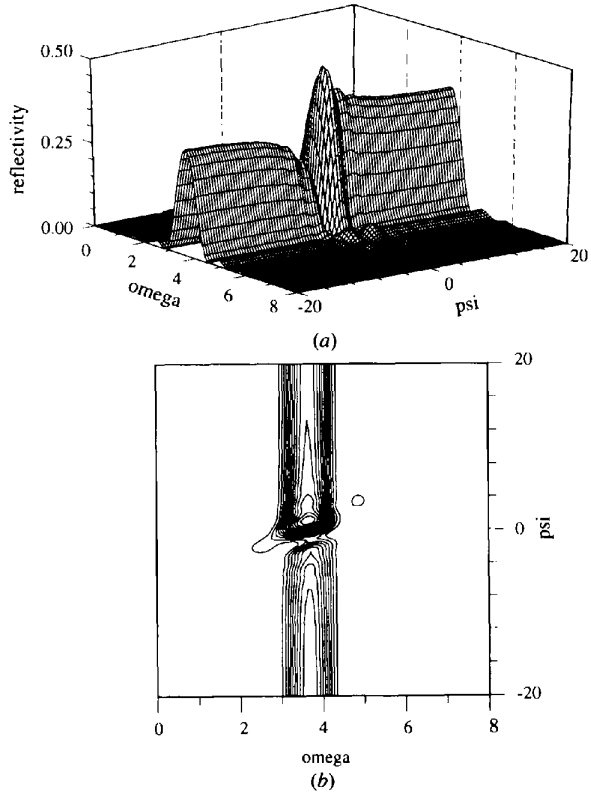

Fig. 14. (*a*) Three-beam reflectivity, $\Phi_3 = 180°$ (axis units in arcseconds), diffraction geometry: Bragg–Bragg; three-beam case: $\mathbf{h} = 040$, $\mathbf{g} = 042$; metric: orthorhombic, $a = 5.582$, $b = 9.812$, $c = 11.796$ Å; $F(\mathbf{0}) = 321$, $|F(\mathbf{h})| = 15.5$, $|F(\mathbf{g})| = 20$, $|F(\mathbf{h} - \mathbf{g})| = 34$; $\lambda = 1.5405$ Å; surface normal: $\mathbf{n} = 040$; plate thickness: 0.02 mm; incident beam: σ polarized. (*b*) Contour plot of (*a*).

destructive region, respectively. In Fig. 15, the integrated three-beam Ψ-scan profile of Fig. 14 is shown. It shows clearly the interference profile of a 180° triplet phase. It should be stressed at this point that an integration in the ω direction is not necessary in the case of a thin crystal as the interference effect is present for each ω close to the maximum of the two-beam rocking curve. This is not the case for a 'thick' crystal with the primary reflection in Bragg geometry.

Figs. 16 and 17 demonstrate that three-beam profiles for Φ_3 equal to +90 and −90° also depend on the sign of the triplet phase. These numerical results clearly confirm the considerations in §3.2. The profiles are symmetrical in both cases. However, the respective relative change of intensity is different owing to constructive and destructive interference effects.

To summarize the results of this section, it should be noticed that if the primary reflection is in Bragg geometry then there is no distinct difference between the thick- and thin-crystal cases with respect to the integrated three-beam intensity, which is usually observed in a real experiment. The important differences for Φ_3 equal to +90 or −90° can be used for the experimental determination of the absolute structure (*cf.* §6.1).

4.3.2. *Laue case.* The essential difference compared with the Bragg case is that *Pendellösung* effects occur in the Laue case for thick crystals which seriously affect phase determination by N-beam diffraction. It is well known from the two-beam case that these effects are due to the interference of the waves that belong to tie points at different branches of the dispersion hyperbola. The diffracted power at the exit surface oscillates between the two transmitted waves $T(\mathbf{0})$ and $T(\mathbf{h})$ (*cf.* Fig. 1) depending on the crystal thickness. This occurs as the phase difference between the **0** waves of different tie points on the one hand and that of the **h** waves of different tie points on the other hand changes continuously with the penetration depth t. The interference term that causes the *Pendellösung* oscillations is given by $2D_1D_2\cos[2\pi\Lambda^{-1}t]$, where the D's are the amplitudes of the waves from different branches of the dispersion hyperbola and Λ is the *Pendellösung* distance (Authier, 1993). In the three-beam Laue–Laue case, *i.e.* the primary **h** reflection as well as the secondary **g** reflection are in transmission geometry, the transmitted power oscillates between three transmitted rays. In a Laue–Bragg case, the situation is comparable to that of a two-beam Laue case. In any case, there are additional phase effects that, so far, have not been taken into account (*cf.* §3.2), which, however, may drastically influence the phase indication of the three-beam profiles. Therefore, we focus at first on the thin-crystal case where the thickness is well below the

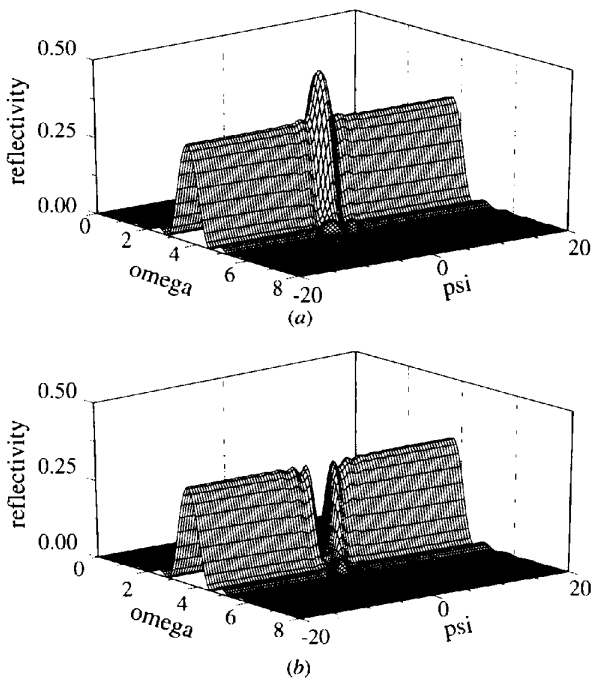

Fig. 16. Three-beam reflectivity. (*a*) $\Phi_3 = -90°$, (*b*) $\Phi_3 = 90°$ (axis units in arcseconds), diffraction geometry: Bragg–Bragg; three-beam case: **h** = 040, **g** = 042; metric: orthorhombic, a = 5.582, b = 9.812, c = 11.796 Å; $F(\mathbf{0}) = 321$, $|F(\mathbf{h})| = 15$, $|F(\mathbf{g})| = 20$, $|F(\mathbf{h}-\mathbf{g})| = 25$, λ = 1.5405 Å; surface normal: **n** = 040; plate thickness: 0.02 mm; incident beam: σ polarized.

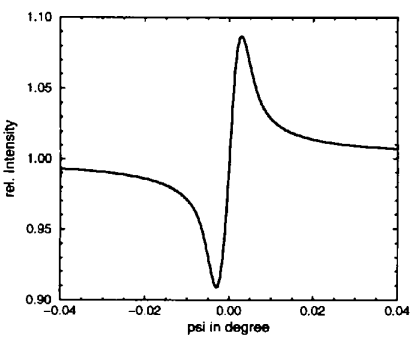

Fig. 15. Integrated three-beam Ψ-scan profile of Fig. 14, convoluted with a Gaussian with $\sigma = 11''$.

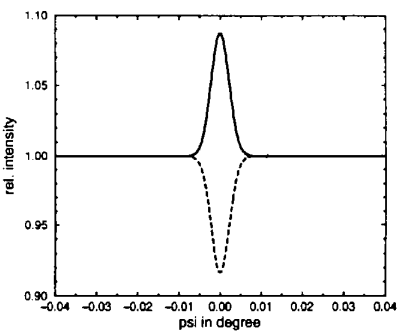

Fig. 17. Integrated Ψ-scan profiles for triplet phases −90° (solid) and +90° (dashed) of Fig. 16 convoluted with a Gaussian with $\sigma = 11''$.

first *Pendellösung* period of the primary **h** reflection, *i.e.* Λ^{-1} is given by the distance of the diameter points of the two-beam hyperbola. Afterwards, the thick-crystal case will be discussed.

Fig. 18 shows the calculated three-beam transmissivity of a Laue case for $\Phi_3 = 180°$. The constructive interference effect in the range $\Psi > 0$ as well as the destructive interference for $\Psi < 0$ close to three-beam setting is clearly be seen. Figs. 19 and 20, for Φ_3 equal to +90 and −90°, demonstrate that also in the Laue case the three-beam intensity depends on the sign of the triplet phase. For +90°, the maximum height of the three-beam intensity is decreased; it is increased for −90°. A comparison of Figs. 19 and 16 reveals similar features of the corresponding profiles in Bragg and Laue geometry. The oscillations obvious in Figs. 19 and 16 are due to the small thickness chosen for the calculations. They correspond to *Pendellösung* fringes of constant inclination.

A summary outline of integrated three-beam Ψ-scan profiles for different triplet phases that are relevant in a real experiment is given in Fig. 6. The respective profiles of triplet phases with opposite sign are compared. This comparison is also of experimental relevance since, as will be understood later (*cf.* §4.4), we always measure the pair of three-beam cases **0/h/g** and **0/−h/−g**. They have opposite signs of triplet phase, although the magnitudes of the involved structure factors are the same if anomalous scattering can be neglected.

In the thin-crystal case, the three-beam profiles show no essential difference between the Laue and Bragg geometry (*cf.* Figs. 16, 19). However, for thick crystals in the Laue case, *Pendellösung* effects come into play. This can be seen in Fig. 21, where the interference effects for Φ_3 equal to +90 and −90° are inverted owing to the *Pendellösung* interference at this thickness.

The integrated three-beam transmissivity at the three-beam position $\Psi = 0$ for triplet phases $\Phi_3 = \pm 90°$

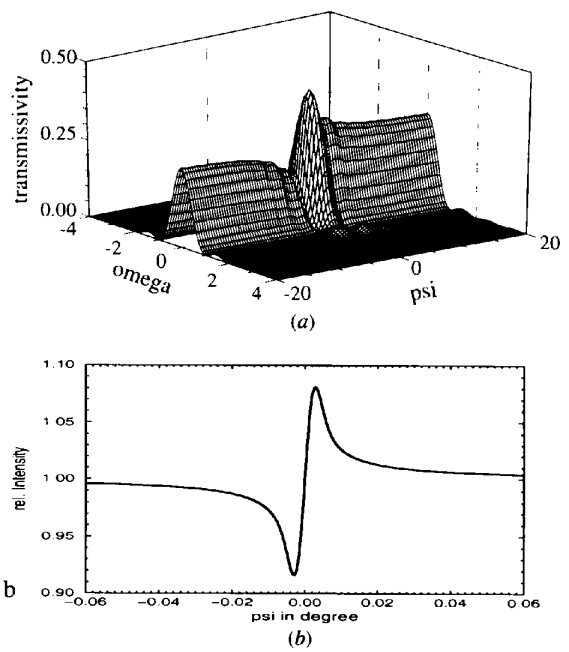

Fig. 18. (*a*) Three-beam transmissivity, $\Phi_3 = 180°$ (axis units in arcseconds). Diffraction geometry: Laue–Laue; three-beam case: **h** = 040, **g** = 042; metric: orthorhombic, $a = 5.582$, $b = 9.812$, $c = 11.796$ Å; $F(\mathbf{0}) = 321$, $|F(\mathbf{h})| = 15.5$, $|F(\mathbf{g})| = 20$, $|F(\mathbf{h}-\mathbf{g})| = 30$, $\lambda = 1.5405$ Å, plate thickness: 0.05 mm, incident beam: σ polarized. (*b*) Integrated Ψ-scan profile of (*a*) convoluted with a Gaussian with $\sigma = 11''$.

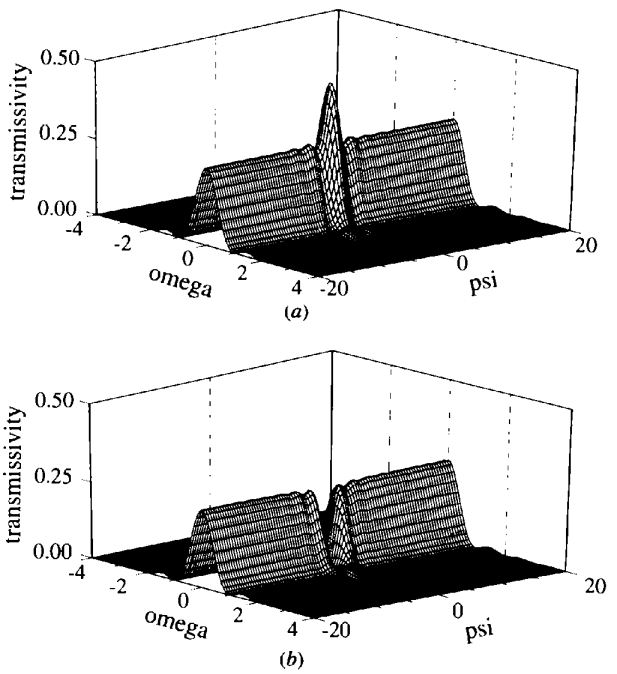

Fig. 19. Three-beam transmissivity. (*a*) $\Phi_3 = -90°$, (*b*) $\Phi_3 = 90°$ (axis units in arcseconds), diffraction geometry: Laue–Laue; three-beam case: **h** = 040, **g** = 042; metric: orthorhombic, $a = 5.582$, $b = 9.812$, $c = 11.796$ Å; $F(\mathbf{0}) = 321$, $|F(\mathbf{h})| = 15$, $|F(\mathbf{g})| = 20$, $|F(\mathbf{h}-\mathbf{g})| = 35$; $\lambda = 1.5405$ Å; plate thickness: 0.05 mm; incident beam: σ polarized.

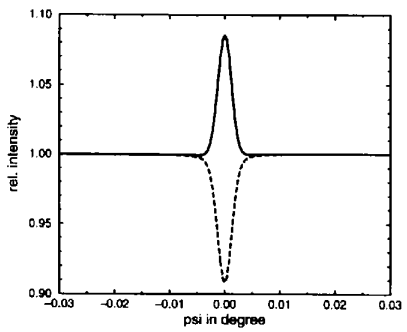

Fig. 20. Integrated three-beam Ψ-scan profiles of Fig. 19 convoluted with a Gaussian with $\sigma = 11''$ (solid: $\Phi_3 = -90°$; dashed: $\Phi_3 = 90°$).

as a function of the crystal thickness compared with the *Pendellösung* period of the integrated two-beam intensity is shown in Fig. 22. It can be seen that, if the thickness is below the first maximum of the three-beam *Pendellösung* period of the profile that corresponds to $\Phi_3 = -90°$, the expected three-beam profiles were observed, *i.e.* the three-beam interference is not disturbed by *Pendellösung* interferences (*cf.* Figs. 19 and 20). However, if the thickness of the crystal plate is comparable with the first maximum of the *Pendellösung* of the three-beam case, unambiguous interpretation with respect to the sign of the triplet phase is not possible. It should be noticed that the Ψ-scan profiles for $\Phi_3 = \pm 90°$ remain symmetrical independent of the thickness, *i.e.* independent of the *Pendellösung* interferences, owing to the centrosymmetry of the dispersion surface. Therefore, it is always possible to determine the modulus of the triplet phase. The determination of its sign, however, is questionable in the Laue case for thick crystals (*cf.* Fig. 21). It should further be pointed out that, if the *Pendellösung* interferences are not taken into account, that means summing up the intensities of the waves of different tie points rather than the amplitudes according to (30) and (31), then the information on the sign of the triplet phase gets lost, since the eigenvectors for different signs of Ψ_3 are complex conjugated (Chang, 1987).

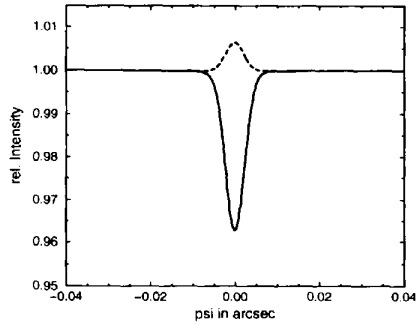

Fig. 21. Integrated three-beam Ψ-scan profiles of Fig. 19 convoluted with a Gaussian with $\sigma = 11''$ (solid: $\Phi_3 = -90°$; dashed: $\Phi_3 = 90°$) calculated for a thickness of 0.175 mm.

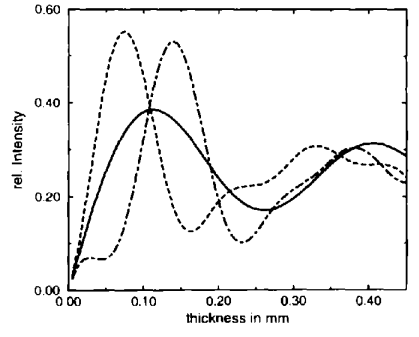

Fig. 22. Integrated intensity of the primary reflection $\mathbf{h} = 040$ as a function of thickness (*Pendellösung*) with the parameters used for Fig. 19 [*cf.* (50)]; solid: two-beam case; dashed: three-beam case with $\Phi_3 = -90°$ at $\Psi = 0$; dot-dashed: three-beam case with $\Phi_3 = 90°$ at $\Psi = 0$.

4.4. *Phase-independent Umweganregung and Aufhellung effects*

In the calculation of the integrated three-beam Ψ-scan profiles of Fig. 6, the magnitudes of the involved structure factors are chosen so that the constructive and destructive interference effects are approximately of equal size comparing the profiles of triplet phases with opposite signs. Ideally, as can be understood by means of the two-beam approximation (*cf.* §3.2) and as can be seen in Fig. 6, the relative intensity change $I_{\mathbf{h}}^{\mathrm{rel}}(\Psi)_+$ for a triplet phase with positive sign taken at a certain azimuth angle Ψ is inverted with respect to that taken at the corresponding negative angle $-\Psi$ of the profile for the negative triplet phase $I_{\mathbf{h}}^{\mathrm{rel}}(-\Psi)_-$. This means, if we sum up,

$$\Delta I(\Psi) = \tfrac{1}{2}[I_{\mathbf{h}}^{\mathrm{rel}}(\Psi)_+ + I_{\mathbf{h}}^{\mathrm{rel}}(-\Psi)_-], \qquad (52)$$

and if we assume that the intensity modulation is completely governed by three-beam interference according to (37), then $\Delta I(\Psi)$ should remain constant and equal to one. This condition is approximately satisfied by the profiles of Fig. 6.

However, it turns out that in the case of N-beam diffraction there are also phase-independent contributions that lead to a modification of the two-beam intensity of each Bragg reflection involved. Such effects have been well known for a long time. Enhancement of the two-beam Bragg intensity was called *Umweganregung* (Renninger, 1937). Attenuation was called *Aufhellung* as, for instance, a divergent-beam photograph of a diffraction cone of a strong reflection is less darkened at the position at which multiple diffraction occurs. These effects are due to the dynamical self-consistent balance of the energy flow. For example, if in a three-beam case the structure factor of the primary **h** reflection is much weaker than those of the secondary **g** and of the coupling $\mathbf{h} - \mathbf{g}$ reflection then part of the intensity of the **g** reflection is coupled into the **h** reflection *via* $\mathbf{h} - \mathbf{g}$. As a result, enhancement of the two-beam intensity is observed, as that was the case in the Renninger experiment, independently of the phase relationships. In contrast to this situation, if the intensity of the primary **h** reflection is much stronger than that of the secondary **g** reflection, then a considerable amount of the intensity of the first is diffracted into the second *via* $-(\mathbf{h} - \mathbf{g})$. This loss of intensity is not compensated by the diffraction power of the **g** reflection into the **h** reflection. Consequently, the intensity of the primary reflection is attenuated. The mean energy flow due to this mutual coupling is described by the so-called energy-transfer equations (Zachariasen, 1967; Moon & Shull, 1964), which is a system of coupled equations that must satisfy the condition of conservation of energy.

The interaction terms are taken to be proportional to the respective intensities of the individual reflections. Thus, the interaction is assumed to be phase independent. If in a three-beam case this mutual coupling of the intensities is well balanced, then no changes of the two-beam intensity would result, except for those due to interference effects that modulate the mean energy flow. This situation would lead to so-called *ideal* three-beam Ψ-scan profiles where $\Delta I(\Psi) = 1$.

In Fig. 23, typical *Umweganreganregung* profiles are shown and, in Fig. 24, typical *Aufhellung* profiles for different triplet phases. In each case, the $\Delta I(\Psi)$ curve is plotted. According to definition (52), the difference between a Ψ-scan profile with *Umweganregung* or *Aufhellung* and the corresponding $\Delta I(\Psi)$ curve gives the ideal profile. Thus, in general, each Ψ-scan profile can be separated into two parts: (1) the symmetrical $\Delta I(\Psi)$ curve that represents the phase-independent part owing to *Umweganregung* and *Aufhellung* and (2) the ideal profile that bears the information on the triplet phase.

This is the reason we always measure the pair of centrosymmetrically related three-beam cases $\mathbf{0/h/g}$ and $\mathbf{0/-h/-g}$. They differ in the sign of their triplet phase, however, the magnitudes of the involved structure factors are the same. Therefore, *Umweganregung* or *Aufhellung* have the same magnitude in both cases. Calculation of the $\Delta I(\Psi)$ curve means that the phase-independent effects can be separated.

In a paper by Chang & Tang (1988), *Umweganregung* is denoted as 'kinematical diffraction intensity I_K'. These authors propose to separate the phase-independent part for the quantitative determination of the triplet phase from a single Ψ-scan profile by calculating the I_K curve, which is a Lorentzian around the three-beam point $\Psi = 0$ whose parameters are determined by the diffraction geometry, the magnitudes of the involved structure factors, the intrinsic peak width of diffraction, the divergence of the incident beam and the crystal mosaic spread. The relative complicated expression for I_K is obtained by resolving the dynamical three-beam equations by first-

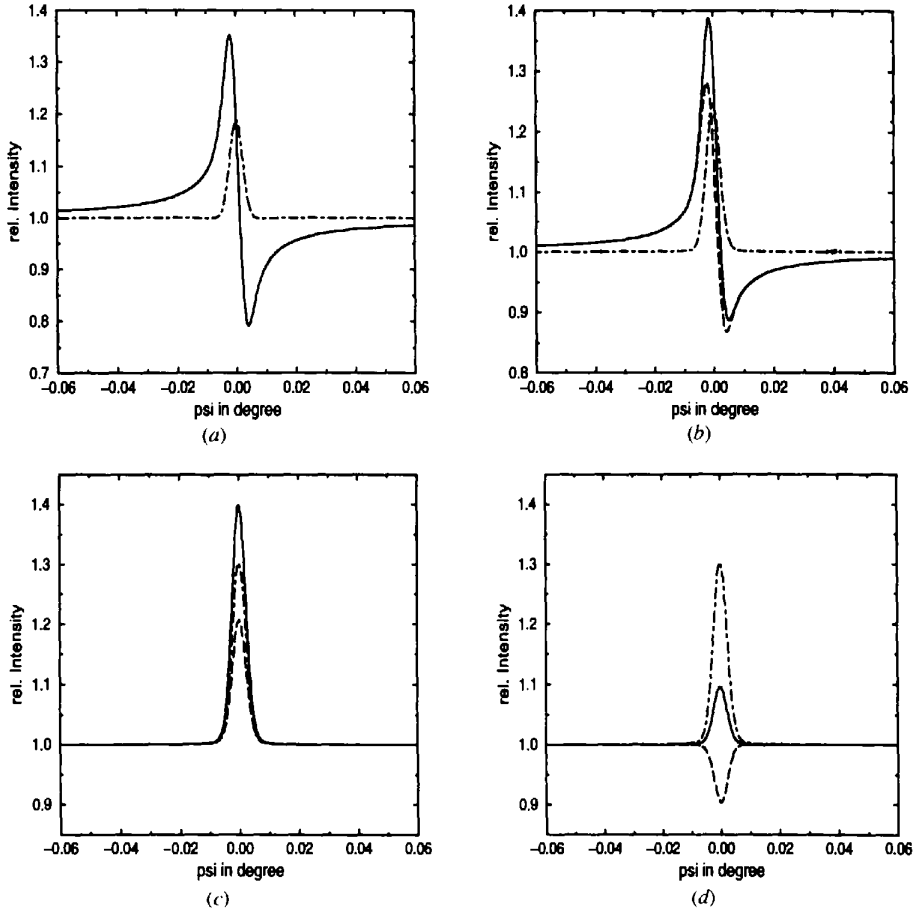

Fig. 23. Integrated three-beam Ψ-scan profiles with *Umweganregung*: (*a*) $\Phi_3 = 0°$, (*b*) $\Phi_3 = \pm 45°$, (*c*) $\Phi_3 = \pm 90°$, (*d*) profiles of (*c*) corrected for $\Delta I(\Psi)$; solid: negative Φ_3; dashed: positive Φ_3; dot-dashed: $\Delta I(\Psi)$ curve. Diffraction geometry: Bragg–Bragg; three-beam case: $\mathbf{h} = 040$, $\mathbf{g} = 042$; metric: orthorhombic, $a = 5.582$, $b = 9.812$, $c = 11.796$ Å; $F(\mathbf{0}) = 321$, $|F(\mathbf{h})| = 10$, $|F(\mathbf{g})| = 40$, $|F(\mathbf{h} - \mathbf{g})| = 40$, $\lambda = 1.5405$ Å, surface normal: $\mathbf{n} = 040$; plate thickness: 0.05 mm; incident beam: σ polarized.

order two-beam approximation. The crucial point of this method is the determination of the three-beam point $\Psi = 0$ that must be fixed with an accuracy of some arcseconds.

In Figs. 23 and 24, it can be seen that the interference effects of the $+90$ and $-90°$ profiles are overcompensated by *Umweganregung* and *Aufhellung*. Nevertheless, it is possible to exploit the triplet phase unambiguously. In Fig. 23, for instance, *Umweganregung* amounts to 30% and the modulation due to three-beam interference is $\pm 10\%$ for $\Phi_3 = \mp 90°$, respectively.

If the phase-independent effects are strong compared with the interference effects then the evaluation of the phase relationships gets more and more difficult. This happens particularly if the primary reflection is weak. Then the phase information, if there is any, is contained in the asymmetry of the wings of an *Umweganregung* peak (*cf.* Shen & Colella, 1988; Tang & Chang, 1988).

It should be pointed out that these phase-independent effects are inherently contained in the solutions of the dynamical N-beam theory. Obviously, they depend on the ratio of the magnitudes of the structure factors $|F(\mathbf{h})|$ and $|F(\mathbf{g})F(\mathbf{h}-\mathbf{g})|$, which determine the amplitudes of the primary reflection and the *Umweg* wave, respectively. As to theoretical results and our experimental experience, the ratio

$$Q = |F'(\mathbf{g})F'(\mathbf{h}-\mathbf{g})|/|F'(\mathbf{h})|^2 \qquad (53)$$

should cover the range $2 < Q < 6$ in order to keep *Umweganregung* and *Aufhellung* small provided that $|F'(\mathbf{g})|$ and $|F'(\mathbf{h}-\mathbf{g})|$ are also of the same order of magnitude. The F' are the structure factors corrected for the geometrical polarization factors. It has turned out that this rule of thumb is not independent of the absolute magnitudes of the structure factors compared with $F(\mathbf{0})$. This fact is illustrated in Fig. 25 where the magnitude of the phase-independent effects and the interference effects for Laue diffraction geometry as a function of Q are compared. In the case of very weak reflections,

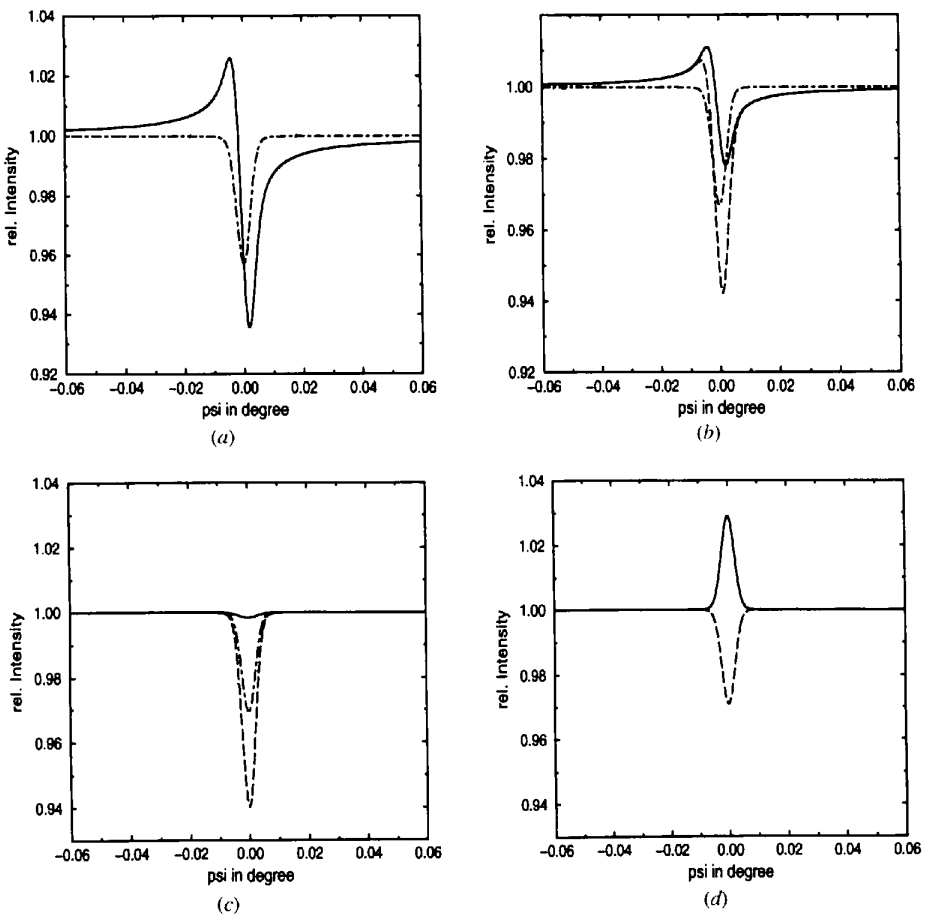

Fig. 24. Integrated three-beam Ψ-scan profiles with *Aufhellung*: (*a*) $\Phi_3 = 0°$, (*b*) $\Phi_3 = \pm 45°$, (*c*) $\Phi_3 = \pm 90°$, (*d*) profiles of (*c*) corrected for $\Delta I(\Psi)$; solid: negative Φ_3; dashed: positive Φ_3; dot-dashed: $\Delta I(\Psi)$ curve. Diffraction geometry: Bragg–Bragg; three-beam case: $\mathbf{h} =$ 040, $\mathbf{g} = 042$; metric: orthorhombic, $a = 5.582$, $b = 9.812$, $c = 11.796$ Å; $F(\mathbf{0}) = 321$, $|F(\mathbf{h})| = 20$, $|F(\mathbf{h}-\mathbf{g})| = 18$, $|F(\mathbf{g})| = 18$, $\lambda =$ 1.5405Å; surface normal: $\mathbf{n} = 040$; plate thickness: 0.05 mm; incident beam: σ polarized.

for example $|F(\mathbf{h})/F(\mathbf{0})| = 0.0036$, the magnitude of the interference effect (label 1) stays well above the phase-independent *Umweganregung* effect (label 1′) even for high values of Q. On the contrary, for strong reflections, for example $|F(\mathbf{h})/F(\mathbf{0})| = 0.0162$ (labels 3 and 3′), *Umweganregung* exceeds the interference effects for Q larger than seven. As a result, the empirical rule for Q works quite well for medium and strong primary reflections. For very weak reflections, there seems to be no restriction. *Aufhellung* effects, which means ΔI from (52) is smaller than one, seem to be negligible in Laue diffraction geometry.

In the Bragg geometry, however, *Aufhellung* is the predominant phase-independent effect especially for low values of Q. This is shown in Fig. 26. For small ratios of $|F(\mathbf{h})/F(\mathbf{0})|$, *Umweganregung* and *Aufhellung* effects (labels 1′, 2′) are again negligible or at least significantly smaller than the interference effects (labels 1, 2). Whereas, in the case of larger $|F(\mathbf{h})/F(\mathbf{0})|$ (label 3) for small Q, *Aufhellung* is nearly as strong as the interference effect, which is, however, dominating for Q larger than two.

In the discussion above, the calculations were carried out with $|F(\mathbf{g})| = |F(\mathbf{h} - \mathbf{g})|$. This symmetry between $\mathbf{g}$ and $\mathbf{h} - \mathbf{g}$ is of course a simplification compared with real three-beam cases. The special situation where one of $|F(\mathbf{g})|$ or $|F(\mathbf{h} - \mathbf{g})|$ is very small or close to zero has not been considered so far and will be discussed now for its practical relevance in order to estimate the effect of neighbouring weak three-beam cases on an interesting one. For $|F(\mathbf{h} - \mathbf{g})|$ very small or zero, the incoming intensity will be shared between reflections $\mathbf{h}$ and $\mathbf{g}$ with small or no coupling between both, which will cause *Aufhellung*. No phase information can be extracted from three-beam cases like this. The situation is symmetric between $|F(\mathbf{g})|$ and $|F(\mathbf{h} - \mathbf{g})|$, this means that an $|F(\mathbf{g})|$ close to zero will also lead to *Aufhellung* as intensity is removed from reflection $\mathbf{h}$ by the coupling vector $\mathbf{h} - \mathbf{g}$ into the direction $\mathbf{K}(\mathbf{g})$. In Fig. 27, an example of the relative *Aufhellung* as function of $|F(\mathbf{h} - \mathbf{g})|/|F(\mathbf{h})|$ is drawn for different values of $|F(\mathbf{h})|/F(\mathbf{0})$. For these calculations, $|F(\mathbf{g})|$ is set to zero. The curve for the largest value of $|F(\mathbf{h})|/F(\mathbf{0})$ represents the situation that is encountered in the case of a small-molecule compound and the smaller values are closer to the situation for a protein crystal. It is obvious that in the latter case the *Aufhellung* of a reflection with a certain $|F(\mathbf{h})|$ is less pronounced owing to the excitation of a second reflection with a comparable structure-factor modulus than for a

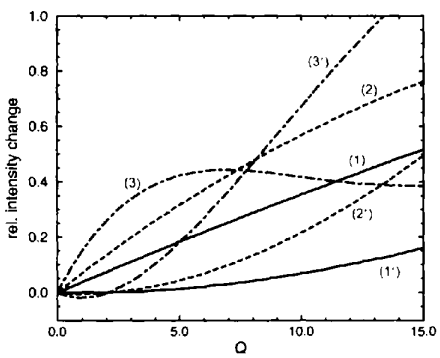

Fig. 25. Magnitude of interference (labelled without primes) and phase-independent effects (with primes) due to (52) as a function of Q (53) for different ratios of $|F(\mathbf{h})/F(\mathbf{0})|$. $|F(\mathbf{h})/F(\mathbf{0})| = 0.0036$ (solid line, 1, 1′), $|F(\mathbf{h})/F(\mathbf{0})| = 0.0067$ (dashed line, 2, 2′), $|F(\mathbf{h})/F(\mathbf{0})| = 0.0162$ (dot-dashed line, 3, 3′). Geometrical parameters and structure-factor phases were taken from the three-beam case shown in Fig. 38; diffraction geometry: Laue–Laue; plate thickness: 0.3 mm; incident beam: π polarized.

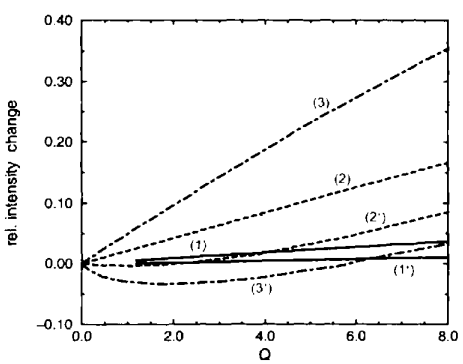

Fig. 26. Magnitude of interference (labelled without primes) and phase-independent effects (with primes) due to (52) as a function of Q (53) for different ratios of $|F(\mathbf{h})/F(\mathbf{0})|$. $|F(\mathbf{h})/F(\mathbf{0})| = 0.0031$ (solid line, 1, 1′), $|F(\mathbf{h})/F(\mathbf{0})| = 0.016$ (dashed line, 2, 2′), $|F(\mathbf{h})/F(\mathbf{0})| = 0.053$ (dot-dashed line, 3, 3′). Geometrical parameters and structure-factor phases were taken from the three-beam cases shown in Fig. 23; diffraction geometry: Bragg–Bragg; plate thickness: 0.05 mm; $\lambda = 1.3$ Å; incident beam: π polarized.

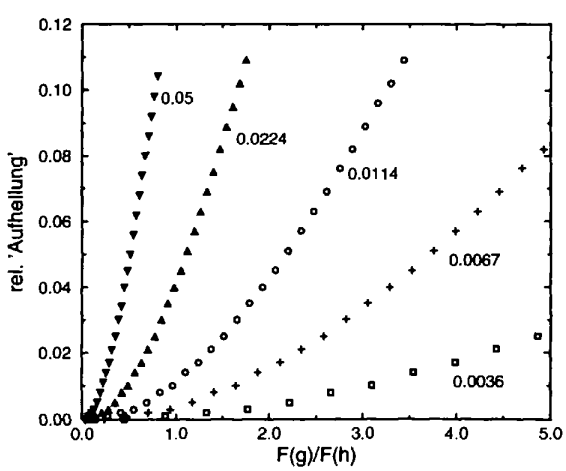

Fig. 27. Relative *Aufhellung* for different ratios of $|F(\mathbf{h})/F(\mathbf{0})|$ as a function of $|F(\mathbf{h} - \mathbf{g})|/F(\mathbf{h})$ with $|F(\mathbf{g})| = 0$ [which is equivalent to $|F(\mathbf{g})|/F(\mathbf{h})$ with $|F(\mathbf{h} - \mathbf{g})| = 0$]; the values of $|F(\mathbf{h})|/F(\mathbf{0})$ are indicated. All geometrical parameters were taken from the three-beam case shown in Fig. 38; diffraction geometry: Laue–Laue; plate thickness: 0.3 mm; incident beam: π polarized.

small-molecule compound. As a rule, *Aufhellung* is less striking if diffraction power is weak. In fact, this is important for the phase determination of macromolecular structures (*cf.* §6.3).

4.5. *Anomalous asymmetries*

In §3.3, the effect of the change of sign of the coupling scalar products in (12) and (13) on the interference profiles has already been discussed. A numerical example demonstrating this effect is given in Fig. 28 (Schwegle, 1989). For the diffraction geometry of the three-beam case of Fig. 28(*a*), only the '*Umweg*' $U^{\sigma}_{\pi\pi}$ channel is active for a π-polarized incident beam whereas $U^{\pi}_{\pi\pi}$ is negligible as $\boldsymbol{\pi}_g\boldsymbol{\pi}_h \simeq 0$. However, since $\boldsymbol{\pi}_0\boldsymbol{\pi}_g \neq 0$, the $\boldsymbol{\pi}$ component of the incoming beam is shared between the primary and secondary reflections, which obviously leads to *Aufhellung* effects. As $\boldsymbol{\pi}_0\boldsymbol{\sigma}_g\boldsymbol{\sigma}_g\boldsymbol{\pi}_h$ is positive, *i.e.* no geometrical phase shifts are induced, a typical 0° three-beam profile with *Aufhellung* results. In Fig. 28(*b*), the situation is reversed. The amplitude of $U^{\sigma}_{\pi\pi}$ is now weaker than the amplitude of $U^{\pi}_{\pi\pi}$. Since $\boldsymbol{\pi}_0\boldsymbol{\pi}_g\boldsymbol{\pi}_g\boldsymbol{\pi}_h$ is negative, we end up with an additional phase shift of 180°, which reverses the asymmetry of the interference profile. This corresponds to the second case in Table 1.

5. Experimental determination of three-phase invariants

5.1. *Experimental set-up and procedure*

5.1.1. *General requirements.* As has been shown in §4, the intrinsic dynamical width of the three-beam interference profiles is of the order of some arcseconds. It depends essentially on the relative magnitude of the structure factors, on the modulus of the triplet phase and on the diffraction geometry. The experimentally observed width is given by the convolution of the dynamical profiles with a broadening function, which depends on the angular divergence and the spectral bandwidth of the incident beam as well as the mosaic spread of the investigated sample. These instrument and sample smearing effects also reduce the interference contrast. Consequently, the use of a well collimated incident beam and crystals with high perfection is advantageous.

Another point to be regarded concerns the density of three-beam positions as the crystal is rotated about the scattering vector of the primary reflection. A rough estimation for a small-molecule structure where the unit-cell volume is about 600 Å^3 shows that for a reasonable length of $|\mathbf{h}| = 0.3$ Å^{-1} using Cu $K\alpha$ radiation the mean angular distance between two three-beam positions is approximately 0.05° on the Ψ scale. As these are not equidistant, it is therefore possible for structures of that size to find for a selected three-beam case gaps in the sequence of three-beam positions by tuning the wavelength so that the angular distance to its neighbours is larger than 0.1°. Then, overlap of adjacent profiles can be avoided. This is shown in Fig. 29 for a small-molecule compound and in Fig. 30 for a small protein where only three-beam cases with $q = |F(\mathbf{g}')F(\mathbf{h}-\mathbf{g}')|/|F(\mathbf{g})F(\mathbf{h}-\mathbf{g})| > 0.25$ that will give significant effects are plotted. $\mathbf{h}/\mathbf{g}'/\mathbf{h}-\mathbf{g}'$ denote neigbouring three-beam cases. Thus, tunability of wavelength is another requirement for triplet phase data collection with regard to the solution of unknown structures that needs a large number of triplet phases. The problem of inevitable overlaps for macromolecular structures will be discussed in §6.3.

5.1.2. *X-ray sources.* The preceding considerations show that high-brilliance sources should be used. Therefore, for home laboratory experiments, a high-brilliance rotating-anode source is advantageous. A rough estimate for crystals with dimensions of 0.3 mm using the bathed crystal technique, an effective source size of 0.3 ×

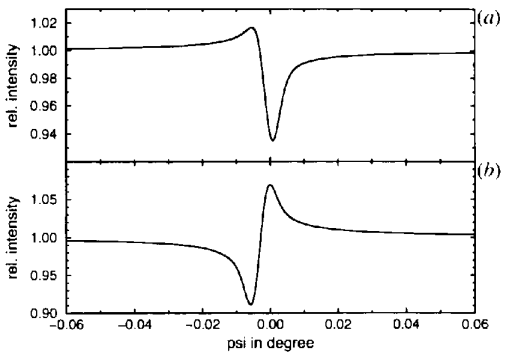

Fig. 28. Integrated three-beam Ψ-scan profiles, $\Phi_3 = 0°$; (*a*) $\lambda = 1.95$ Å typical 0° Ψ-scan profile with *Aufhellung*, $\boldsymbol{\pi}_0\boldsymbol{\pi}_g\boldsymbol{\pi}_g\boldsymbol{\pi}_h = -0.0004$, $\boldsymbol{\pi}_0\boldsymbol{\sigma}_g\boldsymbol{\sigma}_g\boldsymbol{\pi}_h = 0.29$; (*b*) $\lambda = 2.53$ Å anomalous asymmetry owing to an additional geometrically induced phase shift of 180°, $\boldsymbol{\pi}_0\boldsymbol{\pi}_g\boldsymbol{\pi}_g\boldsymbol{\pi}_h = -0.204$, $\boldsymbol{\pi}_0\boldsymbol{\sigma}_g\boldsymbol{\sigma}_g\boldsymbol{\pi}_h = 0.08$. Three-beam case: $\mathbf{h} = 12\bar{3}$, $\mathbf{g} = 321$; diffraction geometry: Bragg–Laue; metric: orthorhombic, $a = 7.075$, $b = 10.277$, $c = 8.775$ Å; $F(\mathbf{0}) = 312$, $|F(\mathbf{h})| = 20$, $|F(\mathbf{g})| = 40$, $|F(\mathbf{h}-\mathbf{g})| = 30$; plate thickness: 0.05 mm; incident beam: π polarized.

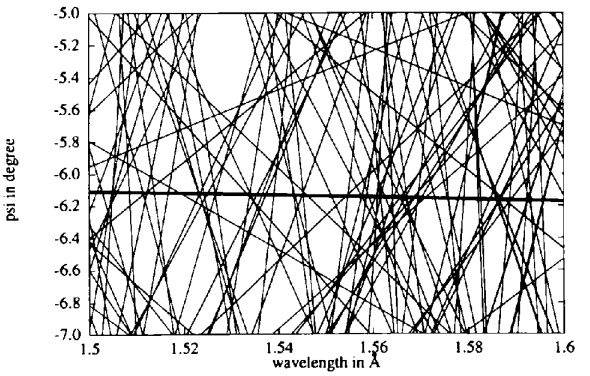

Fig. 29. Three-beam position dependence on Ψ and λ for L-asparagine monohydrate with $V_c = 646$ Å^3. Each line represents the position of a three-beam case for the primary reflection 200. The thick line shows the position of the three-beam case $200/10\bar{2}/1\bar{0}2$. There is a gap for $\lambda = 1.54$ Å of about ±0.2°, for instance.

0.3 mm and a source-to-crystal distance of 1 m gives a divergence of 0.42 mrad ($\sim 0.024°$).

The major advantages using synchrotron radiation (SR) are, firstly, the possibility of tuning the wavelength and, secondly, three or more orders-of-magnitude higher brilliance comparing the characteristic line of a 6 kW mm^{-2} rotating anode with SR from a bending magnet at the ESRF. Experiments were carried out with synchrotron radiation either from a bending magnet (BM) of DORIS (HASYLAB, Hamburg, Germany) or from a bending magnet of the ESRF (Swiss–Norwegian Beamline, Grenoble, France). Very commonly, a fixed-exit double-crystal Si 111 monochromator operating in vertical mode giving a bandwidth of approximately 0.01 to 0.03% is used. The selected wavelengths for our experiments cover the range from 0.5 to 2.5 Å. The divergence is given by the size of source and crystal and the distance between them. With the crystal size assumed to be 0.3 mm, the divergence at DORIS was about 0.002° in the vertical and 0.006° in the horizontal direction and at the ESRF about 0.0007° in both directions.

It should be noticed that the bandwidth is not the crucial point. In principle, white radiation can be used, since multiple-beam interference is restricted to the wavelength band that is accepted by the primary reflection (*cf.* §2.1).

The experimental beam conditions will be given in the caption of each experimental profile shown, where σ polarization denotes scattering perpendicular to and π polarization in the plane of the synchrotron, respectively.

An indispensable demand on the quality of SR is beam-position stability. For good-quality lysozyme crystals, for example, the typical FWHM of reflections is 0.005° (*cf.* Fig. 31). This means that short-term beam instabilities of the order of seconds lead to serious noise in the reference two-beam intensity. Long-term instabilities can be averaged out, since in our measuring routines each Ψ-scan profile is the sum of repeated fast scans with a typical measuring time of about 0.1 s per step. This is why monitoring of the long-term decrease of the SR intensity owing to the decay of the ring current is not necessary. First multiple-beam diffraction experiments at the ESRF have shown that beam stability is not a serious problem with this source and this should be the case for all the storage rings of the third generation.

5.1.3. *The Ψ-circle diffractometer.* Measurement of interference profiles does not only make high demand on the X-ray sources but also on the diffractometer. High precision of the angular resolution and of the Ψ-scan accuracy is required. This means that the scattering vector of the basic reflection must not perform any irregular motion during the Ψ scan, *i.e.* it has to be aligned very accurately with the Ψ axis so that it always lies exactly on the Ewald sphere.

In our experimental experience, exact Ψ scans are difficult with a conventional four-circle diffractometer (see also Mo, Hauback & Thorkildsen, 1988). Therefore, a special Ψ-circle diffractometer has been constructed (Fig. 32). This instrument contains two circles θ, ν for the detector with axes perpendicular to each other and four circles for the crystal motion. The first crystal axis ω is parallel to the first detector axis ($\omega - 2\theta$ relation).

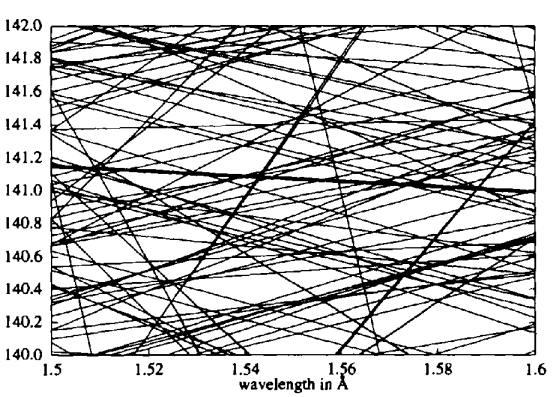

Fig. 30. Three-beam position dependence on Ψ and λ for tetragonal lysozyme with $V_c = 238\,000$ Å^3. Only three-beam cases with $q > 0.25$ (see text) for the primary reflection 470 are shown. The thick line shows the position of the three-beam case $470/251/22\bar{1}$.

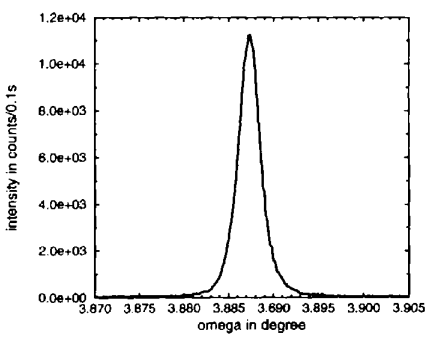

Fig. 31. ω scan of the $\bar{7}40$ reflection of a tetragonal lysozyme crystal at $\lambda = 1.33$ Å; experimental conditions: ESRF, Si 111 monochromator, π polarization.

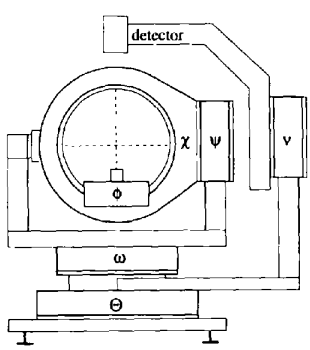

Fig. 32. Ψ-circle diffractometer.

Perpendicular to the ω axis, a second axis for the Ψ rotation is installed. This Ψ axis bears an Eulerian cradle with motions χ and ϕ. Thus, an arbitrary scattering vector **h** can be aligned with the Ψ axis and a Ψ scan is possible by moving only one circle. With the ν circle, the detector can be moved to any position on a half sphere above the horizontal diffraction plane of the primary reflection. In this way, the Ψ angle for the three-beam position can be controlled measuring the second Bragg reflection by means of a Ψ scan about the primary reflection.

All circles are driven by stepper motors that are computer controlled. The angular resolution of the detector axes is 0.001°, that of the crystal axes at least 0.0002°.

5.1.4. *Crystals.* The crystals usually used for experimental phase determination have dimensions in the range from 0.1 to 0.5 mm. No special preparation technique was applied. They were used as they were grown. Sometimes their habit was quite irregular. The investigated protein crystals were mounted in closed capillaries together with some mother liquor so that they did not lose their solvent.

It should be mentioned that absorption in the case of irregularly shaped crystals is not critical since the total Ψ-rotation range for each three-beam setting is about 0.1°. As already mentioned above, the perfection of the crystals should be as high as possible. However, ideal perfection is not required. Most of the investigated crystals showed some mosaicity. It can be estimated from the width of two-beam profiles measured with a highly collimated beam. As a rule of thumb, if the FWHM exceeds 0.05° using SR of typically 0.01° divergence, then it is difficult to measure any interference contrast. The influence of the crystal perfection on the interference contrast can be seen in Fig. 33. In this figure, the interference and reflection profiles of the same three-beam case of the two enantiomorphic forms of the same molecule are compared. The crystal of the (+)-

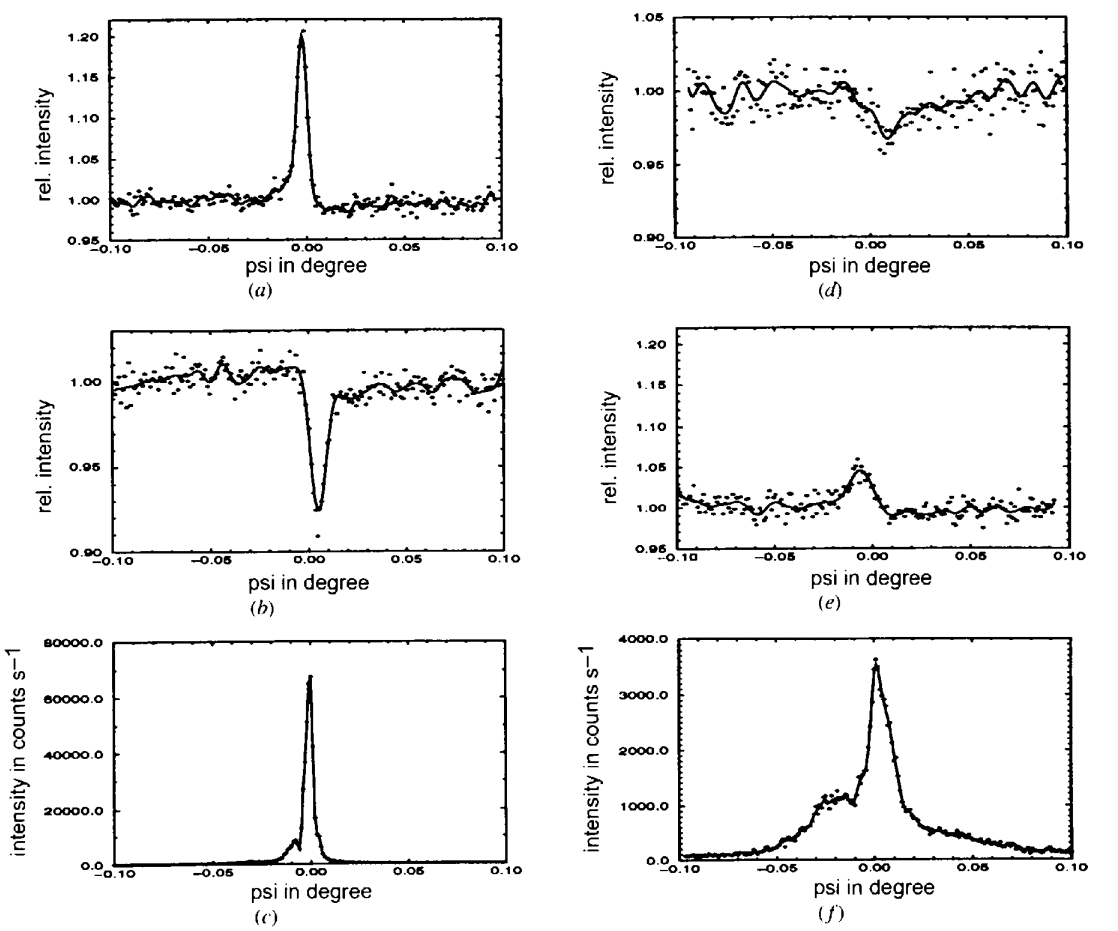

Fig. 33. Comparison of the interference profiles and the reflection profiles of the secondary reflections **g** of (+)-butafenon (left) and (−)-butafenon (right) at $\lambda = 1.8895$ Å. (+)-Butafenon: (*a*) three-beam case: $\bar{1}\,\bar{1}3/012/1\,\bar{2}1$, $\Phi_3^{calc} = -80°$; (*b*) three-beam case: $11\bar{3}/0\bar{1}\,\bar{2}/12\bar{1}$, $\Phi_3^{calc} = 80°$; (*c*) profile of the 012 reflection during Ψ scan around $\bar{1}\,\bar{1}3$. (−)-Butafenon: (*d*) three-beam case: $\bar{1}\,\bar{1}3/012/1\,\bar{2}1$, $\Phi_3^{calc} = 80°$; (*e*) three-beam case: $11\bar{3}/0\bar{1}\,\bar{2}/12\bar{1}$, $\Phi_3^{calc} = -80°$; (*f*) profile of the 012 reflection during Ψ scan around $\bar{1}\,\bar{1}3$. $|F(\bar{1}\,\bar{1}3)| = 23.4$, $|F(012)| = 44.0$, $|F(1\,\bar{2}1)| = 48.7$; experimental conditions: DORIS, Ge 111 monochromator, π polarization.

enantiomer was of good quality and shows sharp well defined interference profiles (Figs. 33*a–c*). The perfection of the (−)-enantiomer was poor (see Fig. 33*f*). Therefore, the interference effects are much weaker, wider and less defined compared with the (+) form. The aim of this investigation was the determination of the absolute structure (see §6.1). This means, however, that only the sign of the triplet phases has to be determined as the modulus is already known. It is obvious from Figs. 33(*d*), (*e*) that this can be achieved from crystals of poor quality, too.

Some crystals of macromolecules have rocking curves like that shown in Fig. 34, *i.e.* they consist of several large relatively perfect blocks whose angular distribution is very well resolved. Such crystals can still be used for phase determination because the highly collimated SR allows the excitation of only one block for three-beam diffraction, which shows the effects of a single small good-quality crystal.

5.1.5. *Measuring procedure.* In order to select suitable three-beam cases of a given crystal for the determination of the triplet phases, the following data are needed: (i) the metric parameters of the unit cell; (ii) an F_{obs} data set as complete as possible including also the low-resolution reflections in the case of protein crystals; (iii) the orientation parameters for the individual crystal.

Selected three-beam cases have to satisfy the following conditions: (i) approximately $2 < Q < 6$ [*cf.* (53)] in order to avoid *Umweganregung* and *Aufhellung* effects; (ii) search of a wavelength where the angular distance to nearest neighbours is large enough to avoid overlap of adjacent three-beam interference profiles. Given the Ψ position for a distinct wavelength of the selected three-beam case, the diffraction vector **h** of the primary reflection is first aligned accurately with the diffractometer Ψ axis by means of rotations in ϕ and χ. This procedure also finds the precise ω position. Secondly, the exact Ψ value of the three-beam position is determined experimentally by a Ψ scan about the precalculated Ψ value monitoring the secondary reflection **g**. Its maximum gives the three-beam position ($\Psi = 0$ of the diffraction patterns). Then the detector is moved back to the 2θ position of the primary reflection and the actual Ψ-scan measuring routine is started.

It should be noticed that, by using a Ψ-circle diffractometer, any error with respect to the Ψ rotation sense, *i.e.* whether it is an in–out or out–in Ψ scan (Fig. 4), is excluded because it can be read directly from the rotation sense of the Ψ axis. No further geometrical analysis is needed. All experimental profiles will be drawn with in–out rotation sense. The solid line that is plotted in addition to the measured intensities represents a smoothing spline function where statistical considerations are used to determine the amount of smoothing required (Craven & Wahba, 1979).

5.2. *Basic results*

Fig. 35 shows that the two-beam intensity of the primary reflection is modified owing to the excitation of a secondary reflection. The intensities of both reflections are measured scanning Ψ through the three-beam position and keeping the primary reflection in its diffraction position. They are plotted on the same angular scale. It can further be seen that interference only takes place within the band width accepted by the primary reflection, which is in that case the Mo $K\alpha_1$ emission line of a rotating anode.

As a result of the two-beam approximation (§3.2), it has been shown that the triplet phase that determines the three-beam Ψ-scan profiles is given by (33). In the case of negligible anomalous scattering, $-\varphi(\mathbf{h}) = \varphi(-\mathbf{h})$ and (33) can be rewritten as

$$\delta_3 = \varphi(\mathbf{g}) + \varphi(\mathbf{h} - \mathbf{g}) + \varphi(-\mathbf{h}). \qquad (54)$$

However, (54) is not valid if anomalous scattering has to be taken into account since considerable phase shifts

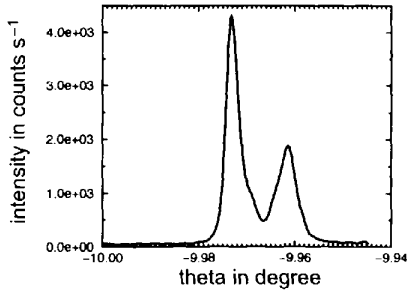

Fig. 34. ω scan of the 24,0,0 reflection of a catalase oxidoreductase crystal at $\lambda = 1.54$ Å showing clearly at least two well separated mosaic blocks. One of these blocks can be selected for a three-beam interference experiment. Experimental conditions: DORIS, Si 111 monochromator, σ polarization.

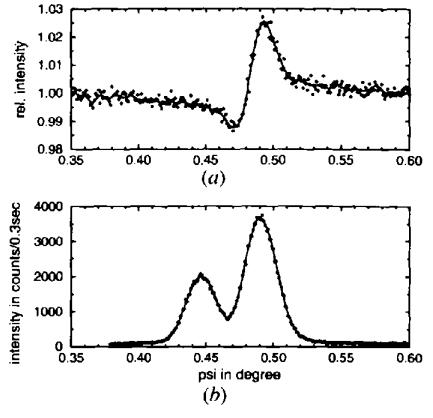

Fig. 35. (*a*) Three-beam interference profile of $\bar{2}00/\bar{1}0\bar{2}$ from L-asparagine monohydrate with Mo $K\alpha$ radiation. (*b*) Reflection profile of $\bar{1}0\bar{2}$ during the Ψ scan around $\bar{2}00$. The $K\alpha_1$ line is selected by the primary reflection and participates in the interference. Experimental conditions: 5 kW, 0.3 × 0.3 mm, effective focus rotating anode with Mo target, Zr filter, distance focus–crystal: 1 m.

may occur leading to a difference between the definitions (33) of Φ_3 and (54) of δ_3.

Fig. 36 shows that in the case of anomalous-dispersion effects only Φ_3 according to (33) is valid. In GaAs for $\lambda = 1.1236$ Å, strong anomalous phase shifts occur, in particular for the weak primary reflection $\mathbf{h} = 222$ of the three-beam case $\mathbf{h}/\mathbf{g}/(\mathbf{h}-\mathbf{g}) = 222/151/1\bar{3}1$ (Chang, 1986, 1987; Hümmer & Weckert, 1990). Accordingly, the calculated phase relationships are given by $\Phi_3 = 165.9°$ and $\delta_3 = 31.9°$ when Ga is set at at 000 and As at $\frac{1}{4}\frac{1}{4}\frac{1}{4}$. The asymmetries of Fig. 36(*a*), where, as always in this paper, an in–out scan is plotted, are only consistent with Φ_3, since for $\Psi < 0$ destructive interference is obvious. If, on the other hand, δ_3 is the involved triplet phase then the two-beam intensity would be increased for $\Psi < 0$ (*cf.* Fig. 6). The same arguments hold for Fig. 36(*b*), where $\delta_3 = -140.4°$ and $\Phi_3 = -6.4°$. The solid lines in Fig. 36 are the results of exact calculations using plane-wave dynamical theory and taking into account the divergence and energy spread of the incident beam as well as the acceptance of the crystal. The anomalous-dispersion corrections were calculated according to Cromer & Libermann (1981).

5.3. *Quantitative phase determination*

It has already been discussed in §4.4 that *Umwegan-regung* and *Aufhellung* effects may drastically influence the Ψ-scan three-beam profiles and thus the indication with respect to the triplet phase involved. Therefore, these phase-independent effects have to be subtracted from the measured profiles in order to get the pure phase-dependent interference profiles that then give an unambiguous phase indication. One possibility to evaluate these effects is to measure the two centrosymmetrically related three-beam cases $\mathbf{0}/\mathbf{h}/\mathbf{g}$ and $\mathbf{0}/-\mathbf{h}/-\mathbf{g}$, which ideally should show identical phase-independent profiles since they depend on the magnitudes of the structure factors. The triplet phases in both cases have different signs. Thus, by calculating the $\Delta I(\Psi)$ curve as defined in (52), it is possible to obtain the undisturbed interference profiles (ideal profiles). However, since in both measurements the crystal is differently oriented with respect to the incident beam and usually non-cut crystals with grown faces are used, the magnitudes of the phase-independent intensities as well as the interference contrast may be different. This considerably complicates the numerical evaluations. For the same reasons, theoretical fitting of the profiles is only possible in exceptional cases where the geometry is accurately known. Therefore, in our experience, only the centre of the phase octants of the triplet phases can be determined, *i.e.*, generally, phase determination will be restricted to the values $0 \bmod \pm 45°$. However, this accuracy will be sufficient for structure determination.

Other methods for quantitative phase determination have been proposed in several papers (*cf.* Chang & Tang, 1988; Tang & Chang, 1988, 1990; Chang, 1992). One method is the separation of the phase-independent profiles denoted by I_K by calculating a Lorentzian that depends on the diffraction geometry, the magnitudes of the involved structure factors, the diffraction peak width,

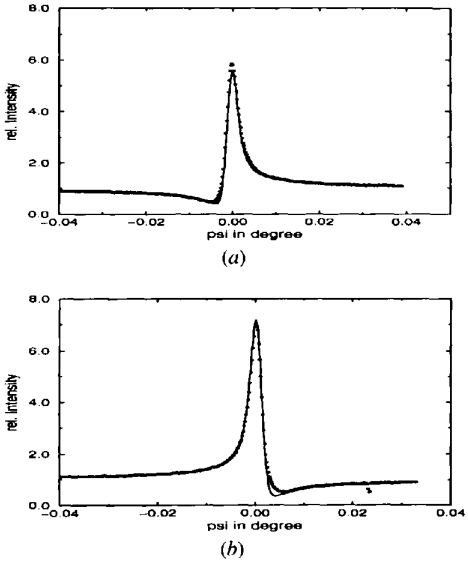

Fig. 36. (*a*) Measured (stars) and calculated (solid line) three-beam Ψ-scan profiles of GaAs. (*a*) Three-beam case: 222/151; (*b*) three-beam case: $\bar{2}\bar{2}2/\bar{1}5\bar{1}$. Diffraction geometry: Bragg–Bragg; $F(\mathbf{0}) = 238.7 + i16.05$, $|F(222)| = 11.7$, $\phi(222) = 113°$, $F(\bar{2}\bar{2}2) = F(222)$, $|F(151)| = 68.1$, $\phi(151) = 319.6°$, $|F(\bar{1}5\bar{1})| = 82.9$, $\phi(\bar{1}5\bar{1}) = 54.8°$, $|F(1\bar{3}1)| = 100.5$, $\phi(1\bar{3}1) = 319.3°$, $|F(\bar{1}3\bar{1})| = 116.3$, $\phi(\bar{1}3\bar{1}) = 51.8°$, $\lambda = 1.1236$ Å, surface normal: $\mathbf{n} = 111$; plate thickness: 0.2 mm; experimental conditions: ESRF, Si 111 monochromator, π polarization.

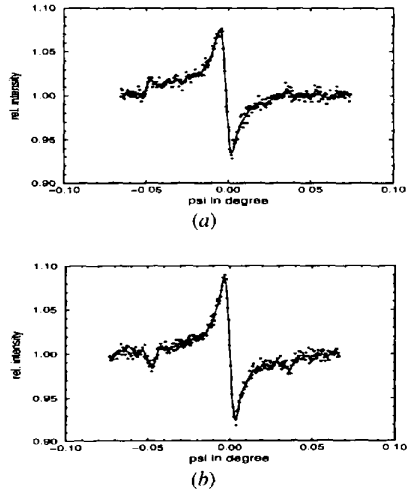

Fig. 37. Measured three-beam Ψ-scan profiles with an estimated triplet phase of 0° from tetragonal lysozyme at $\lambda = 1.367$ Å; (*a*) three-beam case: $14,7,3/\bar{2}\bar{1}0$, $\Phi_3^{\text{calc}} = 4°$ (entry 1lse of PDB); (*b*) three-beam case: $\bar{1}4,\bar{7},3/210$; $|F(14,7,3)| = 724$, $|F(\bar{2}\bar{1}0)| = 1987$, $|F(16,8,3)| = 834$; experimental conditions: ESRF, Si 111 monochromator, π polarization.

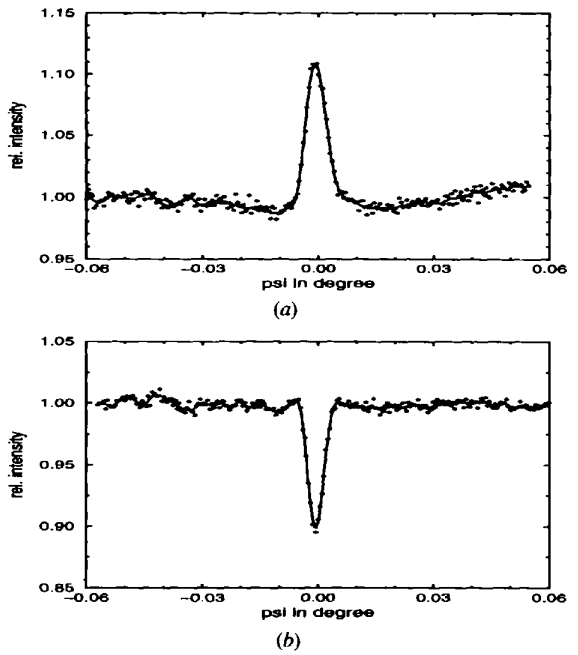

Fig. 38. Measured three-beam Ψ-scan profiles with an estimated triplet phase of $\mp 90°$ from tetragonal lysozyme at $\lambda = 1.3047$ Å; (*a*) three-beam case: $8,11,\bar{8}/14\bar{2}$, $\Phi_3^{\rm calc} = -107°$ (entry 11se of PDB); (*b*) three-beam case: $\bar{8},\bar{11},8/\bar{1}4\bar{2}$; $|F(8,11,\bar{8})| = 727$, $|F(14\bar{2})| = 1319$, $|F(77\bar{6})| = 1157$; experimental conditions: ESRF, Si 111 monochromator, π polarization.

the divergence of the incident beam and the mosaic spread of the sample. The expression of this correcting function is theoretically obtained from the first-order two-beam approximation.

Figs. 37 to 40 show typical three-beam profiles measured at the Swiss–Norwegian beamline (bending magnet) at the ESRF using an Si 111 double-crystal monochromator. We used good-quality hen egg-white lysozyme crystals as test samples. The triplet phases calculated from the atomic coordinates of the recently published structure model (Kurinov & Harrison, 1995) are inserted in each figure. The profiles of the two centrosymmetrically related three-beam cases are always plotted. Visual inspection reveals the correct phase octant (Fig. 6).

6. Applications

6.1. *Determination of the absolute structure*

For each non-centrosymmetric space group, there are two enantiomorphic forms that can be mapped onto each other by a centre of symmetry, *i.e.* the two forms differ in their handedness, which cannot be distinguished from ordinary X-ray diffraction patterns if Friedel's law is valid. This ambiguity has different meanings for different point groups (Burzlaff & Hümmer, 1988). For enantiomorphic merohedral point groups, its resolution means the determination of the absolute configuration

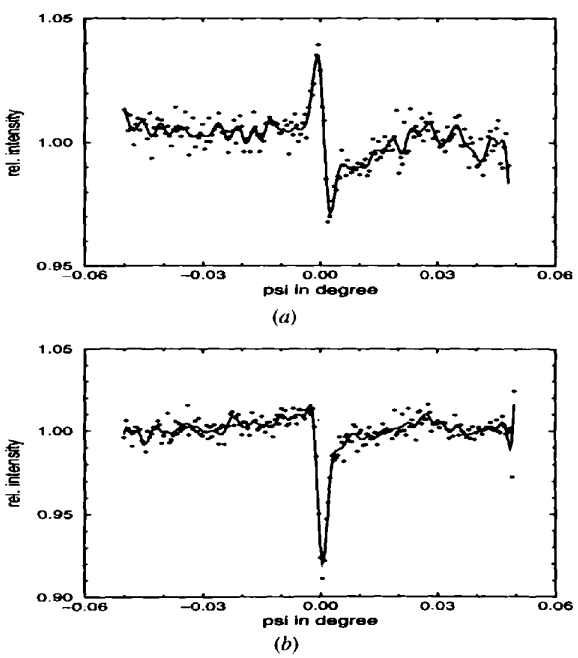

Fig. 39. Measured three-beam Ψ-scan profiles with an estimated triplet phase of $\mp 45°$ from tetragonal lysozyme with *Aufhellung* at $\lambda = 1.2669$ Å; (*a*) three-beam case: $4\bar{3}0/11\bar{1}$, $\Phi_3^{\rm calc} = -52°$ (entry 11se of PDB); (*b*) three-beam case: $\bar{4}30/\bar{1}\bar{1}1$; $|F(4\bar{3}0)| = 980$, $|F(11\bar{1})| = 4753$, $|F(3\bar{4}1)| = 1475$; experimental conditions: ESRF, Si 111 monochromator, π polarization.

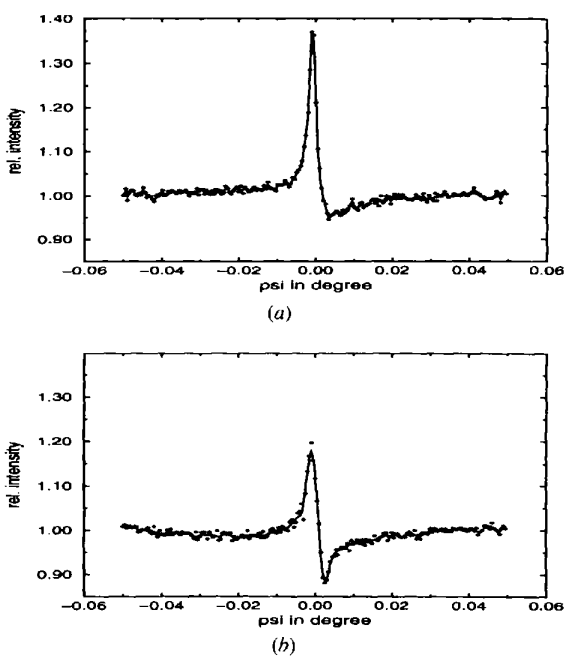

Fig. 40. Measured three-beam Ψ-scan profiles with an estimated triplet phase of $\mp 45°$ from tetragonal lysozyme with *Umwegan-regung* at $\lambda = 1.2438$ Å; (*a*) three-beam case: $4,15,\bar{4}/2\bar{1}0$, $\Phi_3^{\rm calc} = -35°$ (entry 11se of PDB); (*b*) three-beam case: $\bar{4},\bar{1}5,4/\bar{2}10$; $|F(4,15,\bar{4})| = 295$, $|F(2\bar{1}0)| = 1987$, $|F(2,16,\bar{4})| = 977$; experimental conditions: ESRF, Si 111 monochromator, π polarization.

for chiral species or the determination of the absolute conformation for achiral species. For polar point groups, it means fixing the structure with respect to the polar direction. For noncentrosymmetric roto-inversional point groups, with roto-inversions $\bar{4}$ or $\bar{6}$, it means assignment of absolute axes, for example for ZnS-type structures. Jones (1986) summarized the resolution of these ambiguities by the term determination of the absolute structure. It ultimately reduces to a determination of the signs of structure-factor phases.

One possible way for the determination of the absolute structure is to exploit the violation of Friedel's law owing to anomalous scattering comparing the intensities of suitable Bijvoet pairs (Bijvoet, Peerdeman & van Bommel, 1951). However, difficulties arise for light-atom structures. In contrast with this method, three-beam diffraction provides a means of resolving the enantiomorphism problem without the need of anomalous scattering (*cf.* Hümmer & Weckert, 1995).

Application of the operation of inversion that maps the two enantiomorphic forms, say *A* and *B*, onto each other, *i.e.* all the atomic coordinates (x_j, y_j, z_j) are changed to $(-x_j, -y_j, -z_j)$, any structure-factor phase changes its sign from $\varphi(\mathbf{h}_n)$ to $-\varphi(\mathbf{h}_n)$. If the mapping includes a shift **s** of origin, an additional phase shift by $2\pi\mathbf{h}_n \cdot \mathbf{s}$ occurs for each reflection $\mathbf{h}_n$. Since a triplet phase is structure invariant, *i.e.* independent of the choice of the origin, the phase shifts of the three reflections $\mathbf{h}, \mathbf{g}, \mathbf{h} - \mathbf{g}$ cancel and

$$\Phi_{3A} = -\Phi_{3B} \tag{55}$$

provided that the set of atomic coordinates refers to a coordinate system of the same hand. Therefore, best selectors for distinguishing *A* and *B* are triplet phases with $\Phi_3 = \pm 90°$ or close to this value (Rogers, 1980). It should be pointed out again that (55) holds without anomalous scattering effects. Therefore, if the sign of a triplet phase with $|\Phi_3| \simeq 90°$ can be determined by three-beam diffraction, the absolute structure is unambiguously fixed. This is the distinct advantage of the three-beam method over anomalous-dispersion methods in determining the absolute structure of light-atom compounds. An example where the determination of the absolute structure by means of anomalous-dispersion effects would be very difficult if not impossible is given in Fig. 41 for $C_{28}H_{20}N_2$ in space group $P2_12_12_1$.

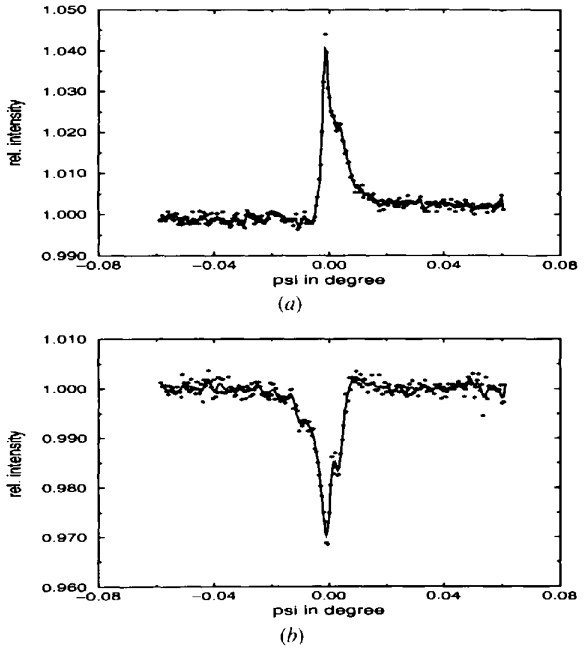

Fig. 41. Measured three-beam Ψ-scan profiles with an estimated triplet phase of $\mp 110°$ from $C_{28}H_{20}N_2$ (space group $P2_12_12_1$) at λ = 1.048 Å: (*a*) three-beam case: $032/\bar{2}2\bar{2}$, $\Phi_3^{calc} = -107.8°$; (*b*) three-beam case: $03\bar{2}/2\bar{2}2$; $|F(032)| = 36$, $|F(\bar{2}2\bar{2})| = 70$, $|F(214)| = 45$; experimental conditions: ESRF, Si 111 monochromator, π polarization; the influence of a second block can be seen in the profiles.

6.2. *Three-beam diffraction of non-periodic structures*

Up to now, it was implicitly assumed that the crystal structures under consideration are translationally periodic in three-dimensional space. Therefore, it was sufficient to use three integers to label individual lattice planes or reflections. There are, however, other classes of 'crystals', which are no longer translationally periodic in three dimensions:

(*a*) *Incommensurately modulated structures:* These structures show at least one additional incommensurate modulation of some structural details, *e.g.* atomic position or occupancy. In the case of a one-dimensional modulation all diffraction vectors, **h** can be indexed by four integers according to de Wolff, Janssen & Janner (1981)

$$\mathbf{h} = h\mathbf{a}^* + k\mathbf{b}^* + l\mathbf{c}^* + m\mathbf{q} \tag{56}$$

with h, k, l, m integers and

$$\mathbf{q} = \alpha_1\mathbf{a}^* + \alpha_2\mathbf{b}^* + \alpha_3\mathbf{c}^*, \tag{57}$$

where at least one of the coefficients α_1, α_2 and α_3 has to be irrational. In many cases, a suitable basis system $\mathbf{a}^*$, $\mathbf{b}^*$ and $\mathbf{c}^*$ can be chosen, so that all reflections with $m = 0$ are on average stronger than reflections with $m \neq 0$. Then the reciprocal lattice spanned by $\mathbf{a}^*$, $\mathbf{b}^*$ and $\mathbf{c}^*$ represents the lattice of the average or approximate structure. All reflections with $m \neq 0$ are considered to be satellite reflections that correspond to the incommensurate modulation.

(*b*) *Quasicrystals:* Since the discovery of Shechtman, Blech, Gratias & Cahn (1984), crystals are known that show no translation symmetry in at least one direction. From the large variety of quasicrystals (*cf.* Janot, 1992), two classes will be discussed briefly. (i) Decagonal quasicrystals show one translation periodic direction.

The plane perpendicular to this direction is quasicrystalline. A four-dimensional basis is needed to describe the quasicrystalline plane translationally periodic with 72° between each of these basis vectors. (ii) Icosahedral quasicrystals show no translational periodicity at all in three dimensions. They can be described periodically in six dimensions.

So far, no multibeam interference experiments have been reported on incommensurate structures and only one experiment has addressed the problem of quasicrystalline crystals (Lee, Colella & Chapman, 1993). For a three-beam case, the scattering vectors of the primary **h** and secondary **g** reflection as well as the coupling vector **h** − **g** have to form a triangle (*cf.* Fig. 3). It is possible to obtain geometrical information on the physical three-dimensional space from higher-dimensional space ($N > 3$) by a projection from the latter one into three dimensions. Therefore, any triangle in higher-dimensional space will still be an exact triangle in three dimensions if **h** and **g** are not collinear after projection. This is the necessary geometrical condition that interference between the direct and '*Umweg*' wave can take place analogous to a three-dimensional lattice. If sufficient sharp reflections exist, indicating a long enough correlation length, then interference effects are observable although the reflections are not Bragg reflections in the traditional sense.

Multiple-beam interference experiments have been carried out with incommensurately modulated calaverite ($AuTe_2$) crystals and with decagonal as well as icosahedral quasicrystals. In Figs. 42(*a*) and (*b*), examples with various orders of satellite reflections of calaverite* ($AuTe_2$) are plotted. There is a limited number of possible combinations of main structure reflections [$m = 0$ in (56)] and satellite reflections to give a three-beam case. A three-beam case with two satellite reflections of the same order m has a reciprocal-lattice vector with $m = 0$ as coupling vector. The case of two reciprocal-lattice vectors with $m = 0$ and a satellite reflection is not possible for geometrical reasons, whereas three-beam cases involving only satellite reflections are possible in any combination. Owing to the centrosymmetry of the structure [superspace group $P^{C2/m}_{\bar{1}\ s}$ (Schutte & de Boer, 1988)], only triplet phases 0 and 180° occur. In total about 25 triplet phases were determined with three-beam cases including satellite reflections up to the order $m = 3$. The experimental results from two crystals of different size and shape revealed no difference with respect to the phase information. The measured triplet phases were in agreement with the phases of the known structural model (de Boer, 1993). The mosaic spread of both crystals was about 0.01° and increased slightly during the course of the experiment. These test experiments show clearly that triplet phases that include phases of satellite reflections of incommensurate structures can be determined by three-beam interference experiments provided the crystal quality is sufficiently good.

Concerning multiple-beam diffraction of quasicrystals, two questions should be answered: (i) do interference effects actually exist?; (ii) is there evidence of lack of centrosymmetry? From normal diffraction data, icosahedral quasicrystals are found to be centrosymmetric. In a paper by Lee, Colella & Chapman (1993), however, the authors stated they had found evidence of noncentrosymmetry for an icosahedral quasicrystal of $Al_{63.7}Cu_{23.6}Fe_{12.7}$.

In Figs. 43 and 44, examples of three-beam interference profiles of the decagonal phase $Al_{70}Ni_{15}Co_{15}$ (Kek & Mayer, 1993) and of the icosahedral phase* $Al_{70}Pd_{20}Mn_{10}$ are plotted. The presence of interference effects is obvious. The profiles in Fig. 43 indicate a 0° triplet phase and *Umweganregung* effects (*cf.* §4.4). This clearly shows that it is essential to measure both centrosymmetrical related three-beam cases in order to evaluate phase-independent *Umweganregung* or *Aufhellung* effects. About 25 pairs of three-beam interference profiles were measured for the icosahedral phase. There

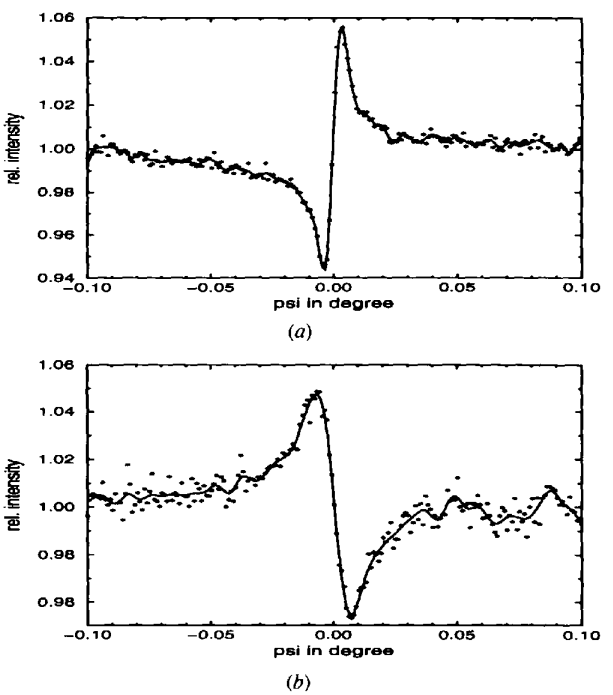

Fig. 42. Measured three-beam Ψ-scan profiles from calaverite ($AuTe_2$); (*a*) three-beam case: $2401/6220/\bar{4}2\bar{2}1$, $\Phi_3^{calc} = 180°$ (de Boer, 1993), $\lambda = 0.569$ Å, estimated triplet phase: 180°, $|F(2401)| : |F(6220)| : |F(\bar{4}2\bar{2}1)| = 1 : 1.8 : 1.47$; (*b*) three-beam case: $\bar{2}64\bar{3}/5\bar{5}1\bar{3}/3\bar{1}30$; $\lambda = 0.5631$ Å; estimated triplet phase: 0°, $|F(26\bar{4}3)| : |F(55\bar{1}3)| : |F(\bar{3}\bar{1}30)| = 1 : 0.96 : 9.5$; experimental conditions: DORIS, Si 111 monochromator, π polarization.

*Crystals and crystallographic data were kindly provided by J. de Boer, Chemische Laboratoria, Rijksuniversiteit Groningen, The Netherlands.

*Crystals of both compounds were kindly made available by S. Kek, Fachrichtung Kristallographie, Universität des Saarlandes, Germany.

is no evidence of noncentrosymmetry as all the interference profiles that could be interpreted indicate triplet phases of 0°. Unfortunately, the quality of the slightly twinned sample (FWHM of a single block was 0.015°) and the number of measured triplet phases is not sufficient to draw a final conclusion whether small deviations from centrosymmetry (point group $10/mmm$) do exist.

The reflection indices of the icosahedral crystal refer to a six-dimensional coordinate system with the axis in the directions of the fivefold axis of the icosahedron (Cahn, Shechtman & Gratias, 1986). The reflections with a 'd spacing' of 9.137 Å and a multiplicity of 12 are labelled with all the permutations of the indices ±200000. As this crystal is F-centred in six-dimensional space, only reflections with all indices even or odd were observed (Boudard *et al.*, 1992). All measured three-beam interference profiles indicate triplet phases close to 0 or 180° like in Fig. 44. This is a strong indication for centrosymmetry (point group $m\bar{3}\bar{5}$). However, for the same reasons as above, a final decision on the basis of the available data is not possible.

In comparison with the decagonal crystals, the interference contrast of this particular icosahedral crystal was two to four times stronger. This is probably due to the lower 'mosaicity' or long-range order because the FWHM of some reflections was in the range 0.008°. This is only half of the width that was measured for the decagonal sample and very close to the value for a perfect crystal under these experimental conditions.

6.3. *Direct phasing of macromolecular structures*

Experimental phase determination of protein crystals by means of three-beam diffraction reveals some specific differences compared with small-molecule structures. This concerns the weak scattering power, the very dense reciprocal lattice and therefore unavoidable overlapping of multiple-beam interference profiles and for nearly all structures radiation damage. These problems are discussed in (*a*)–(*c*) below.

(*a*) *Weak scattering power*: The moduli of structure factors for macromolecular structures even of strong reflections are small compared with the total number of electrons in the unit cell. In the case of tetragonal lysozyme, for example, the magnitude of the largest structure factor of low-resolution reflections is about 3–5% of the total scattering power of the cell. This number has to be compared with about 30 to 50% for small organic compounds and sometimes even more for inorganic compounds. The extinction length in the case of protein crystals is therefore of the order of millimetres and in this case diffraction is considered

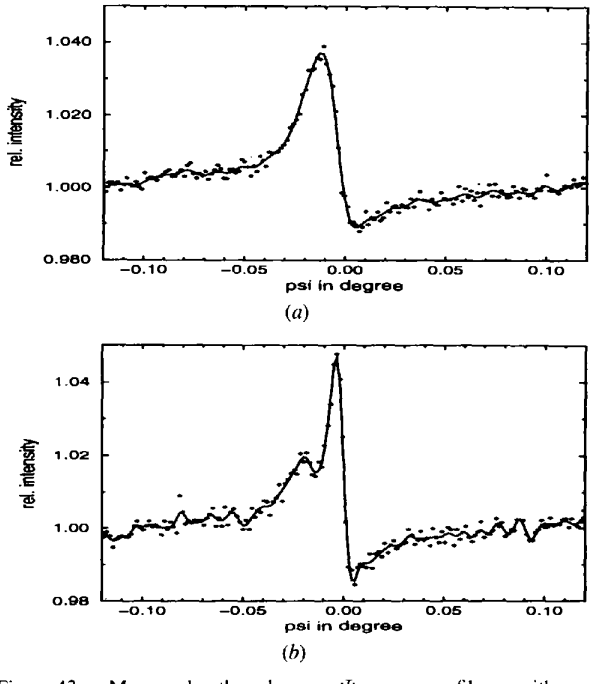

Fig. 43. Measured three-beam Ψ-scan profiles with an estimated triplet phase of 0° from a decagonal quasicrystal ($Al_{70}Ni_{15}Co_{15}$) at λ = 0.6124 Å, choice of coordinate system according to Kek & Mayer (1993); (*a*) three-beam case: $00\bar{2}\bar{1}\bar{1}/00\bar{1}\,\bar{1}3/00\bar{1}\bar{0}\bar{2}$; (*b*) three-beam case: $0021\bar{1}/0011\bar{3}/00102$; $|F(00\bar{2}\,\bar{1}\,\bar{1})| : |F(00\bar{1}\,\bar{1}3)| : |F(00\bar{1}\bar{0}\bar{2})| = 1 : 2 : 1.1$; experimental conditions: DORIS, Si 111 monochromator, π polarization.

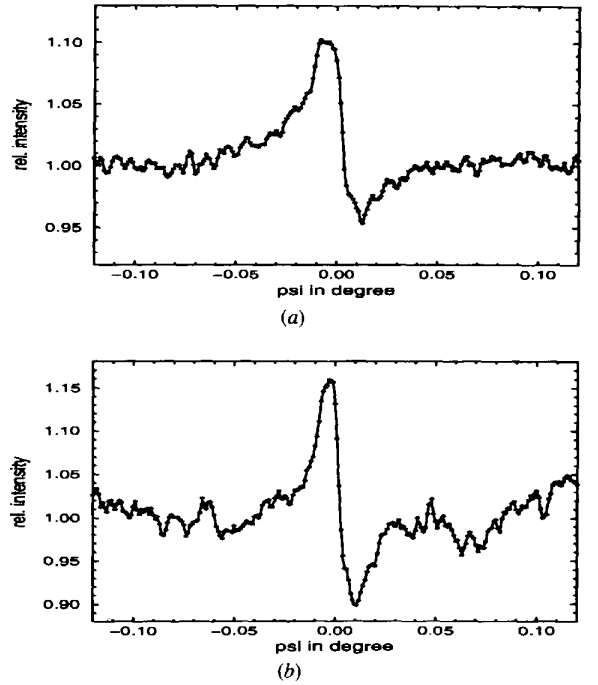

Fig. 44. Measured three-beam Ψ-scan profiles with an estimated triplet phase of 0° from an icosahedral phase ($Al_{70}Pd_{20}Mn_{10}$), λ = 0.7401 Å; (*a*) three-beam case: $\bar{1}31\bar{3}\bar{3}1/\bar{1}\,\bar{3}\,\bar{1}\,\bar{1}\bar{1}/06\bar{2}\bar{4}\bar{4}2$; (*b*) three-beam case: $1\bar{3}\,\bar{1}33\bar{1}/131\bar{1}\,\bar{1}1/06\bar{2}\bar{4}\bar{4}2$; $|F(\bar{1}31\bar{3}\bar{3}1)| : |F(\bar{1}\,\bar{3}\,\bar{1}\,\bar{1}\bar{1}\bar{1})| : |F(06\bar{2}\bar{4}\bar{4}2)| = 1 : 3.7 : 1.4$; experimental conditions: DORIS, Si 111 monochromator, π polarization.

to behave kinematically for crystal or mosaic blocks of usual sizes of the order of some tenths of a millimetre. Kinematic scattering in this context means that $I(\mathbf{h}) \propto |F(\mathbf{h})|^2$. The reflectivity or transmissivity in this range is far below the maximal possible value for a thick perfect crystal (Weckert, Schwegle & Hümmer, 1993). Nevertheless, three-beam interference effects occur as is shown theoretically in §4.3.2 and experimentally. The advantage in this regime is that the interference effects are independent of the diffraction geometry, *i.e.* independent of whether it is a primary Laue or Bragg case. Typical measured three-beam profiles for various triplet phases are shown in Figs. 37 to 40. As will be discussed below for protein crystals, only reflections with large structure factors can be used for three-beam diffraction. These are normally reflections at small scattering angles where Bragg diffraction geometry is hardly possible.

The modulation of the intensity of the primary reflection owing to three-beam interference is normally in the range of 2 to 20%. In order to obtain a reliable estimate for the triplet phase, the interference profiles have to be integrated to give adequate statistics. For the high number of phases necessary for structure determination and owing to the weak reflection intensities of protein crystals, this can only be accomplished in reasonable time by the use of high-brilliance synchrotron radiation. However, the feasibility of multibeam experiments with a laboratory source has also been reported (Huang, Wang & Chang, 1994).

(*b*) *Pseudo three-beam diffraction*: A serious problem for structures with large unit cells such as proteins is the very crowded reciprocal lattice. Therefore, with finite resolution it is not possible to excite only one single three-beam case. It has been found, however, that in spite of the high number of overlapping multibeam cases the exploitation of triplet phases is possible.

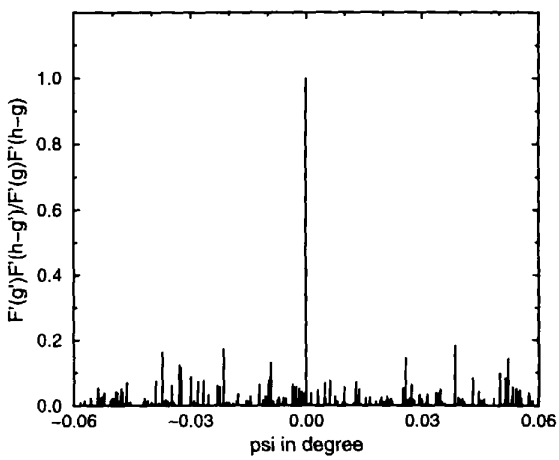

Fig. 45. Distribution of q [see (53)] of neighbours to three-beam case $\bar{7}40/\bar{5}21/22\bar{1}$ at $\lambda = 1.3302$ Å for tetragonal lysozyme. Only three-beam cases with reflections up to 2 Å resolution are drawn.

Configurations can be found at specific wavelengths for which there are only two strong reflections **h** and **g** simultaneously excited besides other weaker reflections with their reciprocal-lattice vectors $\mathbf{g}'$ inevitably at or near that diffraction position (Hümmer, Schwegle & Weckert, 1991; Weckert, Schwegle & Hümmer, 1993). The contributions of these weaker reflections to the interference profile of the 'strong' three-beam case, *i.e.* also the coupling reflection $\mathbf{h} - \mathbf{g}$ has to be comparably strong, do not disturb the estimation of the triplet phase. The weaker reflections produce a sort of noise on the recorded profile. The influence of the overlapping 'weak' three-beam cases for the same primary reflection is negligible if the amplitude of their *Umweg* wave governed approximately by $|F'(\mathbf{g}')\,F'(\mathbf{h} - \mathbf{g}')|$ is smaller than that of the strong wave. As a rule found experimentally, this is the case if

$$q = |F'(\mathbf{g}')F'(\mathbf{h} - \mathbf{g}')|/|F'(\mathbf{g})F'(\mathbf{h} - \mathbf{g})| \lesssim 0.25. \tag{58}$$

The $F'(\mathbf{h})$ are $F(\mathbf{h})$ corrected for polarization. By tuning the wavelength, one can find gaps so that the profiles of the strong three-beam cases ($q > 0.25$) do not overlap. An example for this is given in Fig. 30. The minimal necessary Ψ distance to the next strong three-beam case depends on the angular resolution of the incoming beam and on the mosaic spread of the sample. For good-quality lysozyme crystals and synchrotron radiation from an ESRF bending magnet, a distance of 0.03 to 0.04° proved to be sufficient. In Fig. 45, the q values of neighbouring three-beam cases for the 'strong' $\bar{7}40/\bar{5}21$ three-beam case of tetragonal lysozyme are shown. The corresponding experimental three-beam interference profile is shown in Fig. 46(*a*). The weak neighbouring three-beam cases do not affect the interference profile of the main one.

An advantage of the overall weak scattering power of protein crystals is that *Aufhellung* effects are weak as extinction is weak (Weckert, Schwegle & Hümmer, 1993). This fact and the observation of interference effects even in the so-called 'kinematic' range is the basis of experimental phase determination also in structures with large unit cells like proteins. The disadvantage is that in order to obey condition (58) only reflections with large structure factors are suitable for phase determination.

(*c*) *Radiation damage, use of short wavelengths*: The crystals of nearly all protein structures are damaged by X-rays. This causes the interference contrast to decrease with time. During a series of experiments, we continuously check a standard three-beam case to monitor crystal quality. The magnitude of the interference effect proved to be more sensitive to radiation damage compared with the two-beam rocking curves measured with the resolution of an Si 111 monochromator, which is not sufficient to detect small changes in crystal quality. The influence of radiation damage on the magnitude of the interference effect is illustrated in Figs. 46(*a*) and (*b*).

There is a reduction by about 50% after 36 h exposure with synchrotron radiation from a bending magnet in the wavelength range of about 1.3 to 1.45 Å.

Besides other experimental precautions like cooling, the use of shorter wavelengths below 1.0 Å may slow down crystal decay. However, with use of shorter wavelengths, the radius of the Ewald sphere is increased and, therefore, the number of overlapping three-beam cases is increased. This problem is of minor importance for proteins as strong reflections only appear up to limited resolution; this means no additional strong reflections have to be taken into account. This situation is different for small-molecule structures where high-order reflections often have significant scattering power. Although the total number of strong reflections for protein crystals remains nearly constant, the distance between strong three-beam cases with $q > 0.25$ becomes smaller for shorter wavelengths simply for geometrical reasons. This will reduce the number of measurable three-beam cases. In addition, the interference contrast decreases with shorter wavelengths as Thomson scattering gets weaker. The theoretically calculated magnitude of the interference effect of a particular three-beam case as a function of wavelength shown in Fig. 47 gives an almost linear relation. This behaviour has been proved experimentally. The disadvantage of weaker scattering, however, is in part compensated by a higher primary-beam intensity at wavelengths around 0.7 to 1.2 Å owing to the reduced absorption in the beam path. In the case of perfect crystals and strong primary reflections, short wavelengths can be advantageous owing to the longer extinction length. Therefore, additional phase shifts from *Pendellösung* effects (*cf.* §4.3.2) in Laue diffraction geometry remain small.

The existence of multibeam interference effects in macromolecular crystals was proved for the first time with myoglobin crystals (Hümmer, Schwegle & Weckert, 1991). Three-beam interference experiments with other proteins followed (Chang, King, Huang & Gao, 1991). Catalase oxidoreductase is an example with a rather large unit cell of more than 1.2×10^6 Å^3. Nevertheless, evidence for multibeam interactions for strong low-resolution reflections could be found (Weckert, Schwegle & Hümmer, 1993). For further systematic investigations, lysozyme was chosen. The triclinic form was used to find the resolution limit up to which interference effects can be observed for molecules of this size. It was possible to measure three-beam cases where reflections up to 2.0 Å resolution were involved (*cf.* Fig. 48). In total, about 50 triplet phases of triclinic lysozyme were determined with a mean phase error compared with the known structural model (entry 1lzt of PDB) of less than 20°. The resolution of the reflections involved in measured three-beam cases ranges from 30 to 2 Å with a maximum at about 4 Å.

In order to obtain a starting set of measured triplet phases for structure determination in conjunction with statistical methods or other phase extension methods, up to now about 600 triplet phases were determined from tetragonal lysozyme. The mean phase error compared with the known structure is about 20° [entry 1lse of PDB (Kurinov & Harrison, 1995)]. In this, 600 triplets and about 550 different single reflections are involved. The distribution of the resolution of these reflections is

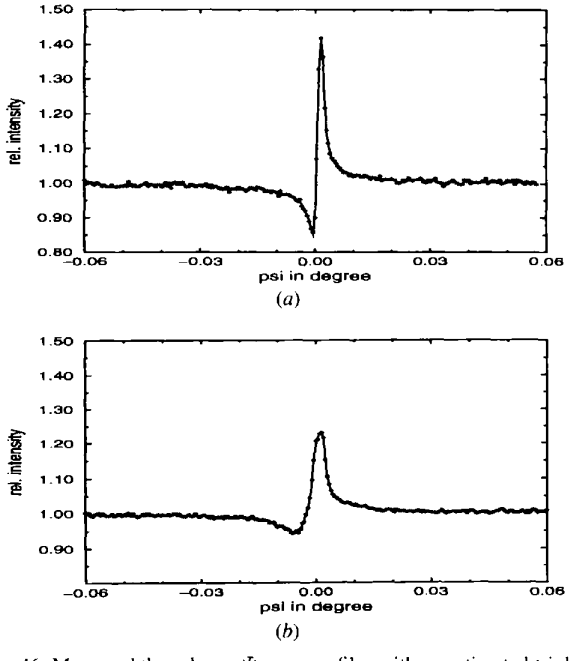

Fig. 46. Measured three-beam Ψ-scan profiles with an estimated triplet phase of 180° and *Umweganregung* from tetragonal lysozyme at $\lambda = 1.3302$ Å corresponding to Fig. 45; (*a*) three-beam case: $\bar{7}40/\bar{5}21/\bar{2}2\bar{1}$, $\Phi_3^{\rm calc} = 173.3°$ (entry 1lse of PDB); (*b*) same three-beam case as in (*a*) after 36 h exposure to X-rays; $|F(\bar{7}40)| = 1065$, $|F(\bar{5}21)| = 2027$, $|F(\bar{2}2\bar{1})| = 2902$; experimental conditions: ESRF, Si 111 monochromator, π polarization.

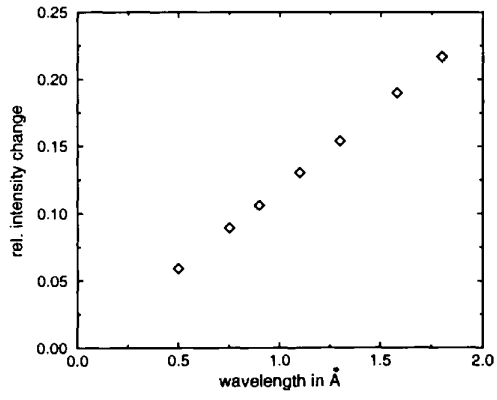

Fig. 47. Calculated magnitude of the interference effect of the three-beam case $\bar{4}\bar{3}2/\bar{2}\bar{1}0/\bar{2}\bar{2}2$, $\Phi_3^{\rm calc} = -58°$ (entry 1lse of PDB) of tetragonal lysozyme as a function of wavelength; $|F(\bar{4}\bar{3}2)| = 822$, $|F(\bar{2}\bar{1}0)| = 1987$, $|F(\bar{2}\bar{2}2)| = 2181$; diffraction geometry: Laue–Laue; plate thickness: 0.01mm.

shown in Fig. 49. The highest achievable resolution at an ESRF bending-magnet beamline was 2.5 Å. This is considerably less than that for the triclinic form. The resolution was not limited by (58) but by the intensity of the high-resolution reflections as integration time grew unacceptably. The minimum of $|F(\mathbf{h})|$ for primary reflections in measurable three-beam cases was about 250. Then at least one of $|F(\mathbf{g})|$ or $|F(\mathbf{h}-\mathbf{g})|$ has to be large (see §4.4). This will be the case for low-resolution reflections. This is the main reason for the low-resolution 'tail' of the distribution. The completeness of the reflections phased by triplets is shown in Fig. 50 with respect to two sets of reflections. One corresponds to all reflections with significant intensity and the other to reflections with $|F(\mathbf{h})| > 250$, which is the smallest structure-factor magnitude accessible experimentally at the moment. It is interesting to note that at low resolution nearly all possible phases are measured whereas the completeness decreases fast towards higher resolution.

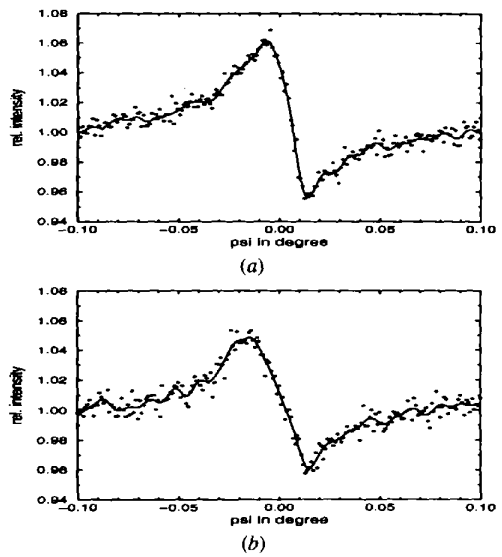

Fig. 48. Measured three-beam Ψ-scan profiles with an estimated triplet phase of 0° from triclinic lysozyme at $\lambda = 1.3583$ Å; (*a*) three-beam case: $\overline{10},8,13/\overline{5}35/\overline{5}58$, $\Phi_3^{\rm calc} = 6°$; (entry 1lzt of PDB); (*b*) three-beam case: $10,\overline{8},\overline{13}/\overline{5}3\overline{5}/5\overline{5}\overline{8}$; $|F(\overline{10},8,13)| = 822$, $|F(\overline{5}35)| = 1987$, $|F(\overline{5}58)| = 2181$; experimental conditions: ESRF, Si 111 monochromator, π polarization.

6.4. *Structure determination with measured triplet phases*

Any structure-determination procedure that should incorporate experimentally determined triplet phases has to take into account the specific kind of information that can be exploited. For example, in the case of macromolecular structures, the phases neither of weak reflections nor of high-resolution reflections are available as is worked out in the last section. The fact that the three-beam diffraction gives generally only triplet phases and not single phases has also to be regarded. A straightforward approach would be to introduce measured triplet phases into direct methods since these are based on the estimation of such three-phase invariants. Measured triplets could be used as a starting set. The problem is, however, that reflections with large $|F(\mathbf{h})|$ which are relevant for the experiment do not generally have large normalized structure factors $|E(\mathbf{h})|$, which are essential for direct methods. Investigations to make use of measured triplet phases in conjunction with direct methods are in progress.

First steps of an alternative method should be briefly discussed here. Details of this approach will be published elsewhere (Weckert, 1997). By combination of measured triplet phase relationships, it is not possible to assign single phases to all the reflections involved since certain criteria have to be obeyed to keep phase-error propagation small because only the phase octant of the triplets are determined. Even if the phases of all the

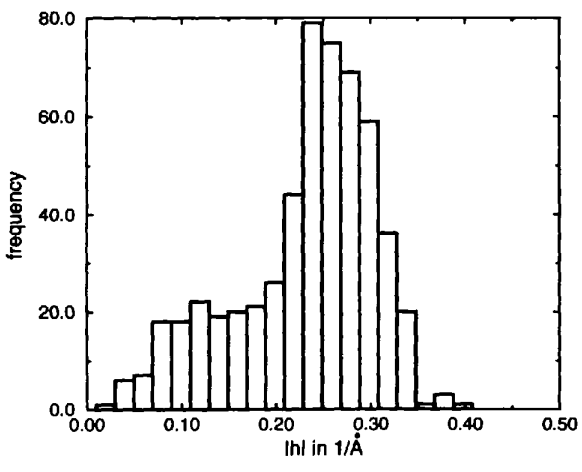

Fig. 49. Distribution of the resolution of triplet reflection measured from tetragonal lysozyme.

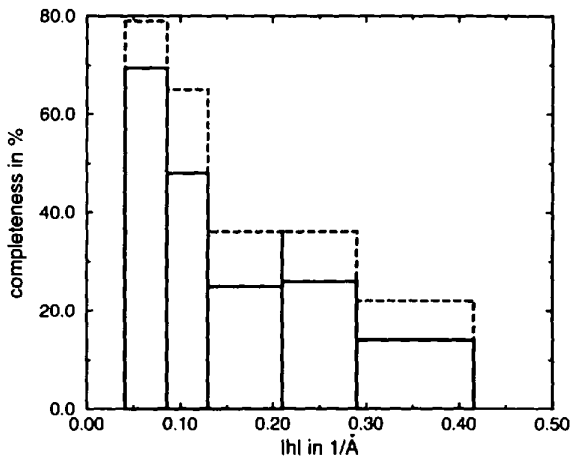

Fig. 50. Completeness of phased reflections as a function of resolution; solid: relative to reflections with $I(\mathbf{h}) > 3\sigma[I(\mathbf{h})]$; dashed: relative to reflections with $|F(\mathbf{h})| > 250$.

single reflections involved are available, a simple Fourier map calculated from say 600 strong reflections will show artifacts like negative densities from series-truncation effects. The application of the maximum-entropy method (MEM) should improve this procedure in two aspects. Firstly, by permutation of unknown phases and using likelihood criteria (Bricogne & Gilmore, 1990), good estimates for permutations with small mean phase error can be obtained. Secondly, as in the MEM an exponential model for the electron density is used, it will show no negative values and series-truncation errors are minimized. As a maximum-entropy density map also contains information on the phases of reflections that are not used in the basis set, to a certain degree, phase extension is possible. A map calculated by this method shows essential features of the molecule. However, so-called chain breaks occur. Whether it is possible to improve this map by standard methods like density modification *etc.* is under investigation. In Fig. 51, part of a maximum-entropy density map is shown, which is derived from 630 measured triplet phases where two reflections had to be permuted.

7. Discussion

It has been shown that three-beam diffraction is a powerful physical method for the determination of three-phase invariants. This information can be used to resolve the enantiomorphous ambiguity of non-centrosymmetric structures, in particular to resolve the absolute structure of light-atom compounds where anomalous-dispersion effects are small. Another application, the power of which has still to be proved in future and which is still under discussion, could be crystal structure analysis of macromolecular structures in conjunction with statistical methods, particularly if no heavy-atom derivatives with good isomorphism are available. The theoretical background and the experimental verification have been worked out in this paper. Finally, some further aspects with respect to the application of this method are discussed.

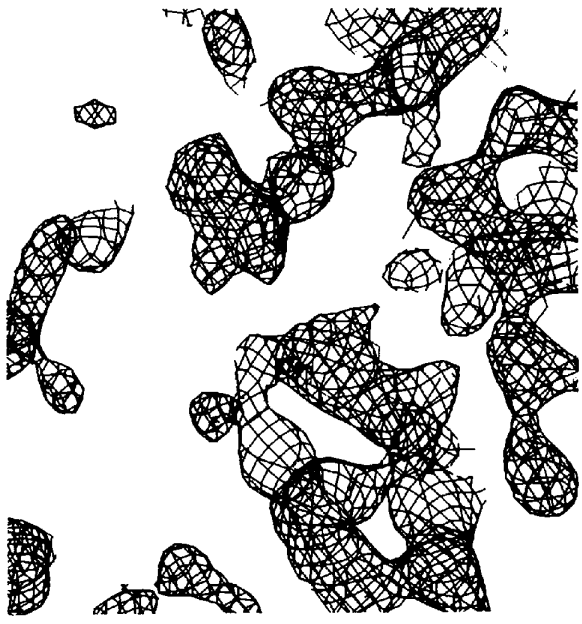

Fig. 51. Part of a maximum-entropy electron-density map calculated only with phases deduced from measured triplet phases. For this map, a low-resolution cut-off of 12 Å was used.

In §3, it was shown that multibeam interference effects take place even in the range where scattering is in general believed to be 'kinematic' if crystal thickness is small compared with extinction length and the relation $I(\mathbf{h}) \propto |F(\mathbf{h})|^2$ holds. This is exactly that range where additional phase shifts owing to *Pendellösung* oscillations in Laue diffraction geometry can be neglected. Then the interference profiles do not depend on whether the primary reflection is in Bragg reflection or Laue transmission geometry. Fortunately, this is the situation for the phase measurement of protein crystals. It leads to an unambiguous assignment of the phase octant of the three-phase invariant also for arbitrarily shaped crystals. Phase-independent *Umweganregung* or *Aufhellung* effects have to be eliminated by measurement of the profiles of the two centrosymmetrical related three-beam cases $\mathbf{h}/\mathbf{g}/\mathbf{h}-\mathbf{g}$ and $-\mathbf{h}/-\mathbf{g}/\mathbf{g}-\mathbf{h}$.

All the theoretical calculations in this paper were carried out using plane-wave dynamical theory with boundary conditions valid for a plane perfect-crystal plate. This is only an approximation with respect to the actual experimental situation. Approximately, the final divergence and wavelength band width can be taken into account by convolution with a suitable Gaussian. However, the crystals usually used are arbitrarily shaped. Nevertheless, the theoretical results reveal the basic features of three-beam diffraction that have to be known for phase determination. It would be desirable to have a more accurate theory taking into account exact shape, mosaic spread and defects.

The application of three-beam interference to small-molecule structures, for example to determine the absolute structure, can be carried out with limited effort using a rotating anode and a suitable diffractometer. However, the problem of overlapping three-beam interference profiles gets worse with larger unit cells. Three-beam interference experiments benefit from high-brilliance synchrotron-radiation sources. The overlap of interference profiles can be minimized by taking advantage of the tunability of the wavelength. The high collimation leads to narrower profiles and higher interference contrast. The higher intensity will reduce the measurement time by some orders of magnitude. However, to take full advantage of the unique properties of synchrotron radiation, the stability of the source as well as that of the diffractometer must match the experimental resolution. The number of triplets measured from

lysozyme reported in this paper could never be measured with a conventional source. The rule that, for larger unit cells and therefore in general smaller scattering power of individual reflections, a more intense source has to be used is also true for multibeam interference effects.

The most critical factor for this kind of experiment is crystal quality. Although multibeam interference effects can only be understood in the framework of dynamical theory, nearly all interference profiles presented in this paper were measured using crystals that show some mosaicity. In general, however, the magnitude of interference effects decreases with increasing mosaic spread. Therefore, a mosaic spread as small as possible is desirable. A crystal that shows a distribution of well separated nearly perfect mosaic blocks can normally still be used for interference experiments if the divergence of the incident beam is small enough to select one single mosaic block (*e.g.* Fig. 34). Up to now, we have been able to measure triplet phases from six different proteins. About every third protein crystal investigated was suitable for multibeam interference experiments. Many protein crystals showed a rather small mosaic spread of the order of 0.01° and often at the limit of the available resolution of about 0.003°. One of the main problems with these crystals is their radiation damage. To give an example, crystals of tetragonal lysozyme can stand an unfocused beam from an ESRF bending magnet for about 24 h (Fig. 46). During that time, the interference contrast reduces to 50%. The maximum number of triplet phases that we could measure from one particular crystal in the case of tetragonal lysozyme was about 150. To reduce radiation damage, the applications of cryotechniques is envisaged, which is routine for intensity data collections. However, in nearly all cases an increase of the mosaic spread is reported. This will probably cause problems for multibeam experiments.

Successful solution of a crystal structure depends on the number and the accuracy of the available phases in a resolution range where major structural details can be resolved. Whereas the accuracy that has been achieved so far by three-beam diffraction with a mean phase error of about 20° seems to be good enough, the number of phases that can be measured is still small compared with other phasing methods. The number of measured triplet phases per time depends on various factors. In the case of small-molecule structures and crystals of good quality, it is mainly limited by the driving speed of the diffractometer to adjust different three-beam positions and by the speed of the monochromator since, generally, each three-beam case is measured at a new wavelength. With synchrotron radiation, the three-beam diffraction profile can be measured with good counting statistics in the order of minutes.

In the case of macromolecular structures, the time required for one triplet phase mainly depends on the primary-beam intensity, crystal quality, size and $|F(\mathbf{h})/F(\mathbf{0})|$ of the reflections involved. With our present set-up at a bending magnet beamline at the ESRF (Swiss–Norwegian CRG beamline) and good-quality lysozyme crystals of 0.4 to 0.6 mm about four to five triplet phases in the 3 to 6 Å resolution range can be measured within 1 h. Typically, each three-beam profile contains 300 single steps (step width $\sim 4 \times 10^{-4\circ}$) each with 1 s integration time. For crystals of worse quality and thus smaller interference effects, a longer integration time is needed. The same is true for larger protein structures. In that case, the integration time and thus the intensity of the primary beam is the limiting factor.

In conclusion, if there are problems in solving structures of small and medium-size proteins by standard methods like MIR, MAD, molecular replacement *etc.*, then it is likely that three-beam diffraction in conjunction with statistically based methods might be an alternative choice.

This work has been funded by the German Federal Minister of Education, Science, Research and Technology under contract nos. 331-4005-05 647VKA and 331-4005-05 641VKA. We thank all members of our group, in particular K. Hölzer, K. Schroer and Dr W. Schwegle. We gratefully acknowledge the support at HASYLAB, DESY and at the ESRF. We particularly appreciate the hospitality at the Swiss–Norwegian CRG-Beamline (ESRF) and the support by Professor H. P. Weber, Dr P. Pattison and the beamline team. We are also grateful to Professor J. de Boer, Rijksuniversiteit Groningen, The Netherlands, for initiating the experiments with incommensurate structures.

References

Authier, A. (1993). *International Tables for Crystallography*, Vol. B, *Reciprocal Space*, edited by U. Shmueli, pp. 464–480. Dordrecht/Boston/London: Kluwer Academic Publishers.

Bethe, H. A. (1928). *Ann. Phys. (Leipzig)*, **87**, 55–129.

Bijvoet, J. M. & MacGillavry, C. H. (1939). *Chem. Weekbl.* **36**, 330–331.

Bijvoet, J. M., Peerdeman, A. F. & van Bommel, A. F. (1951). *Nature (London)*, **168**, 271.

Boer, J. L. de (1993). Personal communication.

Boudard, M., de Boissieu, M., Janot, C., Heger, G., Beeli, C., Nissen, H.-U., Vincent, H. & Ibberson, R. (1992). *Condens. Matter*, **4**, 10149–10168.

Bricogne, G. & Gilmore, C. J. (1990). *Acta Cryst.* A**46**, 284–297.

Burzlaff, H. & Hümmer, K. (1988). *Acta Cryst.* A**44**, 506–508.

Cahn, J. W., Shechtman, D. & Gratias, D. (1986). *J. Mater. Res.* **1**, 13–27.

Chang, S. L. (1982). *Phys. Rev. Lett.* **48**, 163–166.

Chang, S. L. (1984). *Multiple Diffraction of X-rays in Crystals*. Berlin/Heidelberg/New York: Springer Verlag.

Chang, S. L. (1986). *Phys. Rev. B*, **33**, 5848–5850.

Chang, S. L. (1987). *Crystallogr. Rev.* **1**, 87–189.
Chang, S. L. (1992). *Int. J. Mod. Phys.* B**6**, 2987–3020.
Chang, S. L., Hong, S. W., Luh, S. W., Pan, H. H., Tang, M. C. & Sasaki, J. M. (1988). *Acta Cryst.* A**44**, 63–70.
Chang, S. L., King, H. E., Huang, M. T. & Gao, Y. (1991). *Phys. Rev. Lett.* **67**, 3113–3116.
Chang, S. L. & Tang, H. T. (1988). *Acta Cryst.* A**44**, 1065–1072.
Colella, R. (1974). *Acta Cryst.* A**30**, 413–423.
Colella, R. (1995). *Comments Condens. Matter Phys.* **17**, 175–198, 199–215.
Craven, P. & Wahba, G. (1979). *Numer. Math.* **31**, 377–403.
Cromer, D. T. & Liberman, A. A. (1981). *Acta Cryst.* A**37**, 267–268.
Ewald, P. (1917). *Ann. Phys. (Leipzig)*, **54**, 519–597.
Ewald, P. P. (1958). *Acta Cryst.* **11**, 888–891.
Ewald, P. P. (1965). *Rev. Mod. Phys.* **37**, 46–56.
Ewald, P. P. & Heno, Y. (1968). *Acta Cryst.* A**24**, 5–15.
Høier, R. & Marthinsen, K. (1983). *Acta Cryst.* A**39**, 854–860.
Huang, M. T., Wang, C. M. & Chang, S. L. (1994). *Acta Cryst.* A**50**, 342–344.
Hümmer, K. & Billy, H. (1982). *Acta Cryst.* A**38**, 841–848.
Hümmer, K. & Billy, H. (1986). *Acta Cryst.* A**42**, 127–133.
Hümmer, K., Bondza, H. & Weckert, E. (1991). *Z. Kristallogr.* **195**, 169–188.
Hümmer, K., Schwegle, W. & Weckert, E. (1991). *Acta Cryst.* A**47**, 60–62.
Hümmer, K. & Weckert, E. (1990). *Acta Cryst.* A**46**, 534–536.
Hümmer, K. & Weckert, E. (1995). *Acta Cryst.* A**51**, 431–438.
Janot, C. (1992). *Quasicrystals, a Primer*. Oxford: Clarendon Press.
Jones, P. G. (1986). *Acta Cryst.* A**42**, 57.
Juretschke, H. J. (1982*a*). *Phys. Rev. Lett.* **48**, 1487–1489.
Juretschke, H. J. (1982*b*). *Phys. Lett.* A**92**, 183–185.
Juretschke, H. J. (1984). *Acta Cryst.*, A**40**, 379–389.
Juretschke, H. J. (1986). *Phys. Status Solidi B*, **135**, 455–466.
Kato, N. (1958). *Acta Cryst.* **11**, 885–887.
Kato, N. (1992). *P. P. Ewald and his Dynamical Theory of X-ray Diffraction*, edited by D. W. J. Cruickshank, H. J. Juretschke & N. Kato, pp. 3–23. Oxford University Press.
Kek, S. & Mayer, J. (1993). *Z. Kristallogr.* **205**, 235–253.
Kurinov, I. V. & Harrison, R. W. (1995). *Acta Cryst.* D**51**, 98–109.
Laue, M. von (1960). *Röntgenstrahl-Interferenzen*. Frankfurt am Main: Akademische Verlagsgesellschaft.
Lee, H., Colella, R. & Chapman, L. D. (1993). *Acta Cryst.* A**49**, 600–605.
Lipscomb, W. N. (1949). *Acta Cryst.* **2**, 193–194.
Mo, F., Hauback, B. C. & Thorkildsen, G. (1988). *Acta Chem. Scand.* A**42**, 130–138.
Moon, R. M. & Shull, C. G. (1964). *Acta Cryst.* **17**, 805–812.
Ott, H. (1938). *Ann. Phys. (Leipzig)*, **31**, 264–288.
Pinsker, Z. G. (1978). *Dynamical Scattering of X-rays in Crystals*. Berlin: Springer Verlag.
Post, B. (1975). *Acta Cryst.* A**31**, 153–155.
Post, B. (1977). *Phys. Rev. Lett.* **39**, 760–763.
Post, B. (1979). *Acta Cryst.* A**35**, 17–21.
Post, B., Gong, P. P., Kern, L. & Ladell, J. (1986). *Acta Cryst.* A**42**, 178–184.
Renninger, M. (1937). *Z. Kristallogr.* **97**, 107–121.
Rogers, D. (1980). *Theory and Practice of Direct Methods in Crystallography*, edited by M. F. C. Ladd & R. A. Palmer, pp. 23–91. New York: Plenum Press.
Schutte, W. J. & de Boer, J. L. (1988). *Acta Cryst.* B**44**, 486–494.
Schwegle, W. F. (1989). Diploma thesis, Universität Erlangen, Germany.
Schwegle, W. F. (1993). PhD thesis, Universität Karlsruhe (TH), Germany.
Shechtman, D., Blech, I., Gratias, D. & Cahn, J. W. (1984). *Phys. Rev. Lett.* **53**, 1951–1953.
Shen, Q. & Colella, R. (1988). *Acta Cryst.* A**44**, 17–21.
Shen, Q. & Finkelstein, K. D. (1990). *Phys. Rev. Lett.* **65**, 3337–3340.
Shen, Q. & Finkelstein, K. D. (1992). *Phys. Rev.* B**45**, 5075–5078.
Tang, M. T. & Chang, S. L. (1988). *Acta Cryst.* A**44**, 1073–1078.
Tang, M. T. & Chang, S. L. (1990). *Phys. Lett.* A**143**, 405–408.
Thorkildsen, G. (1987). *Acta Cryst.* A**43**, 361–369.
Weckert, E. (1997). *Acta Cryst.* Submitted.
Weckert, E. & Hümmer, K. (1990). *Acta Cryst.* A**46**, 387–393.
Weckert, E., Schwegle, W. & Hümmer, K. (1993). *Proc. R. Soc. London Ser. A*, **442**, 33–46.
Wolff, P. M. de, Janssen, T. & Janner, A. (1981). *Acta Cryst.* A**37**, 625–636.
Woolfson, M. M. & Fan, H.-F. (1995). *Physical and Non-Physical Methods of Solving Crystal Structures*. Cambridge University Press.
Zachariasen, W. H. (1967). *Acta Cryst.* **23**, 558–564.